

DOCTORAL THESIS

Fire Resistance Design Model for Walls and Floors with Wooden I-joists

Katrin Nele Mäger

TALLINN UNIVERSITY OF TECHNOLOGY
DOCTORAL THESIS
84/2025

Fire Resistance Design Model for Walls and Floors with Wooden I-joists

KATRIN NELE MÄGER



TALLINN UNIVERSITY OF TECHNOLOGY

School of Engineering

Department of Civil Engineering and Architecture

This dissertation was accepted for the defence of the degree 21/10/2025

Supervisor: Professor Alar Just
School of Engineering
Tallinn University of Technology
Tallinn, Estonia

Co-supervisor: Dr. Magdalena Sterley
Sollentuna, Sweden

Opponents: Dr. Pedro Palma
EMPA
Swiss Federal Laboratories for Materials Science and Technology
Zürich, Switzerland

Dr. Christian Dagenais
FPInnovations
Quebec, Canada

Defence of the thesis: 02/12/2025, Tallinn

Declaration:

Hereby I declare that this doctoral thesis, my original investigation and achievement, submitted for the doctoral degree at Tallinn University of Technology has not been submitted for doctoral or equivalent academic degree.

Katrin Nele Mäger

signature



European Union
European Regional
Development Fund



Investing
in your future

Copyright: Katrin Nele Mäger, 2025

ISSN 2585-6898 (publication)

ISBN 978-9916-80-403-2 (publication)

ISSN 2585-6901 (PDF)

ISBN 978-9916-80-404-9 (PDF)

DOI <https://doi.org/10.23658/taltech.84/2025>

Printed by Koopia Niini & Rauam

Mäger, K. N. (2025). *Fire Resistance Design Model for Walls and Floors with Wooden I-joists* [TalTech Press]. <https://doi.org/10.23658/taltech.84/2025>

TALLINNA TEHNIKAÜLIKOOL
DOKTORITÖÖ
84/2025

Puidust I-taladega karkass-seinte ja vahelagede tulepüsivuse arvutusmudel

KATRIN NELE MÄGER



Contents

Contents.....	5
List of publications	7
Author’s contribution to the publications	8
Introduction	9
Abbreviations	10
Symbols	11
Greek letters	13
1 Background	14
1.1 Timber frame assemblies	14
1.2 I-joists	15
1.2.1 Bending capacity of I-joists at ambient conditions	15
1.3 Buckling at ambient conditions according to FprEN 1995-1-1 Annex B	16
1.4 Fire design methods for timber frame assemblies	18
1.4.1 Charring.....	18
1.4.2 Mechanical resistance.....	21
1.4.3 Separating function method	22
1.5 Fire design of wood-based I-joists in floors	24
1.6 Fire design of wood-based I-joists in walls.....	24
1.7 Database of previous test results.....	25
1.7.1 Model-scale furnace fire tests.....	25
1.7.2 Full-scale furnace fire tests	25
1.8 Knowledge gaps	28
1.9 Objectives and scope	29
2 Methodology.....	30
3 Investigation of charring behaviour	33
3.1 Unloaded model-scale tests.....	33
3.1.1 Methodology.....	33
3.1.2 Results	35
3.2 Thermal FE simulations	37
3.2.1 Methodology.....	37
3.2.2 Results and analysis	44
3.2.3 Comparison with calculations and model-scale tests	47
3.3 Development of charring equations	55
3.3.1 Methodology (Script 3)	55
3.3.2 Results and analysis	55
4 Investigation of mechanical behaviour	60
4.1 Loaded model-scale tests.....	60
4.1.1 Methodology.....	60
4.1.2 Results and analysis	63
4.2 Mechanical FE simulations.....	64
4.2.1 Methodology.....	65
4.2.2 Results and analysis	67
4.3 Thermal FE simulations with strength reduction factors.....	71

4.3.1 Methodology.....	71
4.3.2 Results and analysis	71
4.4 Development of zero-strength layer depth expressions.....	73
4.4.1 Methodology (Script 5)	73
4.4.2 Results and analysis	74
4.5 Compression at normal temperature	84
4.5.1 Experimental investigation	84
4.5.2 Numerical investigation	88
4.5.3 Experimental results	94
4.5.4 Results of numerical investigations	99
4.5.5 Analysis of numerical and experimental results	101
5 Design of wooden I-joists in fire.....	103
5.1 Charring.....	103
5.2 Zero-strength layer	106
5.3 Buckling	107
5.4 Adhesives	108
5.5 Validation	108
5.5.1 Charring.....	108
5.5.2 Load-bearing capacity	110
6 Discussion.....	117
6.1 Finite element methods.....	117
6.2 Experimental investigations.....	119
6.3 Design model	119
6.4 Limitations and further research	122
6.5 Closing remarks.....	123
7 Summary	124
List of figures.....	126
List of tables	130
References	132
Acknowledgements.....	134
Abstract.....	135
Lühikokkuvõte.....	137
Appendix	139
Curriculum vitae.....	142
Elulookirjeldus.....	143

List of publications

The results of the doctoral thesis have been published in the following publication(s):

- I Mäger, K.N., Tiso, M., Just, A. (2020). Fire design model for timber frame assemblies with rectangular and I-shaped members. In: Makovicka Osvaldova, L., Markert, F., Zelinka, S. (eds) Wood & Fire Safety. WFS 2020. Springer, Cham. <https://doi.org/10.1007/>
- II Mäger, K. N., Just, A. (2025). Charring design model for light timber frame assemblies with load-bearing I-joists. Fire Safety Journal. <https://doi.org/10.1016/j.firesaf.2025.104369>
- III Mäger K.N., Just, A., Sterley, M, Olofsson, R. (2021). Influence of adhesives on fire resistance of wooden I-joists. World Conference on Timber Engineering (WCTE), 2021. p. 1172–1179.

Other published works:

- IV Mäger K.N., Just, A. (2019) Design methods for wood-based I-joists exposed to fire – State-of-the-art and improvements. In: Proceedings of the 15th International Interflam Conference. (1343–1354). Interflam 2019, Royal Holloway College, UK, 1-3 July 2019.
- V Mäger, K. N.; Just, A. (2019). Preliminary design model for wooden I-joists in fire. In: Proceedings of the International Network on Timber Engineering Research (INTER), Meeting 52, Tacoma, USA. (393–406).
- VI Mäger, K. N.; Just, A.; Persson, T.; Wikner, A. (2020). Fire Design of I-joists in Wall Assemblies. Proceedings of the International Network on Timber Engineering Research (INTER): Meeting 53, Online. Timber Scientific Publishing, 243–258.

Author's contribution to the publications

Contribution to the papers in this thesis are:

- I Fire design model for timber frame assemblies with rectangular and I-shaped members

Published in: Wood & Fire Safety. WFS 2020.

Contributor	Contribution Roles
Katrin Nele Mäger	I-joists: Conceptualization, Methodology, Software, Formal Analysis, Writing
Mattia Tiso	Rectangular members: Conceptualization, Methodology, Formal Analysis, Writing
Alar Just	Supervision, Project Administration

- II Charring design model for light timber frame assemblies with load-bearing I-joists

Published in: Fire Safety Journal, 2025

Contributor	Contribution Roles
Katrin Nele Mäger	Conceptualization, Methodology, Software, Formal Analysis, Validation, Writing
Alar Just	Supervision, Project Administration, Resources

- III Influence of adhesives on fire resistance of wooden I-joists

Published in: World Conference on Timber Engineering (WCTE) 2021

Contributor	Contribution Roles
Katrin Nele Mäger	Formal Analysis, Visualisation, Writing, Presenting
Alar Just	Conceptualisation, Project Administration
Magdalena Sterley	Conceptualisation, Methodology, Investigation
Robert Olofsson	Investigation, Data Curation

Introduction

This doctoral thesis proposes a new fire resistance calculation model for wooden I-joists in the ISO 834 standard fire situation (ISO, 1999). Currently, lightweight and more optimised structures are gaining popularity in the climate of scarcity of resources and supply chain issues. Therefore, the optimal use of timber material is important and encouraged.

I-joists are engineered wood products consisting of two flanges and a web connecting them. The flanges can be made of strength graded sawn wood, laminated veneer lumber (LVL) or, in some cases, even glue laminated timber (GLT). The web is usually made of a wood-based board such as oriented strand board (OSB), plywood, fibreboard, etc. Products outside the scope of this thesis may feature thin steel webs or truss-like wood framing between the flanges. These latter products are seldom used in typical timber frame houses and more often utilised as supports for concrete forms, for example.

This thesis aims to provide the practicing structural engineers with an easy-to-use and comprehensive design model for verifying the load-bearing capacity of I-joists exposed to the ISO 834 standard fire. Currently, some models exist which allow for the analysis of a limited number of structural assemblies. These models have not been standardised, and they are available only in handbooks and scientific reports. The content and limitations of these models will be discussed in detail. These gaps have been filled based on the work conducted during the preparation of this thesis.

The proposed design model follows the Effective Cross-Section Method principles and has been developed based on an extensive finite element thermal simulation programme and furnace fire tests. Additionally, the performance of adhesives in the finger joints of the flanges will be discussed based on loaded furnace fire tests and other tests at elevated temperatures.

In Europe, the Eurocodes are harmonised design standards which provide the engineer with widely accepted calculation models for the verification of the performance of different types of structures in various use scenarios, including in the fire situation. These standards are currently under revision. The standard for timber structures in fire, Eurocode 5 Part 1-2, does not include guidance for I-joists in fire. One of the aims of this doctoral study has been to provide a model for I-joists which could be introduced into the standard.

This thesis summarises and provides further background and explanations to the work presented in the publications listed previously. The journal papers have been peer-reviewed and conference papers were reviewed based on extended abstracts. This doctoral project has contributed to the field in broadening the scope of existing calculation models and with the extensive use of finite element modelling to investigate the charring and mechanical behaviour of wooden structures.

This thesis will first describe the state of the art of the design of I-joists both at ambient and fire conditions. The background of fire design methods in the draft version of the Eurocode 5 Part 1-2 is given. Then, the methodology used for the experimental investigations is described. This includes finite element (FE) thermal and thermo-mechanical simulations and different tests. The results of the tests and simulations are provided. Finally, the procedure used to develop the design model is described and all necessary model parameters are given. The last part of the thesis will focus on discussion of limitations and recommendations for future research.

Abbreviations

Btn	wooden battens with void cavities
CAM	Component Additive Method
CEN	European Committee for Standardisation
CF	cellulose fibre insulation
CSW	compression side warm
CP	clay plaster
ECSM	Effective Cross-Section Method
FE(M)	finite element (method)
FPM	fire protection material
FSITB	European guideline <i>Fire Safety in Timber Buildings</i>
FST	full-scale test
GF	gypsum fibreboard
GLT	glue laminated timber
GtA	gypsum plasterboard type A (or any other than type F)
GtF	gypsum plasterboard type F
GW	glass wool insulation
LVL	laminated veneer lumber
MOE	modulus of elasticity
MSE	mean square error
MST	model-scale test
MUF	melamine urea formaldehyde adhesive
N/A	not applicable, not available
OSB	oriented strand board
PB	wooden particleboard
PL	protection level
PRF	phenolic resorcinol formaldehyde adhesive
PUR	polyurethane adhesive
RPM	Reduced Properties Method
SFM	Separating Function Method
SW	stone wool insulation
TC	thermocouple
TFA	timber frame assembly
TSW	tension side warm
TTF	time to failure
WF	wood-fibre insulation
WFB	wooden fibreboard

Symbols

A_{ef}	effective area of the flange, mm ²
A_{fi}	charred area of the flange, mm ²
b_f	initial flange width, mm
$b_{f,ef}$	effective width of the unbraced flange, mm
b_{fi}	charred flange width, mm
b_w	thickness of the web, mm
$b_{w,ef}$	effective thickness of the web, mm
d_0	zero-strength layer depth, mm
$d_{char,0}$	one-dimensional charring depth, mm
$d_{char,n}$	notional charring depth
$d_{char,n,1}$	notional char depth on the fire exposed side, mm
$d_{char,n,2}$	notional char depth on the lateral side, mm
$d_{char,w}$	notional char depth of the web, mm
E_0	modulus of elasticity parallel to grain, N/mm ²
E_f	modulus of elasticity of the flange material, MPa
E_w	modulus of elasticity of the web material, MPa
$E_{w,x}I_{w,x}$	bending stiffness of the web about the x-axis, Nmm ²
F	load that causes the deformation, N
H	depth of the I-shaped member, mm
h_f	initial flange height, mm
$h_{f,ef}$	effective height of the unbraced flange, mm
h_{fi}	charred flange height, mm
h_p	thickness of the gypsum board, mm
h_w	height of the web between the flanges, mm
i	layer with a protective function, -
$I_{y/z}$	second moment of inertia about the respective axis, mm ⁴
k_2	protection factor of the fire protection system, -
$k_{3,1}$	post-protection coefficient for the exposed side, -
$k_{3,2}$	post-protection coefficient for the lateral side, -
$k_{3,w}$	post-protection factor for the web (equal to 2), -
k_4	consolidation coefficient for the lateral side, -
k	spring coefficient of the web,
k_c	factor for lateral instability, -
$k_{fb,y/z}$	factor accounting for the influence of boundary conditions, for lateral buckling about respective axis, -
$k_{j,i}$	joint coefficient of the layer i , -
$k_{j,n}$	joint coefficient of the last layer n , -
k_n	modification factor for corner rounding, -
$k_{pos,exp,i}$	position coefficient for the fire exposed side of the layer i , -

$k_{\text{pos,unexp},i}$	position coefficient for the unexposed side of the layer i , -
$k_{\text{pos,exp},n}$	position coefficient for the fire exposed side of the last layer n , -
k_r	spring stiffness of the smeared restraint, N/mm ²
K_{rel}	relative stiffness, -
$k_{s,n,1}$	combined section and conversion factor for the exposed side, -
$k_{s,n,2}$	combined section and conversion factor for the lateral side, -
k_w	stiffness of the unit length of the web,
l	length of the member, mm
$l_{c,y/z,\text{ef}}$	effective length for lateral buckling about the respective axis, mm
l_{ef}	effective length of the column, mm
$l_{z,\text{ef},m}$	effective buckling length for lateral buckling about the z-axis obtained from the FE model, mm
n	last layer of the assembly with an insulating function, -
$N_{y/z,\text{crit}}$	critical load, N
$N_{\text{crit},0}$	critical (Euler) force of the unbraced member, N
p	number of data points, -
t	time of the fire exposure, min
t_a	consolidation time, min
t_{ch}	start time of charring, min
$t_{\text{ch},2}$	start time of charring on the lateral side, min
$t_{\text{ch},w}$	start time of charring of the web, min
t_f	failure time of the fire protection system, min
t_{ins}	insulation time of the assembly, min
$t_{\text{ins},n}$	insulation time of the last layer of the assembly on the unexposed side, min
$t_{\text{ins},0,n}$	basic insulation time of the last layer n , min
$t_{\text{prot},i}$	protection time of the layer i , min
$t_{\text{prot},0,i}$	basic protection time of the layer i , min
Y_m	observed values
\widehat{Y}_m	predicted values

Greek letters

β_0	one-dimensional charring rate perpendicular to the grain, mm/min
β_n	basic design charring rate perpendicular to the grain, mm/min
$\beta_{n,w}$	notional design charring rate of the web material, mm/min
δ	deformation, mm
Δt_i	correction time of the layer i , min
Δt_n	correction time of the last layer n , min
$\lambda(\rho)$	density-dependent thermal conductivity, W/(m·K)
ρ_{20}	density at ambient temperature, kg/m ³

1 Background

This chapter will provide the context for the work of this doctoral project. First, an introduction is made to timber frame assemblies (TFA) and I-joists which may be used as the load-bearing members in TFA. Then, the calculation principles of I-joists at ambient temperatures are described based on EN 1995-1-1:2004 (CEN, 2004b) and FprEN 1995-1-1:2025 (CEN, 2025a).

Secondly, the fire design models of load-bearing timber structures and TFA are summarised. Finally, the currently available methods for calculating the load-bearing capacity in fire of walls and floors with I-joists will be described and analysed.

The focus of this chapter is on European fire design models to provide input for further improvements to these models and to ultimately develop a general model which can be used for both walls and floors when exposed to the ISO 834 standard fire (ISO, 1999). The deficiencies of the current fire design models for I-joists will be highlighted.

1.1 Timber frame assemblies

Timber frame assemblies are lightweight structural systems with straight solid wood load-bearing members. The timber members are spaced at regular intervals, typically at 400 to 600 mm. The load-bearing timber members are connected to edge members and to each other by boards or sometimes laths to form panel-like structures. TFA may be used as vertical (walls), horizontal (floors) or angled panels (roofs).

TFA often include gypsum plasterboards or wood-based boards as part of the structural assembly. The boards provide bracing and allow the timber members to be unified. The cavities which are formed between the boards and each timber member are often insulated to improve thermal and acoustic performance.

An example of a typical TFA with rectangular timber members is shown in Figure 1. Such structures are typically insulated with batt-type or blown-in loose fill thermal insulation materials.

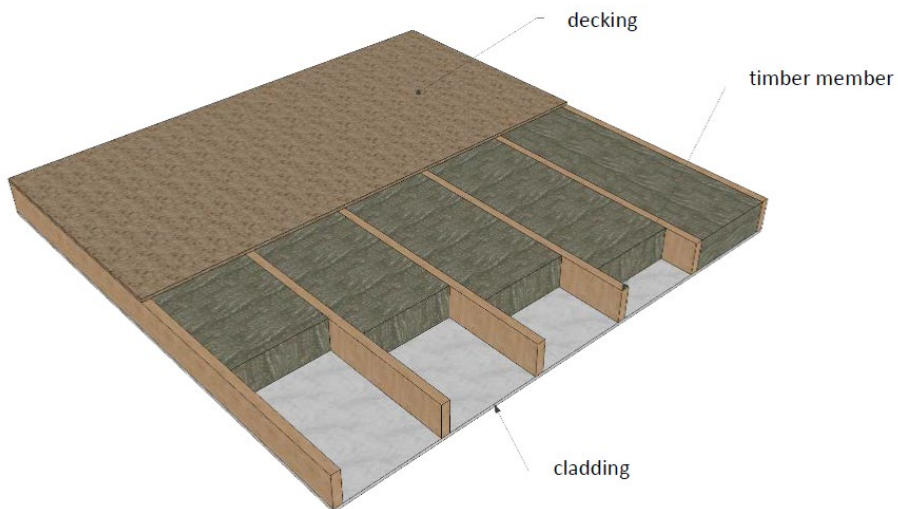


Figure 1. Timber frame assembly (Tiso, 2018).

Timber frame assemblies are material efficient and suitable for factory production or on-site construction. Relatively small timber sections can be used. TFA is popular in Nordic countries due to the possibility to prefabricate and insulate the cavities. Prefabrication reduces the need for long construction times on site and provides a higher quality of assembly.

The design possibilities of TFA are flexible with the advantage that the claddings inherently provide a smooth wall or ceiling surface. The lightweight nature of TFA reduces the need for large foundations. Many bio-based materials are often used in TFA, making it an environmentally conscious choice.

Some disadvantages of TFA are connected to its light weight and use of wood-based materials. Improper design and use may lead to moisture damage and shorter durability. Fire resistance needs specific attention. Open floor plans can be difficult to achieve with typical sawn wood members.

1.2 I-joists

Wooden I-joists assemblies (see Figure 2) are lightweight structural elements used in timber frame construction. I-joists are composed of two flanges and a web.

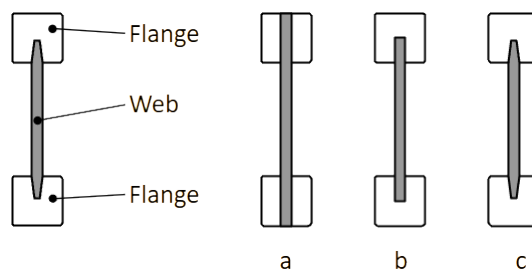


Figure 2. I-joist components (left) and different shapes (right): (a) glued thin webbed beam, (b) rectangular groove, (c) trapezoidal groove (I-Joists, n.d.).

I-joists are typically produced in factories. The most common shape is shown in Figure 2c. The flanges are most often made from strength-graded sawn wood or LVL and the web is a wood-based board (OSB, fibreboard, plywood). Melamine urea formaldehyde (MUF) adhesives are most used in the grooved joints and, if necessary, the finger-jointed sawn wood flanges. I-joists are appropriate for use in walls and floors and also as roof beams in service class 1 and 2. (*The I-Joist Handbook by Masonite Beams*, 2022)

I-joists are produced in a variety of sizes. The total depth of the joist is typically in the range of 200 to 500 mm. Flange widths are roughly 38 to 100 mm. Joist lengths are typically up to 13 m. (*I-Joist - APA – The Engineered Wood Association*, n.d.; *Technical Guide STEICOconstruction*, 2024; *The I-Joist Handbook by Masonite Beams*, 2022)

1.2.1 Bending capacity of I-joists at ambient conditions

The design of I-joists at ambient conditions is described in EN 1995-1-1:2004 (CEN, 2004b) and FprEN 1995-1-1:2025 (CEN, 2025a). Wooden I-joists in bending should be calculated as glued thin-webbed beams. The following subchapter summarises the main principles of verification of the load-bearing capacity of glued thin-webbed beams.

The aforementioned standards assume a linear strain variation across the cross-section depth. The mean and maximum axial tensile and compressive stresses and the lateral

instability of the compressive flange should be checked. The axial compressive and tensile stresses of the web should be checked. The strength of all bonds should be verified.

The section 8.4.1 of FprEN 1995-1-1:2025 (CEN, 2025a) provides some simplified expressions for the relative slenderness ratio and the buckling analysis of the web.

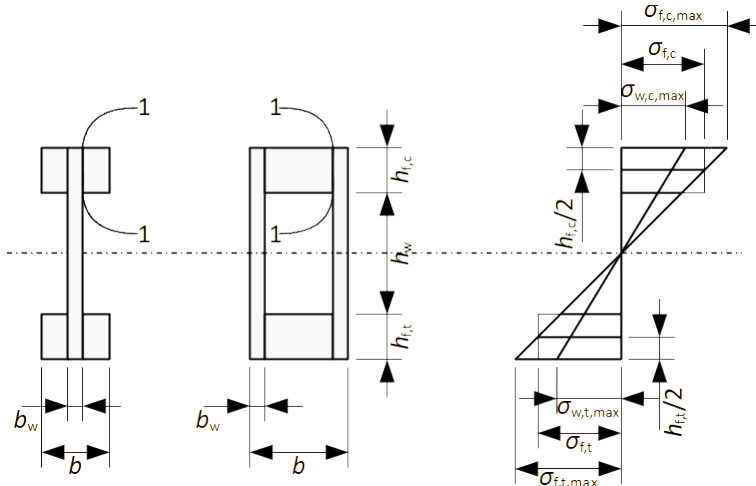


Figure 3. Thin-webbed beams EN 1995-1-1:2004 (CEN, 2004b).

The I-joists described in FprEN 1995-1-1:2025 (CEN, 2025a) have a slightly different configuration to those commonly in production today. Factory-produced I-joists typically have a tapered groove glued joint between the web and the flange (see Figure 2 right).

The axial stresses in the webs should be checked against the design axial strengths of the web material. Unless other values are given, the design in-plane bending strength of the webs should be taken as the design tensile or compressive strength. The strength of bond lines should be verified; however, no specific rules are given in the standard.

The standard provides a simplified verification for lateral buckling analysis of the web for I-joists with a clear distance between flanges less than 70 times the web thickness.

Additionally, the shear stress in section 1-1 in Figure 3 should be checked to be less than the rolling shear strength of the wood-based web material.

This section of FprEN 1995-1-1:2025 (CEN, 2025a) does not differ significantly from the previous version EN 1995-1-1:2004 (CEN, 2004b). Minor adjustments have been made in the naming and wording. The use of I-shaped members as compression elements is not explicitly included, however, section 8.2 of FprEN 1995-1-1:2025 (CEN, 2025a) gives ample provisions for member buckling verification.

1.3 Buckling at ambient conditions according to FprEN 1995-1-1 Annex B

Annex B of FprEN 1995-1-1:2025 (CEN, 2025a) is an informative annex titled “Additional information to Structural Analysis”. Section 3 of the annex provides further information regarding the stability and bracing of members and structural systems.

Subclause B.3.2.2 gives guidance on the evaluation of compressive members. The effective length may be calculated according to (1) as:

$$l_{c,y/z,ef} = k_{fb,y/z} \cdot l \quad (1)$$

where

- $l_{c,y/z,ef}$ is the effective length for lateral buckling about the respective axis [mm];
- $k_{fb,y/z}$ is the factor accounting for the influence of boundary conditions, for lateral buckling about respective axis [-];
- l is the length of the member [mm].

The critical load of unbraced members subjected to constant compressive force may be calculated according to (2) as:

$$N_{y/z,crit} = \pi^2 \cdot \frac{E_0 \cdot I_{y/z}}{l_{c,y/z,ef}^2} \quad (2)$$

where

- $N_{y/z,crit}$ is the critical load [N];
- E_0 is the modulus of elasticity parallel to grain [N/mm²];
- $I_{y/z}$ is the second moment of inertia about the respective axis [mm⁴].

The following is a summary of the subclause B.3.3.5 “Braced compressive members on smeared elastic restraints (elastic foundation)”. In the fire scenario after the fall-off of the fire protection system (protective board), the fire exposed flange becomes unbraced. This flange can be considered to have a smeared restraint against lateral buckling provided by the web and the unexposed flange acting as an elastic foundation, see Figure 4.

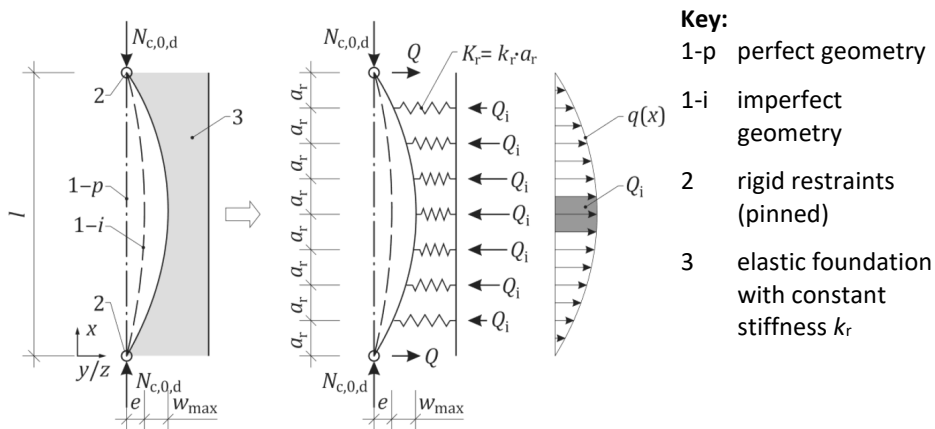


Figure 4. Compressive member on smeared elastic restraint (Figure B.10 of FprEN 1995-1-1:2025 (CEN, 2025a)).

The standard provides expressions for the determination of the effective length of the compression member depending on the spring stiffness of the elastic foundation based on the buckling mode (number of half sine waves). If the number of half-sine waves is not prescribed, the ratio of the member length and effective length may be approximated from formula (B.25) in the standard as shown in (3):

$$\frac{l}{l_{\text{ef}}} \cong \sqrt[4]{1 + \frac{4}{\pi^2} \cdot K_{\text{rel}}} \quad (3)$$

with

$$K_{\text{rel}} = \frac{k_r l^2}{N_{\text{crit},0}}$$

where

- l is the total length of the column [mm];
- l_{ef} is the effective length of the column [mm];
- K_{rel} is the relative stiffness [-];
- k_r is the spring stiffness of the smeared restraint [N/mm²];
- $N_{\text{crit},0}$ is the critical (Euler) force of the unbraced member [N].

1.4 Fire design methods for timber frame assemblies

There are two options for calculating the load-bearing capacity of a timber member in fire listed in the current version of the European standard for fire design of timber structures EN 1995-1-2:2004 (CEN, 2004b). These are the reduced properties method (RPM) and the effective cross-section method (ECSM).

In the reduced properties method (RPM) the initial cross-section is reduced by the notional charring depth and the strength and stiffness properties of the remaining timber section are reduced using appropriate modification factors given for different cases. The RPM is not included in FprEN 1995-1-2:2025 (CEN, 2025b) as it has not been updated and expanded to be applicable to newer structures.

In the effective cross-section method (ECSM) the initial timber cross-section is reduced by an effective charring depth which consists of the notional charring depth and a zero-strength layer compensating for the loss of strength and stiffness of heated but uncharred wood. The remaining cross-section has the strength and stiffness properties of wood at ambient temperatures. In the next version only the ECSM will remain.

The advantage of using the ECSM is that the strength and stiffness properties of the timber members remain the same as at ambient conditions. For modern design software this means a much easier input of the structure where only the cross-section dimensions are changed.

In the following, the calculation of the notional charring depth and the principles of considering the loss of strength and stiffness in the RPM and ECSM are explained.

1.4.1 Charring

The basis of calculating the fire resistance of timber load-bearing elements is the calculation of the charring depth during a set fire exposure. Charring may be one- or two-dimensional, meaning that one or multiple adjacent timber surfaces are affected. The charring rates are valid for all orientations of the fire-exposed surface (e.g. vertical, horizontal, exposure from above, etc.). In principle, the calculation of charring depth is based on multiplying the charring rate by the duration of charring.

The calculation of char depth is an approximation of the real behaviour. For example, planar or rectangular cross-sections are considered to remain as such. Therefore, corner rounding and the natural variability of the charring rate is simplified in the calculations.

Charring rates may vary throughout the fire exposure, depending on the configuration of the structure (initially protected or unprotected) and the wood-based material.

One-dimensional charring is based on one-dimensional heat transfer under standard fire exposure of an unprotected semi-infinite timber slab without any fissures or gaps. The one-dimensional charring rate, also called the basic design charring rate, is given in the standard depending on wood species and timber material type (e.g. solid wood slabs or wood-based boards). Charring which starts with the fire exposure is considered to occur during the normal charring phase (Phase 1), see Figure 5a.

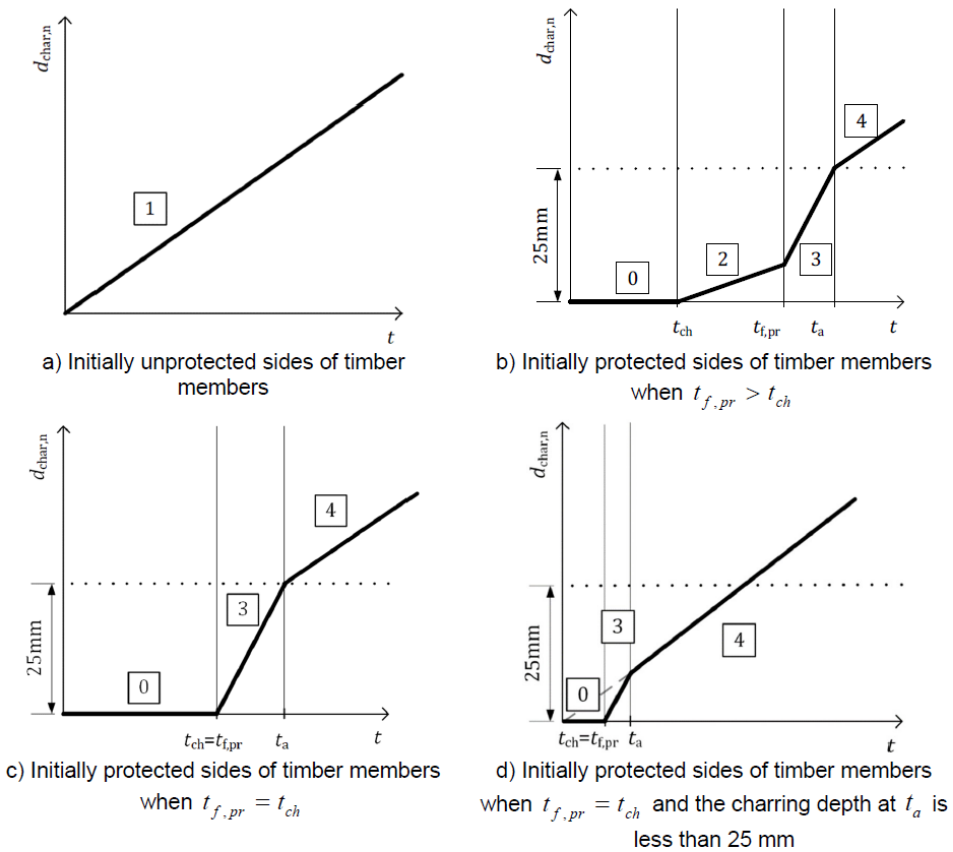


Figure 5. Charring phases of the European Charring Model, according to FprEN 1995-1-2:2025 (CEN, 2025b)

The one-dimensional charring depth $d_{char,0}$ is expressed as equation (4):

$$d_{char,0} = \beta_0 \cdot t \quad (4)$$

where

- t is the time of the fire exposure [min];
- β_0 is the one-dimensional charring rate perpendicular to the grain as shown in Table 3.1 of EN 1995-1-2:2004 (CEN, 2004c) [mm/min].

Heat transfer is two-dimensional near the corners of cross-sections, creating rounded corners on the uncharred cross-section. For simplicity in calculations this rounded cross-section is replaced by a rectangular one with an equivalent notional charring depth $d_{char,n}$ calculated according to (5):

$$d_{\text{char},n} = \beta_n \cdot t = \beta_0 \cdot k_n \cdot t \quad (5)$$

where

t is the time of the fire exposure [min];
 β_n is the basic design charring rate perpendicular to the grain given in Table 3.1 of EN 1995-1-2:2004 (CEN, 2004c) [mm/min].

The notional charring rate β_n can be expressed as (6):

$$\beta_n = k_n \cdot \beta_0 \quad (6)$$

where

k_n is the modification factor for corner rounding [-].

Structural timber members are often covered by one or multiple material layers which postpone the start of charring. Such members are called initially protected and undergo multiple charring phases according to FprEN 1995-1-2:2025 (CEN, 2025b). The charring of initially protected rectangular timber members in TFA is described in the following.

Start of charring is the point in time when the temperature on the timber surface reaches 300 °C. The charring phase between the start of the fire exposure and the start of charring (t_{ch}) is called the encapsulation phase (Phase 0). During this period, the timber cross-section does not decrease by charring. Figure 5b-d show different cases of initially protected cross-sections.

There are broadly two types of protection. The first kind will not maintain protective properties after the start of charring. The other type (also called fire protection materials, FPM) will remain in place and slow down the charring rate of timber members behind it until its failure time $t_{\text{f,pr}}$. The period of time between the start of charring and the failure time of the protection is called the protected charring phase (Phase 2).

The notional charring rate in Phase 2 depends on the thickness and material of the FPM. It is calculated according to (7):

$$\beta_n = k_2 \cdot k_{s,n,1/2} \cdot \beta_0 \cdot (t_{\text{f,pr}} - t_{\text{ch}}) \quad (7)$$

where

k_2 is the protection factor for Phase 2 [-];
 $k_{s,n,1/2}$ is the combined section and conversion factor for the fire exposed side or the lateral side [-];
 t_{ch} is the start time of charring [min];
 $t_{\text{f,pr}}$ is the failure time of the fire protection system [min].

The combined section and conversion factor $k_{s,n}$ considers the effect of the dimensions of the timber member on the charring rate. The factor for the fire exposed side $k_{s,n,1}$ depends on the width of the initial rectangular cross-section. The factor for the lateral sides $k_{s,n,2}$ depends on the depth of the initial cross-section.

Once the protection fails, the charring rate increases. Depending on the char depth and the characteristics of the timber member, the charring rate is approximated as linear or bilinear after the failure time. Phase 3 is called the post-protected charring phase, where charring is rapid until the end of the fire exposure or until the consolidation time t_a is reached. In phase 3, the timber member does not yet have a fully developed char layer. The notional charring rate in Phase 3 for TFA depends on the failure time of the fire protection system and the protection offered by the cavity insulation. It is calculated according to (8):

$$\beta_n = k_{3,1/2} \cdot k_{s,n,1/2} \cdot \beta_0 \cdot (t - t_{\text{f,pr}}) \quad (8)$$

where
 $k_{3,1/2}$ is the post-protection factor for Phase 3 for the fire exposed side or the lateral side [-];
 t is the time [min].

The post-protection factor is used to consider the increase of the charring rate after the failure of the fire protection system. The proper equation to calculate the factor is chosen based on the cavity insulation.

The last charring phase – consolidated charring phase (Phase 4) – begins at the consolidation time. In this phase the charring rate slows, often to the basic design charring rate. For TFA only the lateral sides can char in the consolidated charring phase, according to (9):

$$\beta_n = k_{s,n,1/2} \cdot \beta_0 \cdot t \quad (9)$$

where
 t is the time for the consolidated charring phase [min].

The consolidation time t_a is not applicable to TFA, however for larger cross-sections (especially plane timber members) the consolidation time is considered as the time when a 25-mm thick char layer has formed. This thickness is considered to offer enough protection to slow the charring rate to the basic design charring rate.

If a timber member is exposed to multiple charring phases, the notional char depths are summarised. The factors k_2 , $k_{s,n,1/2}$, $k_{3,1/2}$, etc are called the modification factors for charring in the FprEN 1995-1-2:2025 (CEN, 2025b).

Thermal insulation applied in the cavities of timber frame assemblies also influences the charring behaviour of the timber members. The protective properties of insulation materials affect the charring rate of the lateral sides of the timber member. Thermal insulation materials are divided into protection levels (PL) according to the test procedure in Annex D of FprEN 1995-1-2:2025 (CEN, 2025b). This approach was developed by Tiso (Tiso, 2018). The design approach is summarised in Publication I.

Protection level 1 (PL1) provides the most protection against side charring. An example of a PL1 insulation is traditional stone wool.

Protection level 2 (PL2) provides less protection against side charring and is exemplified by glass wool and wood-based insulations.

Protection level 3 (PL3) insulation materials are for example extruded polystyrene and other similar foams which melt in the cavities. Insulation materials which are not classified without further testing and which have not been classified as PL1 or PL2 are considered in calculations as PL3.

1.4.2 Mechanical resistance

Uncharred but heated wood does not exhibit full strength and stiffness. This loss in mechanical properties can be considered either by reducing the strength and stiffness properties (reduced properties method, RPM) or by reducing the cross-section dimensions by a zero-strength layer and assuming the strength and stiffness properties as at ambient conditions (effective cross-section method, ECSM).

The RPM is valid for rectangular or round cross-sections. The reduction factors are given based on the duration of the fire exposure (less or greater than 20 min) and the loading conditions (bending, tension, compression). The values depend on the perimeter and area of the reduced cross-section.

The reduced cross-section method in EN 1995-1-2:2004 (CEN, 2004c) has not been improved since the 90s and is, therefore, rather limited. Only 7 mm is provided as the universal value for the zero-strength layer d_0 . However, this is even further limited to use with larger cross-sections and not TFA. For fire exposure less than 20 minutes for initially unprotected members and less than the start time of charring for initially protected members, the zero-strength layer depth should be interpolated between 0- and 7-mm.

The calculation methods for TFA have been improved and new parameters have been developed since the publication of EN 1995-1-2:2004. These have been detailed in Fire Safety in Timber Buildings (Östman et al., 2010) and the Doctoral Thesis of Mattia Tiso (Tiso, 2018). These improvements will be summarised below, with a focus on timber frame assemblies.

Fire Safety in Timber Buildings (Östman et al., 2010) provides values for d_0 for beam and stud elements of timber frame assemblies which were derived from the RPM results. These are significantly higher than the 7 mm for larger timber cross-sections. The values are dependent on the dimensions of the rectangular timber element.

The Doctoral Thesis of Mattia Tiso (Tiso, 2018) provides more specific values for the zero-strength layer depth depending on the type of insulation, the load direction and the dimensions of the timber member. An additional optimised approach is also given, which considers the start time of charring and the failure time of the cladding. The optimised approach accounts for the changing of the zero-strength layer depth with time of fire exposure.

The influence of adhesives in (Östman et al., 2010) is only discussed in connection to cross-laminated timber where the softening of adhesive bonds is considered through a higher charring rate and a compensation layer for strength and stiffness.

1.4.3 Separating function method

The standard FprEN 1995-1-2:2025 (CEN, 2025b; Mäger et al., 2019) describes the separating function method (SFM, formerly known as the Component Additive Method) for the verification of the separating function or the calculation of the start time of charring behind protection. The method is valid for the standard fire exposure. Essentially, this method considers the contribution of each layer to the insulation time of the whole assembly (see Figure 6).

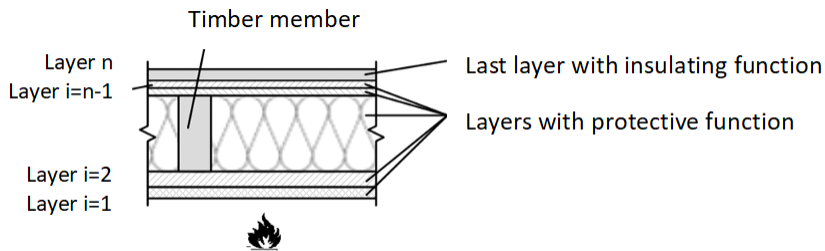


Figure 6. Numbering and function of the layers in a timber frame structure.

The layers fulfil different functions (Figure 6). The last layer of the assembly on the fire-unexposed side serves an insulating function (insulation time) while the previous layers have a protective function (protection time). These functions are defined by different temperature criteria on the fire-unexposed side of the considered layer.

The protection time $t_{\text{prot},i}$ is the time until the temperature rise on the fire-unexposed side of the considered layer is (1) 250 K on average or (2) 270 K at any point. Ambient conditions are usually 20 °C, hence the temperature criteria become 270 °C and 290 °C, respectively. These criteria are approximations to account for the failure of thermally degraded material layers. They are also close to the charring temperature of timber (300 °C). Therefore, the sum of protection times of the layers preceding the timber elements may be used as a slightly conservative value for starting time of charring.

The insulation time $t_{\text{ins},n}$ of the last layer of the assembly is the time until the temperature rise on the fire-unexposed side is equal to 140 K on average over the whole area and 180 K at any point. These criteria are in line with the insulation requirements set in the standard EN 13501-2:2023 (CEN, 2023). The temperature limitation on the fire-unexposed surface of the structure should prevent the ignition of nearby objects.

The fire resistance time of the timber assembly is the sum of the contributions from the different layers as shown in equation (10) (layer naming according to Figure 6).

$$t_{\text{ins}} = \sum_{i=1}^{i=n-1} t_{\text{prot},i} + t_{\text{ins},n} \quad (10)$$

where

t_{ins} is the insulation time of the assembly [min];
 $t_{\text{prot},i}$ is the protection time of the layer i [min];
 $t_{\text{ins},n}$ is the insulation time of the last layer of the assembly on the unexposed side [min].

The protection and insulation times of the material layer can be calculated taking into account the basic values of the layers, the position coefficients and joint coefficients by equations (11) and (12).

$$t_{\text{prot},i} = (t_{\text{prot},0,i} \cdot k_{\text{pos,exp},i} \cdot k_{\text{pos,unexp},i} + \Delta t_i) \cdot k_{j,i} \quad (11)$$

$$t_{\text{ins},n} = (t_{\text{ins},0,n} \cdot k_{\text{pos,exp},n} + \Delta t_n) \cdot k_{j,n} \quad (12)$$

where

$t_{\text{prot},0,i}$ is the basic protection time of the layer i [min];
 $k_{\text{pos,exp},i}$ is the position coefficient for the fire exposed side of the layer i [-];
 $k_{\text{pos,unexp},i}$ is the position coefficient for the unexposed side of the layer i [-];
 Δt_i is the correction time of the layer i [min];
 $k_{j,i}$ is the joint coefficient of the layer i [-];
 $t_{\text{ins},n}$ is the insulation time of the last layer n [min];
 $t_{\text{ins},0,n}$ is the basic insulation time of the last layer n [min];
 $k_{\text{pos,exp},n}$ is the position coefficient for the fire exposed side of the last layer n [-];
 Δt_n is the correction time of the last layer n [min];
 $k_{j,n}$ is the joint coefficient of the last layer n [-].

The correction time is added only until the fall-off of the fire protection system according to (Mäger et al., 2017).

The SFM tends to be more conservative for longer fire exposures and after the failure of the fire protection system. Therefore, it is important to follow the detailing rules of FprEN 1995-1-2:2025 (CEN, 2025b) to ensure the proper fixation of the fire protection system as the performance of it has the greatest influence on the charring and load-bearing capacity of timber members of frame assemblies.

1.5 Fire design of wood-based I-joists in floors

The fire design model for simply supported floor structures with wooden I-joists as the load-bearing elements is published in Fire Safety in Timber Buildings (Östman et al., 2010) based on the work of König (König, 2006).

The model for floors is compatible with EN 1995-1-2:2004. The behaviour of I-joists in fire was investigated using thermal and mechanical simulations. The protection by claddings is considered by the fall-off time and protection coefficients. It is assumed that the structure with I-joists is protected on both sides by a cladding of gypsum plasterboard or wood-based panels. The cavities formed between the load bearing I-joists and claddings are assumed to be completely filled with batt-type stone wool or glass wool insulation. Moreover, the model is only valid until fall-off of the cladding if glass wool is used as insulation. The model provides different formulae for calculating the fire resistance, depending on whether the failure occurs in the protected or post-protected phase.

The charring model proposed by König considers charring only on the fire exposed side of the fire exposed flange. The charring rate depends on the width of the flange.

The reduced bending capacity of I-joists in fire is considered by a modification factor which depends on the char depth and the dimensions of the flange and the I-joist cross-section.

König sets forth expressions for the calculation of the shear capacity of the web depending on the char depth and the cross-section width.

The behaviour of adhesives in finger-joints is considered for PRF (phenolic resorcinol formaldehyde), MUF (melamine urea formaldehyde) and PUR (polyurethane) adhesive groups by a modification factor.

The modification factors for the reduced properties method have been recalculated as the zero-strength layer depth in Fire Safety in Timber Buildings for assemblies insulated with stone wool.

1.6 Fire design of wood-based I-joists in walls

The design model for fire exposed wooden I-joists in wall assemblies was developed at SP Wood Technology (Schmid et al., 2011).

The design method for walls gives the relevant parameters for the RPM. It is valid for wall structures where the cavities are partially or completely filled with batt type mineral wool. Cavity insulation batts with a thickness less than 120 mm need additional mechanical fixation. The model is valid for structures with partial insulation with a thickness of at least 100 mm. Batts with a thickness of more than 120 mm are assumed to stay in place without additional mechanical fixation. Traditional glass wool products can be considered in the calculations only before the failure of the cladding. Additionally, the flanges must be made of solid timber of C30 strength class.

The charring model provides similar expressions to König. However, the factor considering the effect of the width of the flange is different, which is not in agreement with the assumption that fire exposure is similar in all directions.

(Schmid et al., 2011) conducted model-scale furnace fire tests on beams with the compression flange exposed to fire. This configuration was used as a substitute for full-scale wall fire tests. From these tests, the modification factor for bending strength and stiffness was derived. The effect of adhesives in finger-joints is the same as for floor assemblies.

1.7 Database of previous test results

In the following the available tests performed with I-joists are summarised. Test data was gathered from producers (Masonite Beams AB, Steico SE) and RISE Research Institutes of Sweden. A table was sent to producers who could fill it in with relevant data to this study (see Appendix 4). Furnace fire tests where the furnace was not controlled by plate thermometers according to EN 1363-1:2020 (CEN, 2020) have been excluded.

1.7.1 Model-scale furnace fire tests

Two reports of model-scale furnace fire tests were available featuring a total of 14 tests. The tests were all conducted in Stockholm in a cubic metre furnace following the standard fire curve. All tests were conducted on a horizontal beam in bending with either the tension (TSW) or compression (CSW) side exposed to fire.

All tested joists had a total cross-section depth of 200 mm, 47x47 mm flanges of C30 sawn timber and 10-mm thick wood fibreboard web. The cavities were insulated with rectangular slabs of stone wool. Strips of glass wool were placed between the flanges, the web and the cavity insulation to protect the web.

The overview of model-scale furnace fire tests is given in Table 1. The load per stud represents the load ratio in fire to the ambient load bearing capacity.

Table 1. Model-scale tests.

No	Loading	Load (per stud)	Cavity insulation	Protection type and thickness [mm]	Report
1	CSW	32,7%	SW	GtF 15	SP: 2011:27
2	CSW	28,2%	SW	GtF 15	SP: 2011:27
3	CSW	15,6%	SW	GtF 15	SP: 2011:27
4	CSW	11,4%	SW	GtF 15	SP: 2011:27
5	CSW	8,7%	SW	GtF 15	SP: 2011:27
6	CSW	4,2%	SW	GtA 12,5	SP: 2011:27
7	CSW	15,0%	SW	GtA 12,5	SP: 2011:27
8	CSW	15,9%	SW	GtF 15+ GtA 12,5	SP: 2011:27
9	TSW	35,6%	SW	GtA 12,5	SP: 2011:27
10	TSW	31,3%	SW	GtF 15	SP: 2011:27
11	TSW	38%	SW	GtF 15	SP: 3P04455
12	TSW	40%	SW	GtF 15	SP: 3P04455
13	TSW	40%	SW	GtF 15	SP: 3P04455
14	TSW	40%	SW	GtF 15	SP: 3P04455

1.7.2 Full-scale furnace fire tests

23 full-scale furnace fire tests of floor structures (F) and 17 full-scale wall tests (W) were available.

The I-joist profiles tested are summarised in Table 2.

Table 2. I-joist profiles tested in full-scale.

No	I-joist height, mm	I-joist distance, mm	Flange width, mm	Flange height, mm	Flange material	Web thickness, mm	Web material
F1	220		45	39	LVL	8	HB.HLA1
F2	240		45	39	LVL	8	HB.HLA1
F3	250	600	47	47	C30		
F4	200	600	47	47	C30		
F5	200	600	47	47	C30		
F6	300	600	47	47	C30		
F7	220	400	47	47	C30	10	OSB
F8	220	600	47	47	C30	10	OSB
F9	220	400	47	47	C30	10	OSB
F10	240	600	47	47	C18	10	OSB
F11	240	600	45	36	LVL	10	OSB3
F12	220	600	45	45	LVL		
F13	220	600	47	44	C24	9.5	OSB3
F14	240	600	45	36	LVL	10	OSB3
F15	220	600	45	36	LVL	10	OSB
F16	300	600	47	47	C30	10	OSB
F17	240	600	45	36	LVL	10	OSB
F18	235	600	47	45	C24	9.2	OSB
F19	235	600	47	45	C24	9.2	OSB
F20	220	600	45	36	LVL	9	OSB3
F21	220	600	45	36	LVL	9	OSB3
F22	240	600	45	36	LVL	10.2	OSB3
F23	235	600	47	45	C24	9.2	OSB
W1	160		60	45	LVL	6.7	HB.HLA1
W2	160		60	39	LVL	6.7	HB.HLA1
W3	160		60	39	LVL	6.7	HB.HLA1
W4	160		60	39	LVL	6.7	HB.HLA1
W5	160		60	45	LVL	6.7	HB.HLA1
W6	160		60	39	LVL	6.7	HB.HLA1
W7	250	600	47	47	C30	10	WFB
W8	250	600	47	47	C30		
W9	200	600	47	47	C30		
W10	200	600	47	47	C30		
W11	200	600	47	47	C30		
W12	200	600	47	47	C30		
W13	200	600	70	47	C30	10	OSB3
W14	250	600	70	47	C30	10	OSB3
W15	200	600	47	47	C18	10	OSB
W16	200	600	47	47	C30	8	WFB
W17	250	600	47	47	C30+	10	OSB3

Table 3 shows the results of the full-scale furnace fire tests obtained from producers. The loads shown in the rightmost column are shown as uniformly distributed over the floor area or the wall width unless otherwise noted. All symbols are shown above in chapter "Abbreviations".

Table 3. Full-scale fire test results.

No	Test report	Fire protection type and thickness in mm	Cavity insulation (thickness in mm)	Fall-off time, min	Time to failure, min	Load, kN/m or kN/m ²
F1	Y 2118-3E-RA-001	GtA15	Void	28	34	1.03
F2	LP01-01565/14/Z00 BP	GF12.5+GF12.5	WF (100)	63	70	1.5
F3	SP4P04534-04-1-2	2GF12.5	WF (250)	44	61	1.35
F4	SPFR 150011-02B	GF15+GF12.5	WF (200)	59	65	1.35
F5	SPFR 1500112A	GtA12.5	WF (200)	22,5	33	1.35
F6	SINTEF	GtA15	SW (300)	15	29	2.7
F7	RISEFR 150011-08	GtA15	Void	27	31	1.5
F8	RISEFR 150011-06	GtA15	Void	25	30	0.7
F9	RISEFR 150011-05	GtA15	Void	27	30	1.0
F10	RISEFR 150011-09	2GtA15+Btn16	GW (100)	58	73	1.5
F11	2020-Efectis-R000333	GtA15	Void	29	34	1.02
F12	CERIB 021968	GtA15	SW (45)	31	35	1.06
F13	LIEGE EF/FH/1420	GtA15	Void	37	37	1.09
F14	2020-Efectis-R000334	GtA15	Void	29	34	1.02
F15	WF 428777	GtA15	Void	24	30	1.0
F16	RISEFR 150011-16A	GtF15+GtA12.5	GW (100)	65	65	1.5
F17	PEUTZ Y 2142-3E-RA-002	2GtF15	GW (100)	41	75	1.7
F18	PEUTZ Y 2153-3E-RA-001	GtA15	Void	37	39	1.02
F19	PEUTZ Y 2154-3E-RA-001	2GtF15	GW (100)	78	82	1.36
F20	PEUTZ Y-2510-3E-RA-001	2GtA15	Void	52	72	1.7
F21	PEUTZ Y 2533-4E-RA	GtA15	Void	28	33	1.12
F22	PEUTZ YA 1916-1E-RA-001	GtA15	Void	22	30	1.02
F23	PEUTZ YA 2153-1E-RA-001	GtA15	Void	NA	39	1.02
W1	PB 3.2/12-050-1	CP7+WFB60	WF (160) ¹	84	99	16.8
W2	PB 3.2/14-202-1	GtA9.5+OSB12	WF (160) ¹	30 ²	45	16.8
W3	PB3.2/13-181-2	GF12.5	WF (160) ¹	28	35 ³	17

W4	PB3.2/13-181-1	WFB35	WF (160) ¹	33	35 ³	17
W5	PB 3.2/09-275	GF18	WF (160) ¹	62	83	16
W6	PB 3.2/14-202-2	GtF15+GtF15+OSB12	WF (160)	82	120	22.5
W7	REI90 Borås 8.10.2018	2GtF15+Btn45	WF (250)	66	82,9	54 ⁴
W8	SP4P04534-04-1-1	GF9+GtA15	WF (250)	61	61	17 ⁴
W9	SP PX03681-01	GtA 12.5	SW (200)	21	57	22 ⁴
W10	RISEFR 150010-01A	GtF15+GtF12.5	WF (200)	77	85	22 ⁴
W11	RISEFR 150010-01A	GtF12.5	GW (250)	47	69	24 ⁴
W12	RISEFR 150010-01B	GtA12.5	WF (200)	27	40	17 ⁴
W13	RISEFR 150010-09	GtA12.5+GtF15 + Btn34	GW (245)	102	113	50 ⁴
W14	RISE 8P06896	2GtA12.5	CF (250) ¹	48	82	54 ⁴
W15	RISEFR 150010-05	GtA12.5	GW (200)	NA	69	120
W16	SP PX03861-01	GtA12.5	SW (220)	19	57	22 ⁴
W17	RISEFR 150010-06	2GtF15	CF (250) ¹	74	121	48 ⁴

Notes:

¹ loose fill or blown in insulation

² fall-off determined by rapid temperature rise

³ test stopped without structural failure

⁴ load per stud

1.8 Knowledge gaps

Fire resistance calculation methods for wooden I-joists as described above in chapters 1.5 and 1.6 do not meet the needs of today's building market. The materials used in conjunction with I-joists in TFA have been improved and more complex systems are used. Additionally new and improved design approaches are included in the updated FprEN 1995-1-2:2025 (CEN, 2025b) for which there is no data about I-joists. This subchapter describes and extends the gaps identified in Publication IV.

The fire design method for floors with I-joists was developed by König (König, 2006). The behaviour of I-joists in bending was investigated numerically. Although finite element modelling is a valid tool to investigate the behaviour of structures with well-known properties from fire testing, the results should always be validated by test results. In the report (König, 2006), no validation of the calculation model with full-scale furnace fire tests is provided.

The existing floor design model provides different formulae for calculating the fire resistance, depending on whether the failure occurs in the protected or post-protected phase. This approach is not different from the fire design models for standard fire in the FprEN 1995-1-2:2025. Additionally, König has proposed to use an effective failure time for claddings as 90% of the failure time for timber frame assemblies with rectangular members. The reasoning behind this assumption is unclear.

The model by König includes modification factors for strength of I-joists for three different adhesive families. More recent research has shown that differences in performance exist within adhesive families. Therefore, a more detailed approach could be developed based on performance, rather than adhesive types.

The fire design method for walls with I-joists was developed at SP Wood Technology (Schmid et al., 2011) based on model-scale testing and numerical investigations. The design model follows the RPM approach.

Interestingly, the wall model includes a different conversion factor to find the equivalent rectangular cross-section. This is not in agreement with the principles of FprEN 1995-1-2:2025 where it is stated that the fire exposure is not dependent on the orientation of the structure. Therefore, a harmonisation of the wall model with the current standards could be possible.

The wall model by Schmid includes the same modification factors for the strength depending on the adhesive used in the finger joints. It is unclear if adhesive softening in the compression members influences the load-bearing capacity.

Buckling of I-joists in the fire situation has not been sufficiently investigated. More specifically, there is little information and calculation guidance for the case where fall-off of claddings has occurred on the fire exposed side regarding buckling capacity of I-joists.

Both these models include many coefficients to calculate the char depth of the flange of an I-joist. These coefficients are different from those used for rectangular members. Moreover, they do not harmonise with the design model by Tiso (Tiso, 2018). Another limitation of the models by König (König, 2006) and Schmid (Schmid et al., 2011) is the narrow choice of insulation materials. More insulation and cladding materials should be included, based on the work of Tiso.

The models described above are not following the principles of the European Charring Model and the Effective Cross-Section Method and consider only a narrow range of cavity insulations. There are no widely available fire resistance design models for walls with I-joists which consider buckling.

1.9 Objectives and scope

This subchapter defines the objectives and scope of the thesis. A brief outline is given for the approaches to reach the objectives.

The main goal of the thesis is the development of a fire design model for wooden I-joists in bending and compression. This model is aimed to follow the Effective Cross-Section Method in order for it to be fully compatible and harmonised with the updated FprEN 1995-1-2:2025. The new method should be open to new materials and further improvements in the future. The fire design method developed within this thesis shall include a novel and detailed buckling calculation approach. The effect of adhesives in the finger joints of the tension flange will be considered based on adhesive performance and not only adhesive families.

The model is developed based on normal temperature testing, model-scale furnace fire testing and numerical methods. The model is validated with a database of full-scale furnace fire test results.

This thesis is focused on wooden I-joists exposed to the ISO 834 standard fire curve. I-joists with steel or truss webs are out of the scope of this work. The design model developed within this thesis is valid for I-joists as the load-bearing members in timber frame floor and wall assemblies with cavity insulation. Void cavities have not been explicitly investigated.

2 Methodology

This chapter provides an overview of the methods used and the steps taken during the preparation of the experimental and numerical investigations in this thesis. Specifics and details will be described in the following, in chapters 3 and 4. The procedure for the development of the equations to calculate the char depth and the depth of the zero-strength layer is shown as a flowchart in Figure 7.

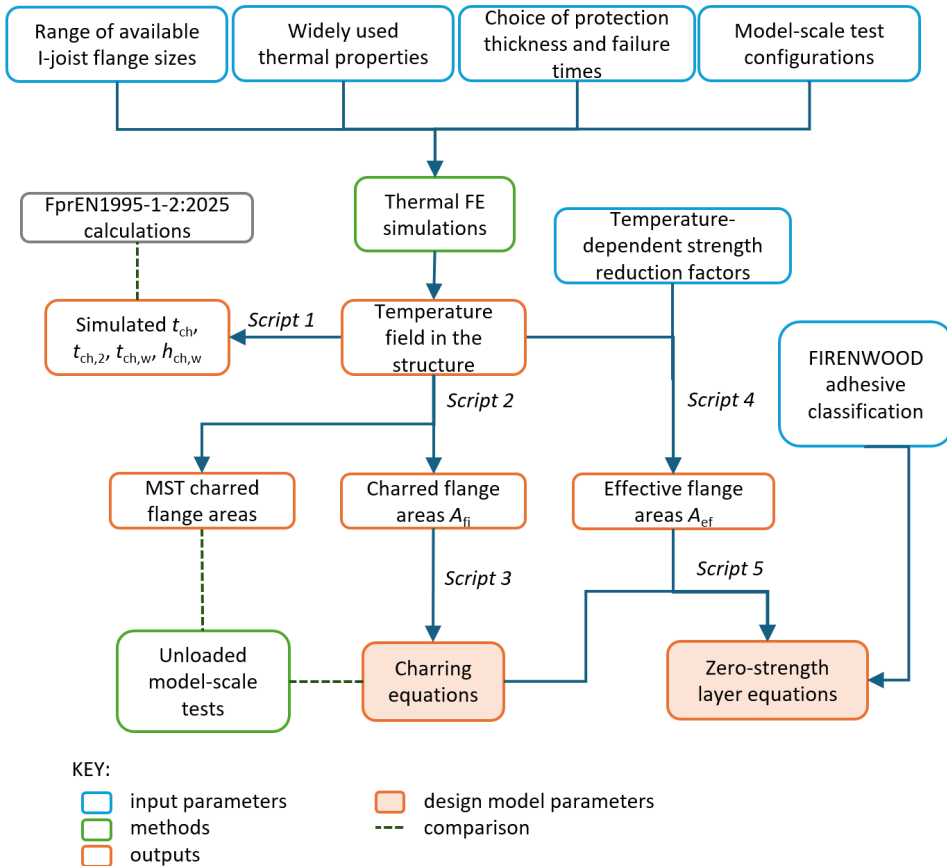


Figure 7. Flowchart of the procedure to develop charring and zero-strength layer equations.

First, thermal FE simulations were conducted with typical I-joint sizes and common fire protection systems. These are described further in chapter 3.2. The purpose of thermal simulations was the investigation of the temperature development in different sized flanges with two types of cavity insulation. Based on the temperature fields at every time step, the significant times which separate different charring phases and the charred flange areas were extracted. The charred areas were the basis for developing the modification factors for charring rates for different charring phases.

Unloaded model-scale furnace fire tests were conducted to measure the temperature development in a part of a timber frame assembly with I-joists. These temperatures were compared to simulations. The remaining charred areas were used to validate thermal simulations and the char depth calculations according to the design model.

The configurations tested in unloaded model-scale tests (as described in chapter 3.1) were also simulated. The simulation results were compared to the temperatures measured in the tests and the charred areas of the flanges after the test. The purpose of this comparison was to validate the results of the thermal simulations.

Then, the temperature fields in the fire exposed flange obtained from the thermal FE simulations were substituted with the reduction factors for tensile and compressive strength in FprEN 1995-1-2:2025 (CEN, 2025b). The results are temperature-dependent strength distributions in the flange. The effective areas were calculated with the purpose of developing the expressions to calculate the depth of the zero-strength layer.

The further steps taken to develop the complete design model are shown as a flowchart in Figure 8.

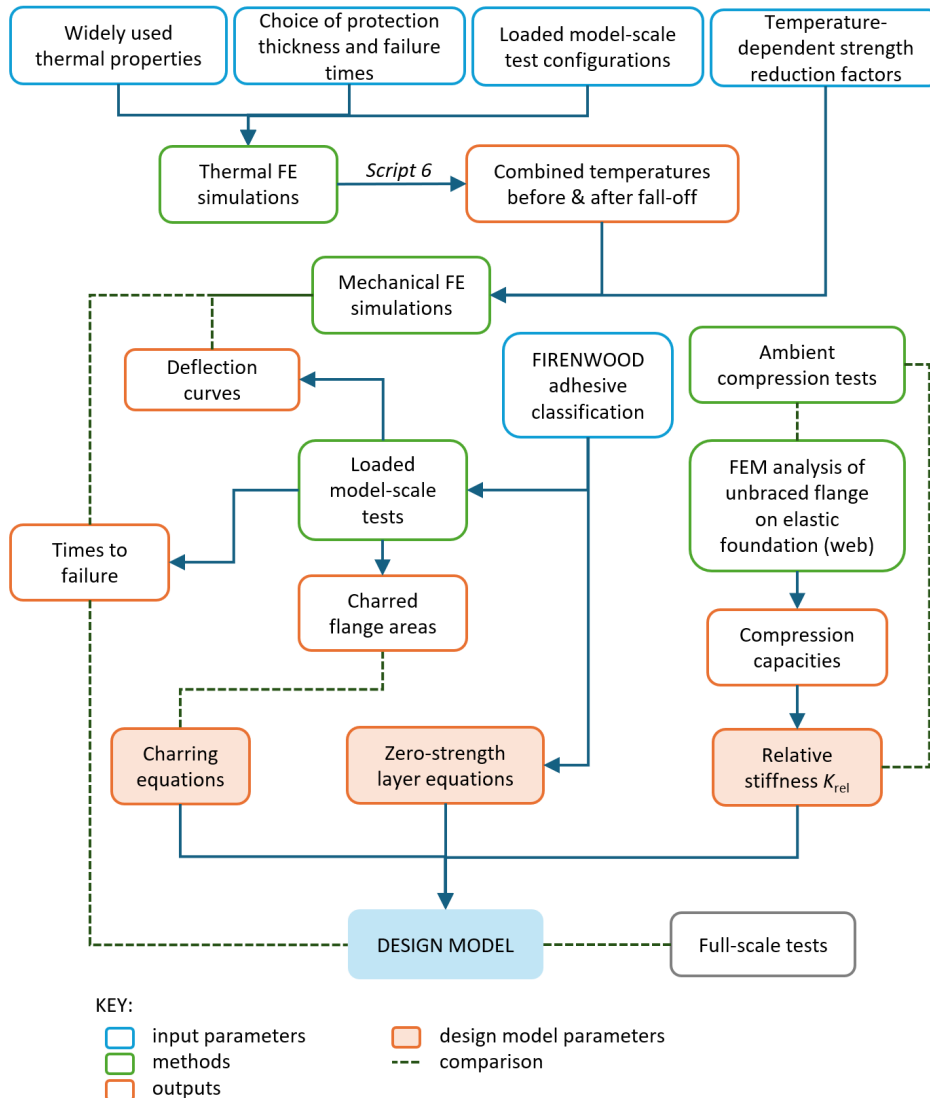


Figure 8. Flowchart of the procedure for the development of the design model.

The mechanical response of I-joists was investigated by FE simulations, loaded model-scale furnace fire tests and compression tests at normal temperature. Thermo-mechanical FE simulations were conducted. Based on the comparison of the deflections from the simulations and loaded model-scale tests, the FE results were not suitable to conduct a further parametric study. The times to failure from FE simulations and the design model were compared.

Loaded model-scale furnace fire tests were conducted within the FIREWOOD project with the aim of investigating the behaviour of different adhesives in the finger joints of the tension flanges of I-joists. The results were used to validate the FE simulations and the design model.

The compression of I-joists was investigated by testing and numerical methods. Normal temperature (ambient) compression tests were conducted on a variety of configurations to investigate the effect of I-joist dimensions and bracing conditions on the compression capacity. Numerical investigations were validated with tests and further configurations were simulated to expand the results.

3 Investigation of charring behaviour

The following chapter describes the steps taken to develop the charring model and the parameters shown in Chapter 5.1. Charring behaviour of I-joists was investigated by unloaded model-scale furnace fire tests and finite element (FE) simulations.

3.1 Unloaded model-scale tests

Unloaded model-scale tests were conducted to investigate the temperature development in the specimen. Different factors such as the flange dimensions, type of thermal cavity insulation and test duration were varied. The results of MST were used to validate the thermal simulations and the modification factors for charring.

3.1.1 Methodology

Six horizontal model-scale fire tests have been conducted in a cubic metre furnace at RISE in Borås, Sweden. A total of 12 I-joists from different producers were tested. All tests followed the ISO 834:1999 (ISO, 1999) standard time-temperature curve as fire exposure.

The inner dimensions of the test furnace are 1x1x1 m³. The furnace temperature is controlled by two plate thermometers according to EN 1363-1:2020 (CEN, 2020). In this test series, horizontal tests were conducted where the specimen was placed on top of the furnace with the fire exposure from below the structure.

The purpose of the model-scale tests (MST) was to investigate the charring behaviour of I-joists with stone wool (SW) and glass wool (GW) insulation in the cavities. The aim in this test series was to study the behaviour of I-joists in different charring phases. An overview of the tested configurations is given in Table 4.

Table 4. Unloaded model-scale furnace tests.

Test no	Beam B1				Beam B2				Insulation
	Flange width b_f (mm)	Flange depth h_f (mm)	Flange material	Web Material (thickness, mm)	Flange width b_f (mm)	Flange depth h_f (mm)	Flange material	Web material (thickness, mm)	
T1	47	47	C30	OSB3(10)	97	47	C30	OSB3(10)	GW
T2	47	47	C30	OSB3(10)	97	47	C30	OSB3(10)	SW
T3	45	36	LVL	OSB3(10)	96	39	LVL	OSB3(10)	GW
T4	45	36	LVL	OSB3(10)	96	39	LVL	OSB3(10)	SW
T5	47	45	C24	OSB3(9)	97	45	C24	OSB3(9)	SW
T6	90	39	LVL	HB.HLA1(8)	97	45	C24	OSB3(9)	SW

In all tests, the total depth of the I-joist was 220 mm (see Figure 9). The cavities were completely filled with thermal insulation. The insulation batts were cut to the shape of the I-joists with ~5 mm oversize. Insulation batts were cut to shape manually due to the uncommon width of the cavities in the specimen. For common framing distances (e.g. 400 and 600 mm) insulation manufacturers provide factory cut batts with I-joist shaped edges.

The top surface of the specimen was covered by a wood-based board (plywood or fibreboard, thickness at least 15 mm). The fire exposed surface was initially protected by a 15 mm thick fire rated (type F according to EN 520:2004 (CEN, 2004a)) gypsum plasterboard.

The specimen was enclosed in a frame made from sawn timber or glulam with a depth of 220 mm (see Figure 9). The test specimens each had two I-joists which were instrumented with thermocouples (TC). I-joists B1 and B2 may have different sizes according to Table 4.

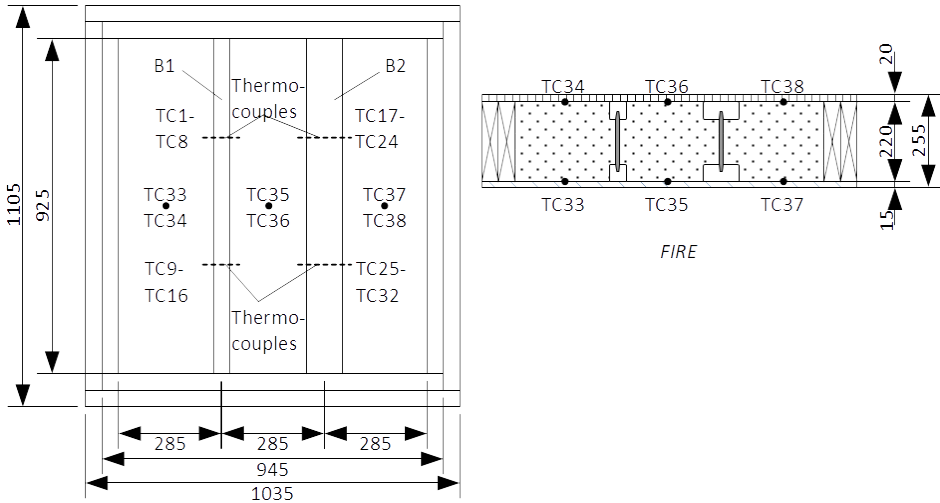


Figure 9. Plan (left) and section (right) views of the model-scale test specimen.

Type K thermocouples according to IEC 60584-1:2013 (IEC, 2013) were used to measure temperatures in the two I-joists during the test. Some thermocouples were drilled into the centre of the width of the flange (see Figure 10) using a 2 mm drill bit in a drill press. The holes were placed in a zig-zag pattern on the side of the flange to limit interference of heat flux between holes (Figure 11 left). The tips of the TC were exposed of insulation and twisted together about 5 mm. Thermocouples on the top corner and on the web were lightly fixed with paper tape to ensure that they would not be shifted when installing the thermal insulation. The TC wires were stapled to the joists and guided towards the unexposed side.

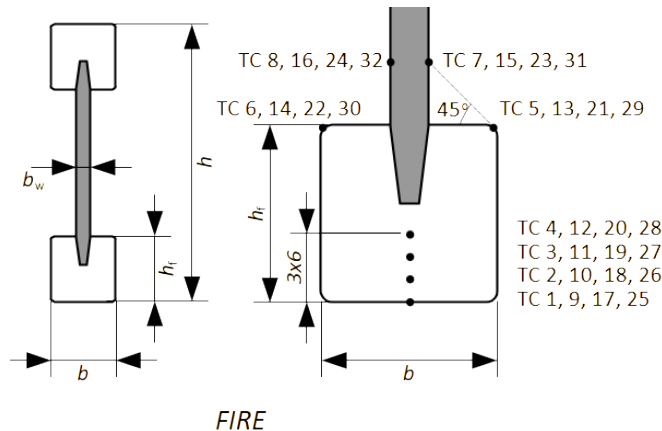


Figure 10. Thermocouple placements on tested I-joists.

The gypsum boards on the fire exposed side were fixed with screws at approximately 30 cm distance in both directions. Test 2 had screws with a length of 51 mm. Relatively short screws (33 mm) were used in all other tests to ensure a reasonably short fall-off time of the gypsum board. Fall-off time of fire protection systems cannot be investigated in furnaces which are smaller than full-scale according to EN 13381-7:2019 (CEN, 2019).

The edges of the specimen were covered with strips of the same gypsum board to reduce the risk of hot gasses or flames escaping the furnace from the supported sides of the specimen. No caulking was applied. Furthermore, the inside and outside joints in the outer frame were taped with aluminium tape to increase airtightness (see Figure 11 right).

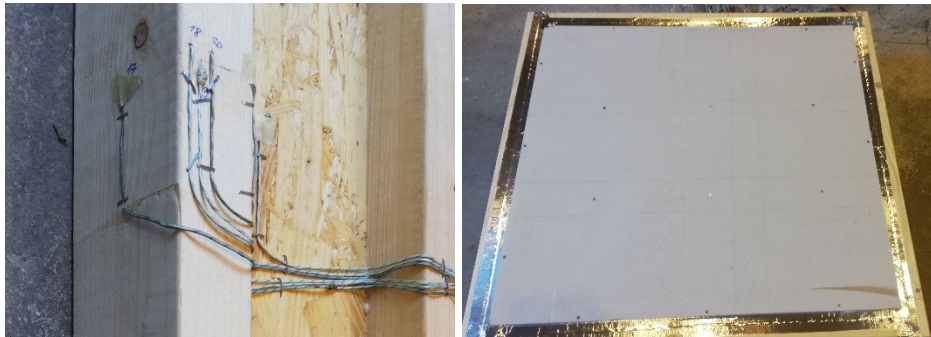


Figure 11. Thermocouples on the fire exposed flange (left) and the finished specimen (right).

Temperatures were monitored throughout the test duration. If all drilled-in thermocouples or ones on the web showed temperatures over 300 °C the burners were turned off and the test time stopped. The tests were stopped at different stages, in some cases if all drilled-in thermocouples showed temperatures over 300 °C, whereas other tests were stopped earlier to keep more charred cross-section for further investigation.

The thermocouple wires were cut and the specimen was lifted from the furnace. The specimen was extinguished using water. The time elapsed from turning off the burners to complete extinguishment was less than 2 minutes. Any remaining insulation was removed from the specimen immediately after extinguishment.

The residual charred areas from furnace fire tests were measured. First, the loose char layer was removed by wire brush. Then, slices of the specimen were cut (approximately 5 cm thick). Both sides of these slices were traced to paper and the cross-sections were scanned. Finally, the residual areas were redrawn in AutoCAD and the REGION and MASSPROP commands were used to obtain the charred cross-section areas.

3.1.2 Results

The temperature measurements and other results obtained from model-scale furnace fire tests are shown below.

The tested start times of charring, fall-off times of gypsum boards and test durations for unloaded model-scale tests are shown in Table 5.

Table 5. Tested start times of charring, fall-off times of gypsum boards and test durations.

Test number	Fall-off time	Beam B1				Beam B2				Test duration
	t_f	t_{ch}	$t_{ch,2}$	$t_{ch,w}$	A_{res}	t_{ch}	$t_{ch,2}$	$t_{ch,w}$	A_{res}	t_{test}
T1	25.8	25.8	36.0	-	2806	25.8	33.9	-	572	46
T2	53.2	29.0	47.3	-	1586	29.3	52.4	69.6	0	70
T3	38.0	31.8	39.1	50.7	99	31.6	38.3	-	934	51.8
T4	33.7	29.8	36.3	54.4	0	30.9	35.7	-	472	55.4
T5	35.2	32.8	40.6	61.5	103	30.7	38.9	-	0	63.4
T6	34.1	29.7	37.1	69.1	0	27.4	39.8	-	0	69.3

Temperatures measured in T5 are presented in Figure 12 and in T1 are in Figure 13. Test T5 had I-joists with sawn wood flanges with different widths and stone wool cavity insulation. Test T1 had I-joists with sawn wood flanges with different widths and glass wool cavity insulation.

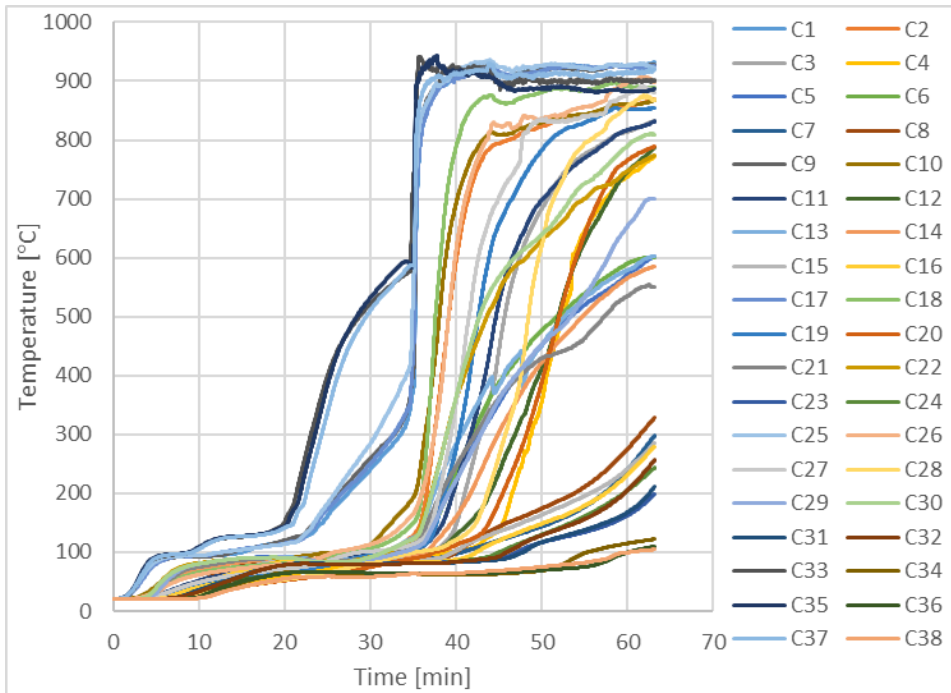


Figure 12. All temperatures measured in MST T5.

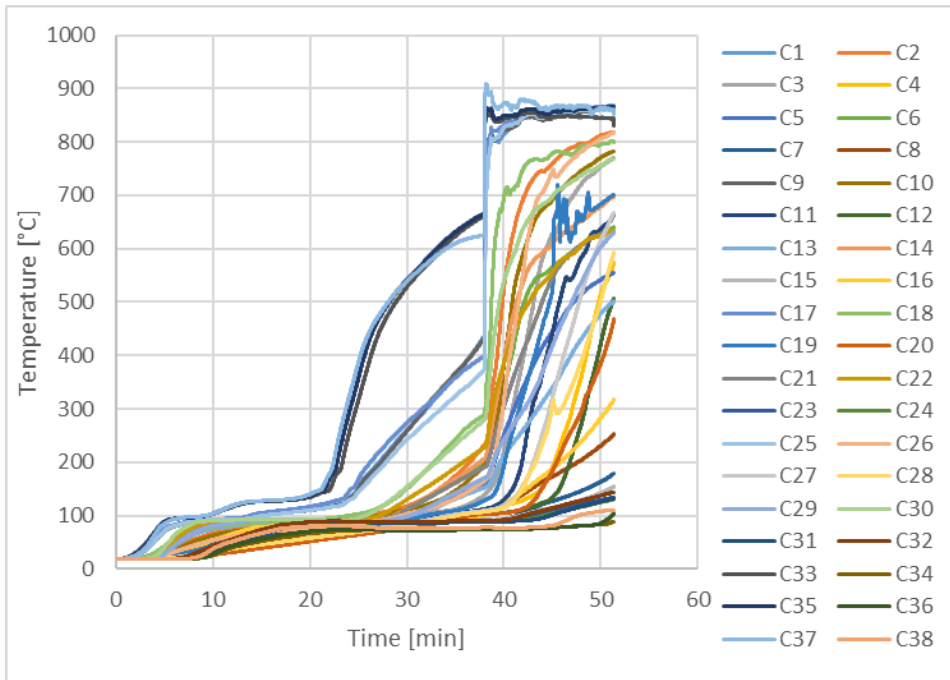


Figure 13. All temperatures measured in MST T1.

The temperature development at the different measurement stations on the same cross-section show very good agreement. Temperature rise in the flange is significantly slower in the wider cross-section. See Figure 10 for the schematic of the TC locations.

3.2 Thermal FE simulations

The objective of thermal FE simulations is to investigate the temperature development in the fire exposed flange and the web of I-joists exposed to the ISO 834 standard fire curve (ISO, 1999). Furthermore, the simulation data was used to determine the times that separate the charring phases and the modification factors for charring rate. The latter are the basis for the charring calculations according to the European Charring model as described in FprEN 1995-1-2:2025 (CEN, 2025b). The FE simulations were validated with model-scale furnace fire test data.

3.2.1 Methodology

Finite element simulations for this study were conducted using SAFIR software v2022.a.2 (Franssen & Gernay, 2017). This software package allows for the investigation of heat conduction in materials and voids, as well as the mechanical response of the structural elements by solving the Fourier heat transfer equation.

ISO 834 (ISO, 1999) standard fire exposure was used on the fire exposed side and an ambient temperature of 20 °C boundary was imposed on the unexposed surface.

The coefficient of convection was taken as 25 W/(m²K) on heated surfaces and 4 W/(m²K) on unheated surfaces according to EN 1991-1-2:2002 (CEN, 2002), and emissivity as 0.8 according to EN 1995-1-2:2004 (CEN, 2004c). These coefficients were

used only on the exposed and unexposed surfaces of the assembly. Void cavities have not been studied within the scope of the thesis.

To calculate the heat transfer, the values of thermal conductivity, specific heat capacity and density are needed at different temperatures. These properties change with temperature as a reflection of various chemical or physical reactions happening in the material under different temperatures and heating conditions. The thermal properties used in this thesis were taken from widely accepted sources and are given in Table 6 for timber, Table 7 for wood fibreboard and OSB, Table 8 for stone wool, Table 9 for glass wool and Table 10 for gypsum plasterboard.

Table 6. Thermal properties of timber used in FE simulations according to FprEN 1995-1-2:2025 (CEN, 2025b).

Temperature [°C]	Thermal conductivity [W/(m·K)]	Specific heat [J/(kg·K)]	Density ratio ρ_i/ρ_{20}
20	0.12	1530	1
99	0.133	1770	1
100	0.133	13600	1
120	0.167	13500	1
121	0.137	2120	0.89
200	0.15	2000	0.89
250	0.123	1620	0.83
300	0.097	710	0.68
350	0.07	850	0.46
400	0.077	1000	0.34
500	0.09	1200	0.30
600	0.177	1400	0.25
800	0.35	1650	0.23
1200	1.5	1650	0

Table 7. Thermal properties of wood fibreboard and OSB used in FE simulations (Östman et al., 2010).

Temperature [°C]	Thermal conductivity [W/(m·K)]	Specific heat [J/(kg·K)]	Density ratio ρ_i/ρ_{20}
20	0.12	1790	1
100	0.3	1790	1
110	0.23	30796	0.97
120	0.15	1790	0.94
200	0.18	1790	0.94
275	0.14	6173	0.58
350	0.09	690	0.23
500	0.23	690	0.21
800	0.74	690	0.17
1200	4.2	690	0.11

The thermal conductivity of stone wool depends on its density according to equation (13).

$$\lambda(\rho) = \begin{cases} \lambda(\rho_0) & \text{for } T \leq 100 \text{ }^\circ\text{C} \\ \lambda(\rho_0) \cdot (11 \cdot e^{-0.05 \cdot \rho_{20}} + 1.9) & \text{for } T > 100 \text{ }^\circ\text{C} \end{cases} \quad (13)$$

where

- $\lambda(\rho)$ is the density-dependent thermal conductivity [W/(m·K)];
- $\lambda(\rho_0)$ is the density coefficient for thermal conductivity [W/(m·K)];
- ρ_{20} is the density at ambient temperature [kg/m³].

In the scope of this thesis, the density of stone wool at ambient temperature has been taken as 26 kg/m³.

Table 8. Thermal properties of stone wool used in FE simulations (Östman et al., 2010).

Temperature [°C]	Thermal conductivity [W/(m·K)]	Specific heat [J/(kg·K)]	Density ratio ρ_i/ρ_{20}
20	0.036	880	1
100	0.047	1040	1
200	0.304	1160	0.98
400	0.449	1280	0.977
600	0.751	1355	0.973
800	1.154	1430	0.97
925	1.517	1477	0.96
1200	2.418	1580	0.887

The ambient temperature density of glass wool has been taken as 15 kg/m³.

Table 9. Thermal properties of glass wool used in FE simulations (Östman et al., 2010).

Temperature [°C]	Thermal conductivity [W/(m·K)]	Specific heat [J/(kg·K)]	Density ratio ρ_i/ρ_{20}
20	0.035	1200	1
100	0.068	1340	0.983
200	0.11	1380	0.961
300	0.151	1382	0.94
400	0.192	1384	0.94
510	0.238	1386	0.94
660	0.3	1389	0.94
1200	100	1400	0.94

Table 10. Thermal properties of gypsum plasterboard used in FE simulations (Östman et al., 2010).

Temperature [°C]	Thermal conductivity [W/(m·K)]	Specific heat [J/(kg·K)]	Density ratio ρ_{fi}/ρ_{20}
20	0.4	960	1
70	0.4	960	1
100	0.27	960	1
130	0.13	14900	0.93
140	0.13	25200	0.90
150	0.13	21700	0.88
170	0.13	960	0.83
600	0.13	960	0.83
720	0.33	4360	0.83
750	0.38	960	0.78
1000	0.8	960	0.78
1200	2.37	960	0.78

The values of thermal conductivity and density ratios of different materials are shown in Figure 14, and the specific heat values in Figure 15.

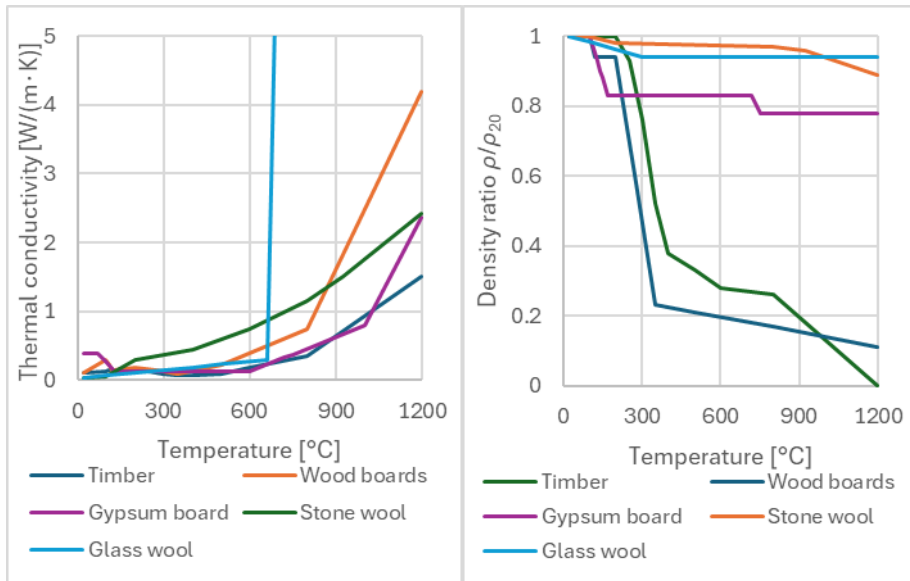


Figure 14. Thermal conductivities (left) and density ratios (right) used in FE simulations.

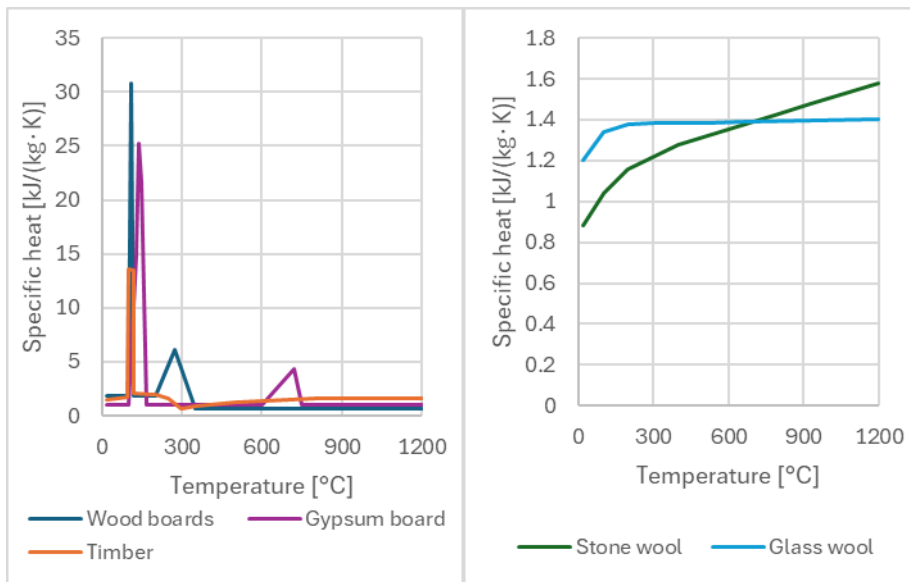


Figure 15. Specific heat of timber, wood-based boards and gypsum plasterboard (left) and stone and glass wool (right) used in FE simulations.

The thermal simulations were conducted in 2D using the SAFIR v2022.a.2 software. Quadrilateral 2D SOLID elements were used. Each element was defined by four nodes with one degree of freedom (temperature). SAFIR uses the sparse matrix solver PARDISO to solve the system of equations. Materials are described as solids, where the heat transfer is based on the Fourier equation. On surfaces, the heat exchange is based on linear convection and the law of grey bodies. Precision value 0.002 was used as the convergence criterion.

All simulated I-joists had a total depth of 200 mm as the main focus was on the investigation of the charring of the flange on the fire exposed side. The unexposed side was covered by a 20 mm thick wooden fibreboard. The cavities were completely filled with stone wool insulation with a density of 26 kg/m³ or glass wool with a density of 15 kg/m³.

The factors which were varied with each thermal simulation were the size of the flanges (both width and depth, according to Table 11), the length of the fire exposure (up to 120 minutes) and the thickness and fall-off time of the fire protection system (gypsum board, see Table 12).

The flange sizes were chosen based on available products on the market. The depth 69-mm and the width of 140-mm were added to extend the range of the investigated flange sizes. The fall-off times of 30, 45 and 60-minutes were chosen to represent common fire resistance time requirements. These times are also within the range of calculated fall-off times of gypsum plasterboards as given in FprEN 1995-1-2:2025 (CEN, 2025b).

All ten flange sizes were simulated without protection in the first set of simulations and then, all cases shown in Table 12 were simulated for each flange size. Fall-off of the fire protection system was imposed at various times by removing the material from the simulation and continuing the calculation until the full charring of the exposed flange. In total, 90 different configurations were simulated with both types of insulation.

The ambient temperature density of timber was taken as 490 kg/m³, wood-based boards (fibreboard or OSB) as 630 kg/m³ and gypsum plasterboard as 890 kg/m³.

The density values were based on the experimental results of the test campaign conducted by Tiso.

Table 11. Flange sizes.

Flange depths h_f (mm)	Flange widths b (mm)				
	38	46	70	96	140
36	V	V	V		
45		V	V	V	V
69		V	V	V	

Table 12. Fire protection systems.

Board thickness h_p (mm)	Fall-off times t_f (min)		
	30	45	60
13	V	V	
15	V	V	V
20	V	V	V

* V shows the performed simulation

The simulated sections were discretised into rectangular elements. The sizes of the elements were varied between $1 \times 1 \text{ mm}^2$ and $5 \times 5 \text{ mm}^2$. The time steps were kept at maximum 5 seconds. Half of a frame assembly (see Figure 16) with the stud distance of 600 mm centre-to-centre was simulated. The sides of the structure were adiabatic surfaces. Fire exposure is from below in Figure 16.

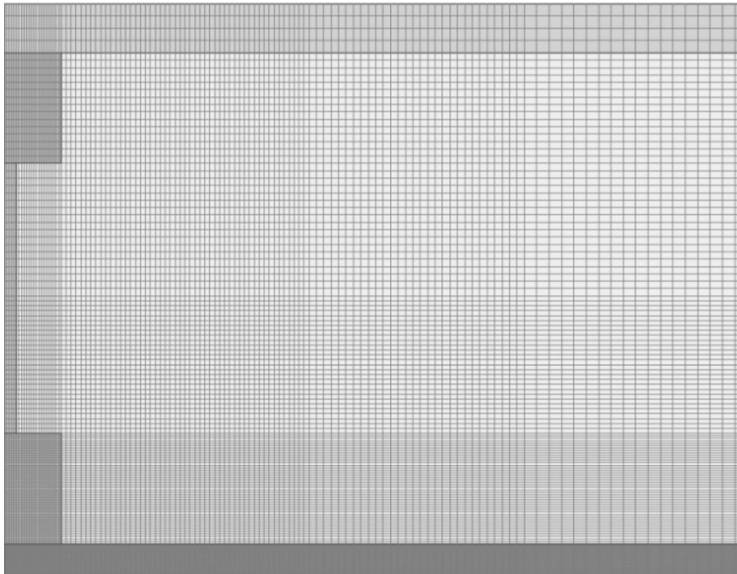


Figure 16. Element distribution in thermal simulations.

The configurations of model-scale furnace fire tests given in chapter 3.1.1 were simulated using similar element distribution. Material densities were taken the same as the tested materials. The failure time of gypsum plasterboard was imposed at the time it occurred in the tests.

3.2.1.1 Script 1

Script 1 was developed in MATLAB to extract the start time of charring (t_{ch}), the start time of lateral charring ($t_{ch,2}$), the start time of charring on the web ($t_{ch,w}$) and the height of the node on the web where charring first started ($h_{ch,w}$). These values were extracted for all simulated setups (Table 11 and Table 12). These parameters are a significant input for the development of the charring calculation model.

The script would import the SAFIR thermal output files and retain the node information of the wood flanges and the web. All timesteps and temperatures with and without gypsum were stored. The locations of all nodes which make up the I-joist were also stored. Figure 17 shows the stored elements of the fire exposed flange and part of the web as the grid. The nodes which include temperature data are at each intersection. The dashed line represents symmetry.

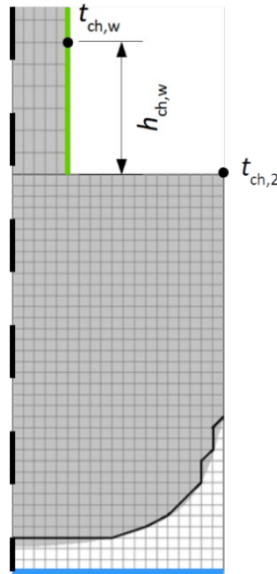


Figure 17. Fire exposed flange.

The start time of charring is relevant for the design model as the first time when the calculation of the char depth on the fire exposed side should be considered. The start time of charring was determined as the first time when a node on the blue line in Figure 17 had a temperature greater than 300 °C.

The start time of lateral charring is relevant for the design model as the first time when the calculation of the char depth on the lateral side should be considered. The start time of lateral charring was determined as the first time when the node at the top corner of the flange (see point marked with “ $t_{ch,2}$ ” in Figure 17) showed a temperature greater than 300 °C.

The start time of charring on the web is relevant for the design model as the first time when the calculation of the char depth on the web should be considered. The start time of charring on the web was determined as the first time when a node on the green line in Figure 17 had a temperature greater than 300 °C. The distance of this node from the top of the flange was recorded as $h_{ch,w}$. That distance is an important parameter for the development of the design model, showing the location where web starts to char and its cross-section starts to decrease.

3.2.1.2 Script 2

Script 1 was developed in MATLAB to calculate the charred flange area A_{fi} for each timestep. The charred areas were calculated for all simulated setups (Table 11 and Table 12). The areas are used for the development of the charring calculation model.

The charred flange area A_{fi} was calculated for each timestep based on the area enclosed within nodes with temperatures lower than 300 °C. The black line Figure 17 in represents the boundary of the charred flange area. The flange was divided into horizontal trapezoidal slices and summarised.

3.2.2 Results and analysis

The start times of charring for all simulation cases with stone wool cavity insulation are shown in Table 13.

Table 13. The start times of charring in minutes from thermal FE simulations with stone wool cavity insulation.

Flange size $b \times h_f$ (mm)	Thickness of gypsum (mm) ; Failure time (min)								
	0;0	13;30	13;45	15;30	15;45	15;60	20;30	20;45	20;60
38x36	2	25.8	25.8	30.1	30.7	30.7	30.1	43.4	43.4
46x36	2	26.0	26.0	30.1	30.8	30.8	30.1	43.7	43.7
46x45	2	26.1	26.1	30.1	30.8	30.8	30.1	43.8	43.8
46x69	2	26.1	26.1	30.1	30.8	30.8	30.1	43.8	43.8
70x36	2	26.3	26.3	30.1	31.3	31.3	30.1	44.2	44.2
70x45	2	26.3	26.3	30.1	31.3	31.3	30.1	44.2	44.2
70x69	2	26.3	26.3	30.1	31.3	31.3	30.1	44.2	44.2
96x45	2	26.5	26.5	30.1	31.4	31.4	30.1	44.4	44.4
96x69	2	26.5	26.5	30.1	31.4	31.4	30.1	44.5	44.5
140x45	2	26.7	26.7	30.1	31.6	31.6	30.1	44.7	44.7

The start times of charring on the lateral side for all simulation cases with stone wool cavity insulation are shown in Table 14.

Table 14. The start times of lateral charring in minutes from thermal FE simulations with stone wool cavity insulation.

Flange size $b \times h_f$ (mm)	Thickness of gypsum (mm) ; Failure time (min)								
	0;0	13;30	13;45	15;30	15;45	15;60	20;30	20;45	20;60
38x36	11.3	31.3	36.0	32.3	41.0	41.0	32.9	46.3	54.4
46x36	11.1	31.2	35.6	32.3	40.6	40.6	32.9	46.3	53.9
46x45	13.8	32.5	38.6	33.7	43.6	43.6	34.3	47.3	57.1
46x69	22.0	37.8	45.8	38.9	47.6	51.4	39.7	51.6	61.8
70x36	10.8	31.2	35.2	32.2	40.1	40.1	32.8	46.3	53.4
70x45	13.4	32.4	38.0	33.6	43.0	43.0	34.3	47.3	56.4
70x69	21.3	37.4	45.5	38.6	47.3	50.8	39.3	51.3	61.6
96x45	13.3	32.4	37.8	33.6	42.8	42.8	34.2	47.3	56.2
96x69	21.2	37.3	45.4	38.6	47.3	50.6	39.2	51.3	61.6
140x45	13.3	32.3	37.8	33.6	42.8	42.8	34.2	47.3	56.1

The start times of charring on the web for all simulation cases with stone wool cavity insulation are shown in Table 15.

Table 15. The start times of charring in minutes on the web from thermal FE simulations with stone wool cavity insulation.

Flange size $b_f \times h_f$ (mm)	Thickness of gypsum (mm) ; Failure time (min)								
	0;0	13;30	13;45	15;30	15;45	15;60	20;30	20;45	20;60
38x36	22.2	39.6	45.9	40.9	48.7	51.3	41.7	53.6	62.3
46x36	24.5	41.3	47.4	42.7	50.3	53.6	43.4	55.2	63.7
46x45	28.1	44.2	49.9	45.5	52.8	56.9	46.2	57.7	66.0
46x69	38.1	52.7	57.8	53.8	60.7	65.0	54.5	65.3	73.2
70x36	30.7	46.3	52.1	47.6	54.9	59.8	48.2	59.5	67.8
70x45	35.3	50.2	55.6	51.4	58.4	63.1	52.1	63.0	71.0
70x69	49.5	62.6	67.3	63.7	69.9	73.9	64.3	74.3	81.6
96x45	42.4	56.3	61.6	57.5	64.2	68.7	58.2	68.6	76.3
96x69	62.3	74.2	78.6	75.3	81.0	84.8	75.8	85.0	91.9
140x45	51.8	64.9	70.2	65.9	72.4	77.1	66.5	76.3	84.0

The heights of the first node to char on the web for all simulation cases with stone wool cavity insulation are shown in Table 16.

Table 16. The heights of the first node to char on the web in millimetres from thermal FE simulations with stone wool cavity insulation.

Flange size $b_f \times h_f$ (mm)	Thickness of gypsum (mm) ; Failure time (min)								
	0;0	13;30	13;45	15;30	15;45	15;60	20;30	20;45	20;60
38x36	8	10	10	10	10	10	10	10	10
46x36	10	12	12	12	14	12	12	12	12
46x45	14	12	14	14	12	12	14	12	14
46x69	12	14	12	14	14	12	12	14	14
70x36	18	20	20	20	20	20	18	18	18
70x45	22	20	20	22	22	20	20	20	20
70x69	18	20	18	18	18	18	20	18	20
96x45	24	26	26	26	24	26	26	26	26
96x69	20	20	20	22	20	20	22	20	22
140x45	0	22	24	20	20	24	20	20	24

Additionally, the charred areas for every simulation were calculated and divided by the initial flange area for easier comparison. The following four graphs present the reduction in charred flange areas over time for flanges insulated with stone and glass wool. A comparison can be made between the effect of short and long fall-off times. 13-mm thick gypsum plasterboard with a fall-off of 30 and 45 minutes is shown for stone wool in Figure 18 and Figure 19, and for glass wool in Figure 20 and Figure 21.

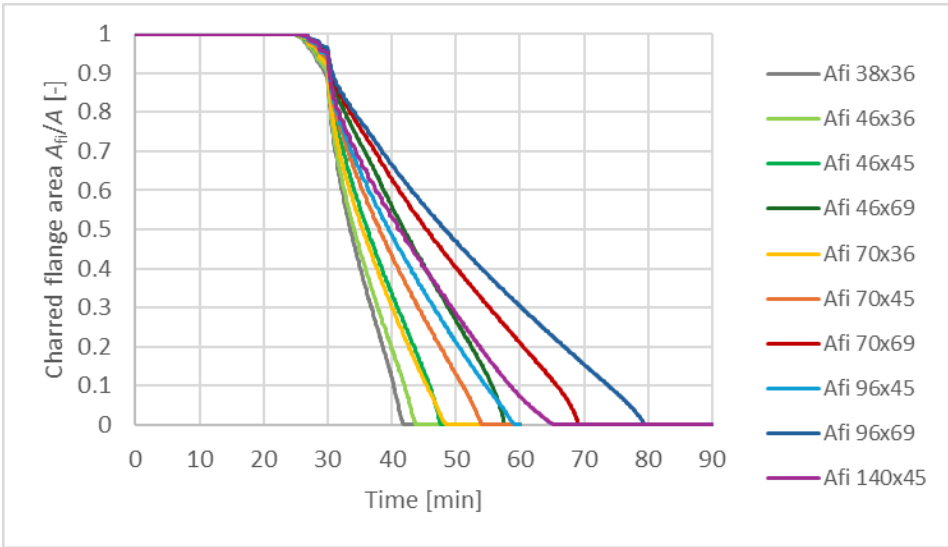


Figure 18. Charred areas of 13-mm thick gypsum with 30-min fall-off time with stone wool.

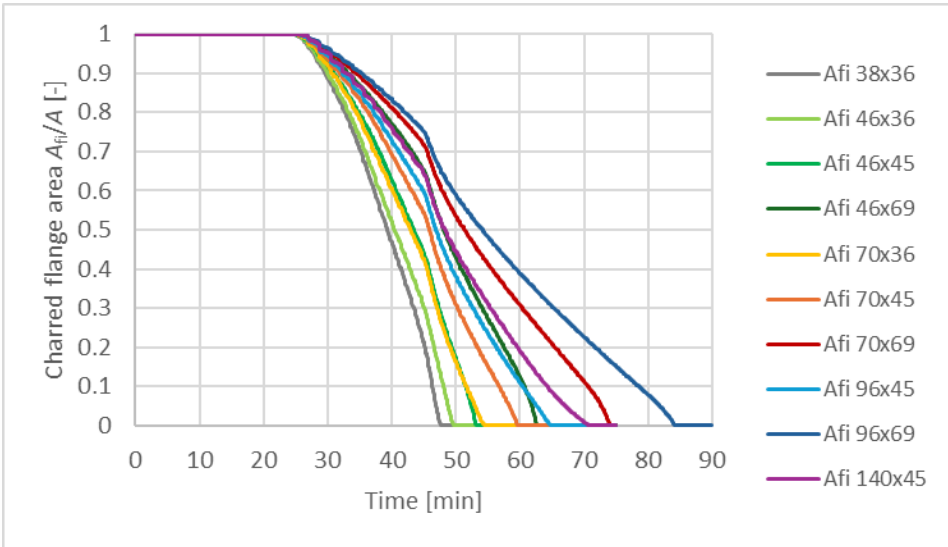


Figure 19. Charred areas of 13-mm thick gypsum with 45-min fall-off time with stone wool.

The reduction in area starts at the start time of charring and is slower behind protection. After the fall-off of gypsum board, the charring rate increases. For the case with short fall-off time, the charring rate is briefly very rapid before slowing down. Comparing the graphs, the reduction of area has a similar slope after fall-off and the initial rapid phase.

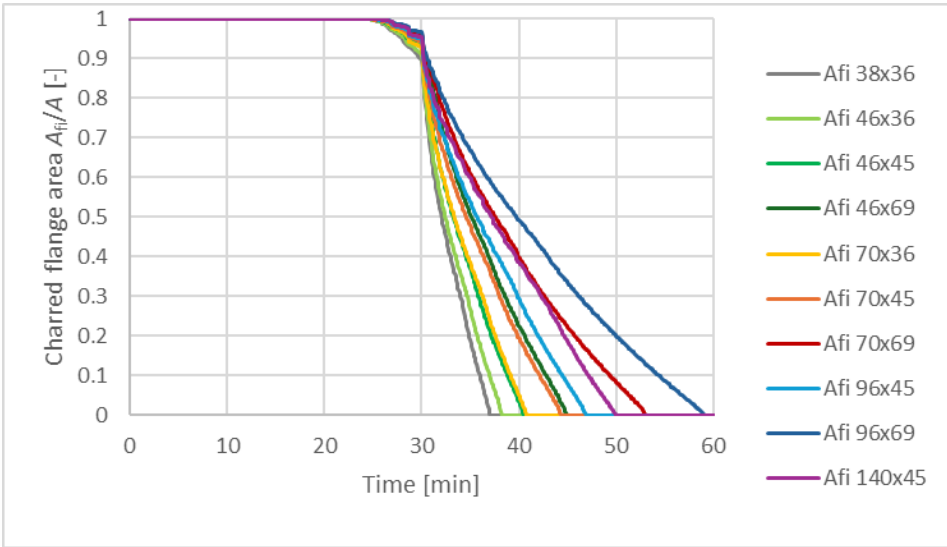


Figure 20. Charred areas of 13-mm thick gypsum with 30-min fall-off time with glass wool.

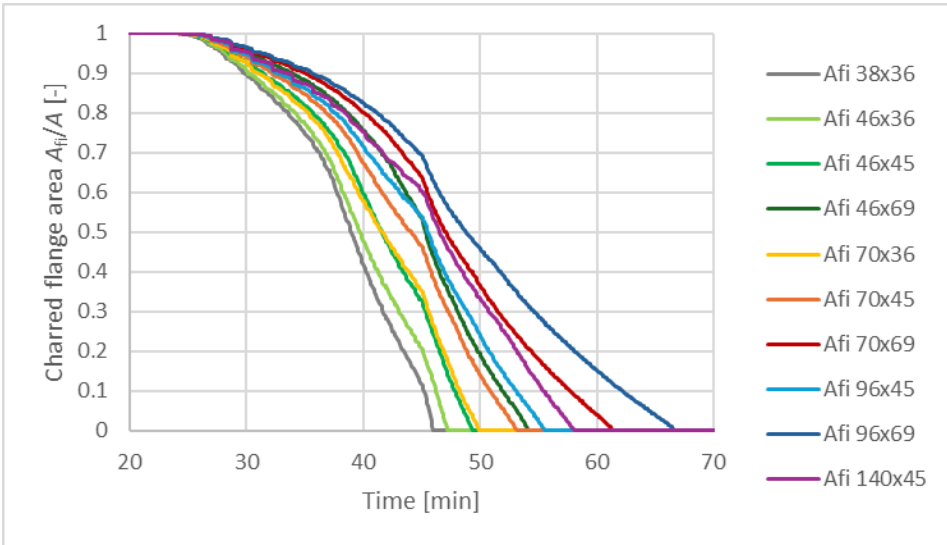


Figure 21. Charred areas of 13-mm thick gypsum with 45-min fall-off time with glass wool.

Comparing the reduction in area between assemblies with stone and glass wool, the reduction is greater with glass wool insulation. The overall tendencies, however, are very similar. The slopes of the curves are almost colinear when the protection is in place and before the start of lateral charring.

3.2.3 Comparison with calculations and model-scale tests

This section provides the results of numerical analyses where the temperature distribution in the cross-section was investigated. The thermal simulations were conducted on different flange dimensions, with different protection and two types of thermal insulation as described previously in Chapter 3.2.1.

The start times of charring on the fire exposed side from simulations and calculations according to FprEN 1995-1-2:2025 are shown in Figure 22. The start times of charring are shown for each combination of the thickness (h_p) and the failure time (t_f) of the thermal simulations according to Table 12.

The start time of charring was calculated according to equation (14):

$$t_{ch} = 2.8 \cdot h_p - 14 \quad (14)$$

where

t_{ch} is the start time of charring [min];

h_p is the thickness of the gypsum board [mm].

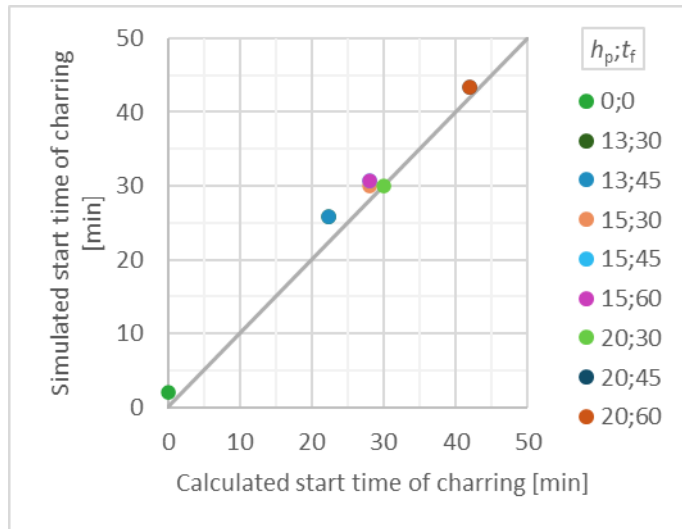


Figure 22. Start time of charring.

The simulations give slightly longer times than the calculations using the Separating Function Method. The calculation results are very similar to the simulations. The reason could be that the simulation results for the start of charring were taken as the first time when a node in the timber flange reached 300 °C. This point was always in the outer corner of the flange. In the calculations this distinction cannot be made and the calculated start time of charring is at the middle of the width of the timber flange.

The start time of charring on the fire exposed side is unaffected by the type of insulation used in the simulations, which also corresponds to the assumptions used in the calculations.

The start time of charring was calculated as the sum of the protection time of the gypsum plasterboard ($t_{prot,1}$) and the protection time of the thermal insulation ($t_{prot,2}$) with the thickness taken as the depth of the flange (h_1 in Figure 23). The start time of lateral charring from simulations and calculations according to FprEN 1995-1-2:2025 using stone wool cavity insulation is shown in Figure 24.

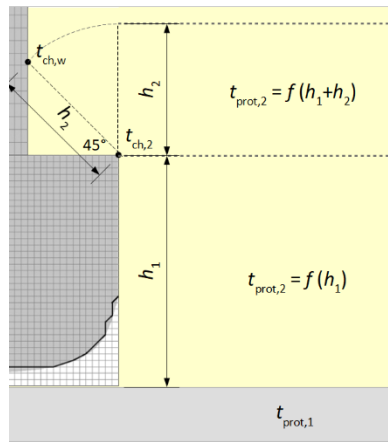


Figure 23. Thicknesses of insulation to calculate the start time of lateral charring and the start time of charring on the web.

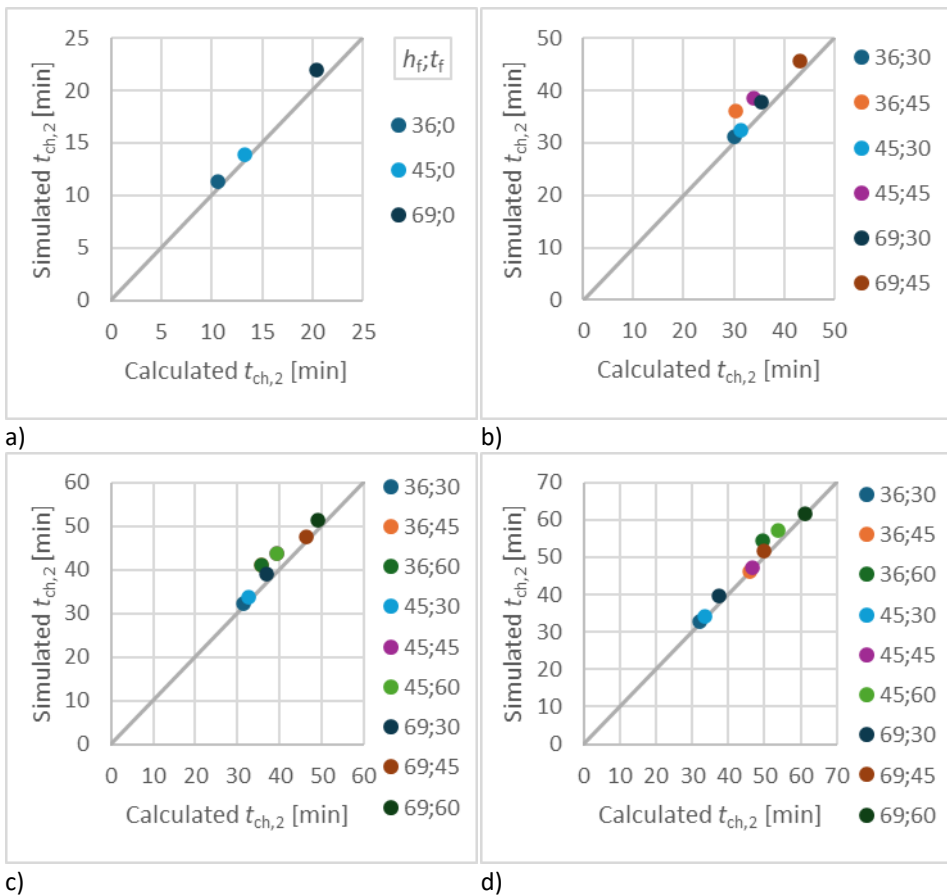


Figure 24. Start time of lateral charring with stone wool: a) unprotected, b) 13-mm gypsum, c) 15-mm gypsum, d) 20-mm gypsum. Legend key: flange depth (mm)/fall-off time (min).

The start times of lateral charring with stone wool insulation are slightly longer in the simulations than the calculated values. The calculations used the Separating Function Method. The method is slightly conservative in the calculation of the start time of lateral charring compared to the thermal simulation results.

The comparison of the start time of lateral charring from simulations and calculations using glass wool cavity insulation is shown in Figure 25. The start time of charring was calculated using the SFM, similarly to stone wool.

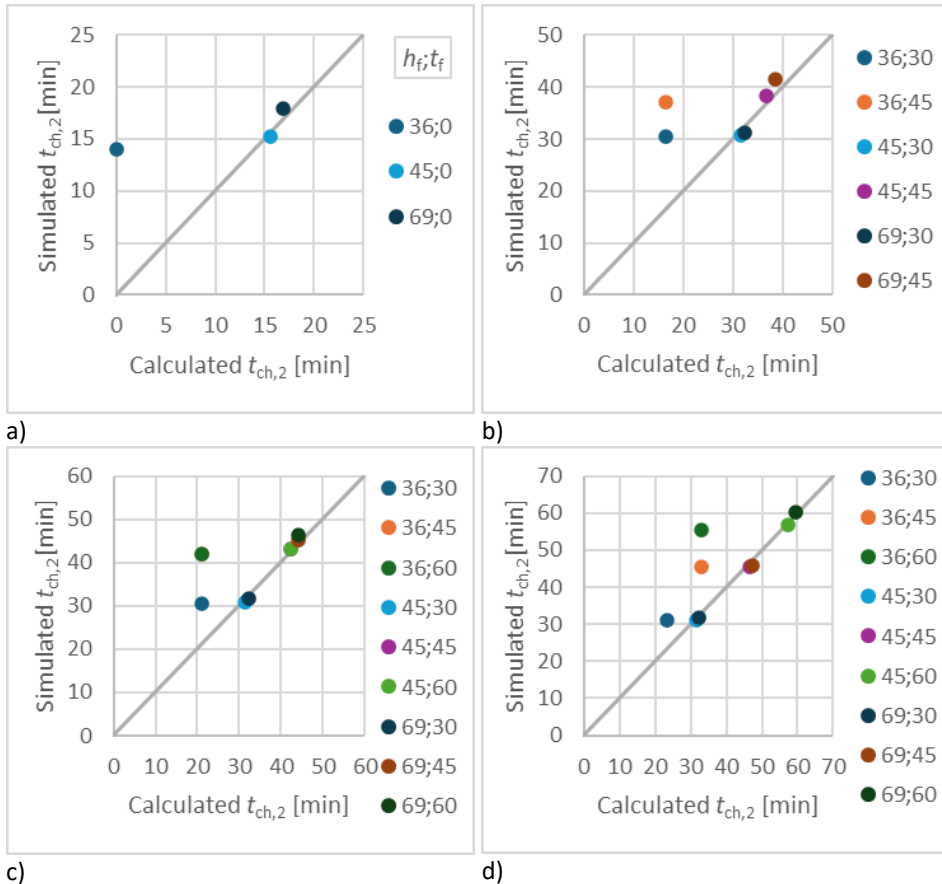


Figure 25. Start time of lateral charring with glass wool: a) unprotected, b) 13-mm gypsum, c) 15-mm gypsum, d) 20-mm gypsum. Legend key: flange depth (mm)/fall-off time (min).

With glass wool as the cavity insulation, a noticeable scatter of the comparison of the simulations and calculations can be seen. This is due to the calculation rules, which state that for glass wool thicknesses of less than 40 mm, the protection time must be taken as 0. The same assumption is not included in the simulations, therefore the flange depth of 36 mm shows a larger difference. Other simulated flange depths are captured very precisely by the calculations.

The distances between the first node to char on the side of the web and the top of the fire exposed flange from simulations with stone and glass wool are shown in Figure 26. The diagonal dashed line shows the assumption that charring starts at the point marked with “ $t_{ch,w}$ ” in Figure 23 and the height of this point from the top of the flange $h_{ch,w}$ is

calculated according to (15). The distance is necessary to calculate the start time of charring on the web using the SFM.

$$h_{ch,w} = \frac{b_f - b_w}{2} \tag{ 15 }$$

where

b_f is the initial width of the flange [mm];

b_w is the thickness of the web [mm].

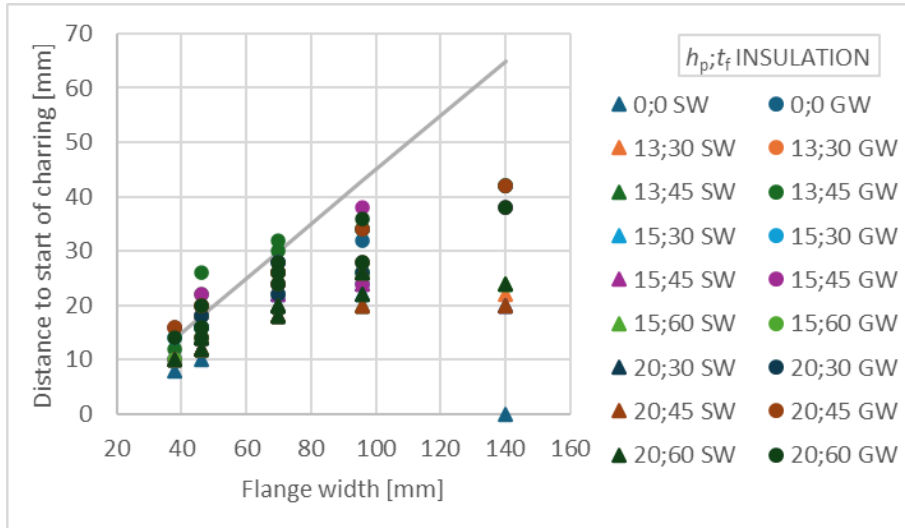


Figure 26. Height of the first node to exceed 300 °C on the side of the web.

The comparison of the start time of charring on the web from simulations and calculations using stone wool cavity insulation is shown in Figure 27. The start time of charring on the web was calculated as the sum of the protection time of the gypsum board ($t_{prot,1}$) and the protection time of the cavity insulation ($t_{prot,2}$) with the thickness taken as the sum of h_1 and h_2 (see Figure 23).

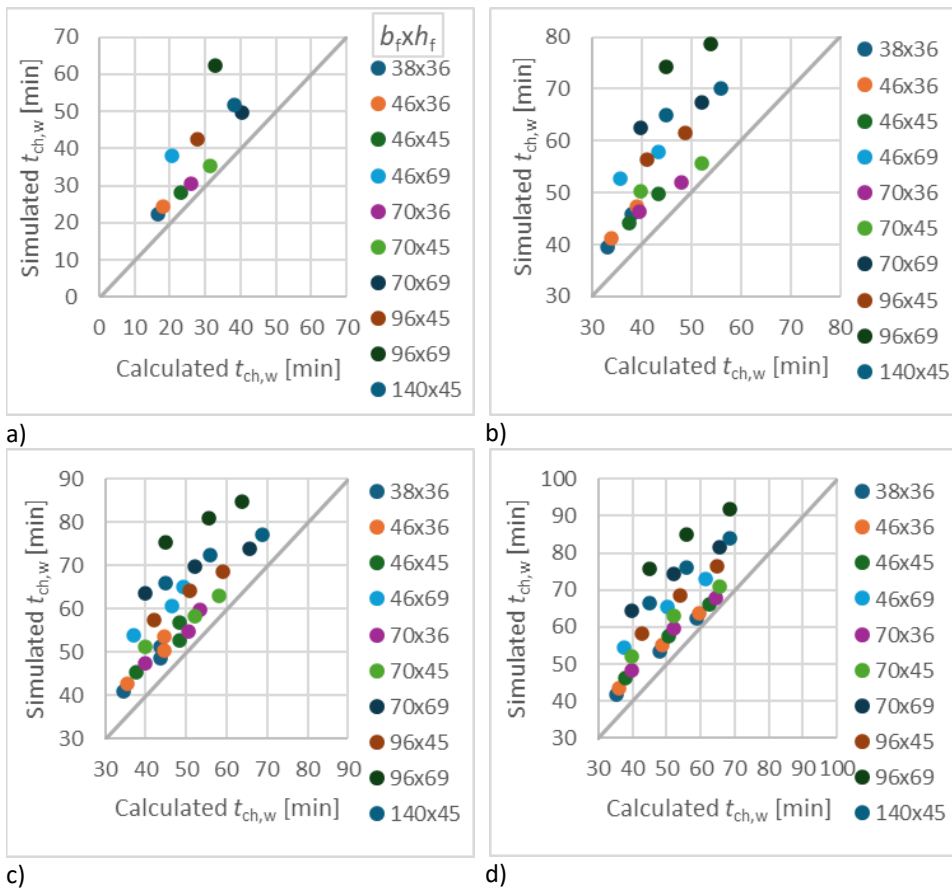


Figure 27. Start time of charring on the web with stone wool: a) unprotected, b) 13-mm gypsum, c) 15-mm gypsum, d) 20-mm gypsum. Legend key: flange width (mm) x flange depth (mm).

The calculations show an earlier start time of charring on the web in all simulation cases with stone wool cavity insulation. Interestingly, larger cross-sections show a more conservative result, even though the distance for the point where the start of charring occurs is overestimated for wider flanges (see equation (15) and Figure 26). The conservative calculation for the start of charring on the web is essential for I-joists, as the load-bearing capacity may be almost immediately lost when the web chars.

The comparison of the start time of charring on the web from simulations and calculations using glass wool cavity insulation is shown in Figure 28. The start time of charring was calculated similarly as described above for cavities with stone wool.

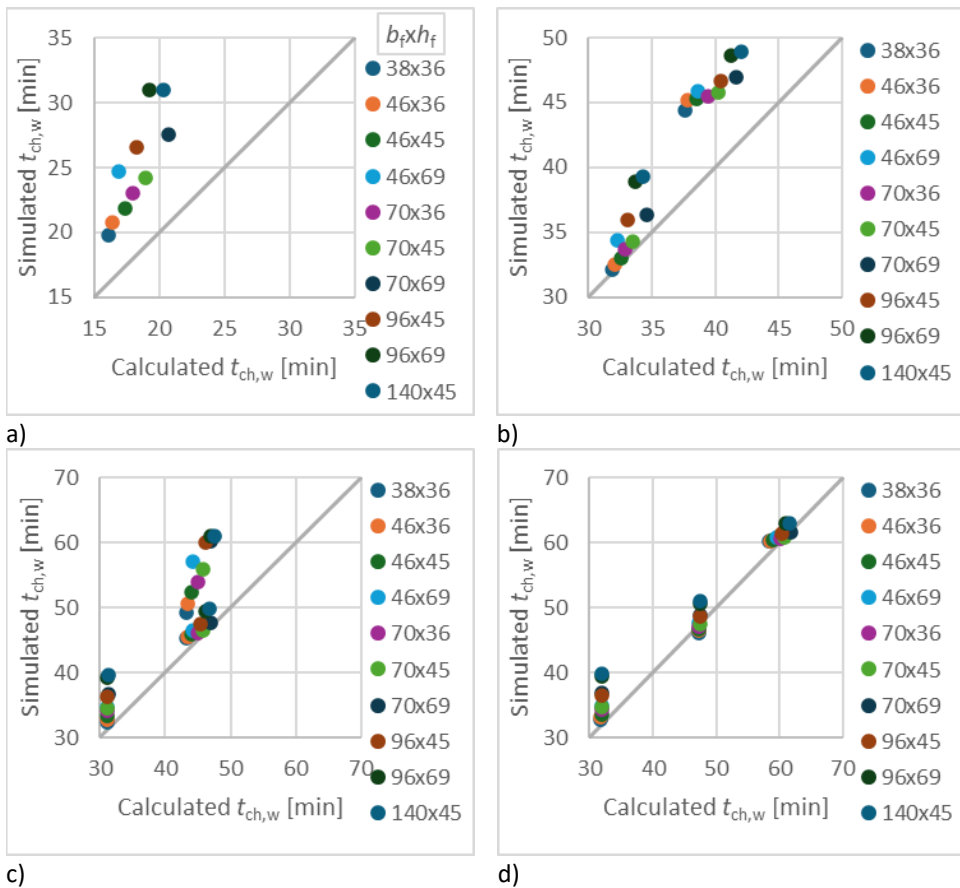


Figure 28. Start time of charring on the web with glass wool: a) unprotected, b) 13-mm gypsum, c) 15-mm gypsum, d) 20-mm gypsum. Legend key: flange width (mm) x flange depth (mm).

The start times of charring on the web for simulations with glass wool cavity insulation are slightly less conservative compared to the results of simulations with stone wool. Nevertheless, no significantly unsafe calculations were identified.

Based on Figure 27 and Figure 28 it is a reasonable simplification to calculate the start of charring on the web as the sum of protection times at the depth of the flange plus the distance from the corner to the web at a 45° angle. Although this is not precisely the same location where some simulations showed the first node to start charring, this distance fits reasonably for the calculation of the start of charring on the web. The conservative calculation for the start of charring on the web is essential for I-joists, as the load-bearing capacity may be almost immediately lost when the web chars. The corner of the flange provides some thermal “shielding” effects and based on the comparison with the simulations, the calculations are able to consider this effect reasonably well.

The char depths obtained from tests T5 (stone wool) and T1 (glass wool) are compared with simulations run with the same configuration are shown in Figure 29. The same colour represents the same beam.

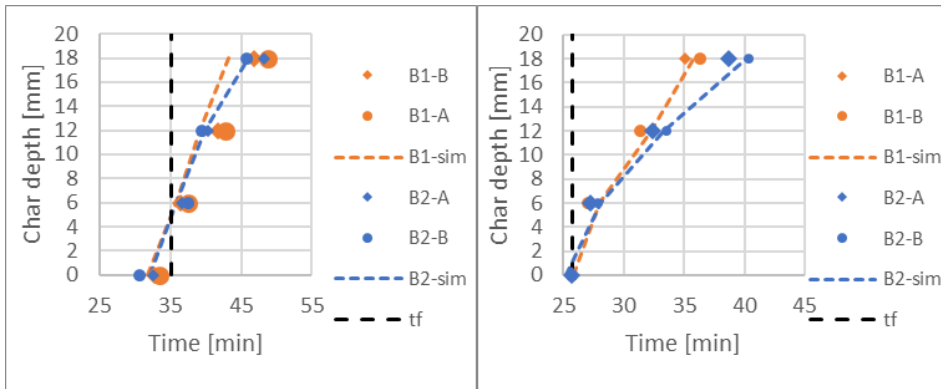


Figure 29. Comparison of tested and simulated char depths in tests T5 (left) and T1 (right.)

The comparison of tested and simulated start times of charring on the exposed and lateral sides, the web, and the residual charred areas is shown in Table 17. The development of the char depth in the middle of the flange is captured well in the simulations for both cases with stone and glass wool cavity insulation. As the measurements are taken at distinct points, the continuous char development behaviour must be interpolated between the different distances. Therefore, some minor effects may be undetectable in the experimental setup. Nonetheless, the overall agreement with the simulation results is considered satisfactory.

Table 17. Comparison of tested and simulated start times of charring on the exposed and lateral sides, the web, and the residual charred areas.

Beam no	Start time of charring [min]		Start time of lateral charring [min]		Start time of charring on the web [min]		Residual flange area [mm ²]	
	Test	Sim	Test	Sim	Test	Sim	Test	Sim
T1_B1	25.8	25.8	36.0	27.2	>46	33.6	2806	0
T1_B2	25.8	25.8	33.9	27.1	>46	30.2	572	0
T2_B1	29.0	32.0	47.3	43.3	>70	67.8	1586	245
T2_B2	29.3	31.8	52.4	44.1	69.6	56.3	0	0
T3_B1	31.8	31.8	39.1	38.2	50.7	39.4	99	0
T3_B2	31.6	32.0	38.3	38.2	>51.8	41.7	934	0
T4_B1	29.8	31.8	36.3	34.9	54.4	44.5	0	0
T4_B2	30.9	32.0	35.7	35.2	>55.4	>55.4	472	200
T5_B1	32.8	31.8	40.6	37.2	61.5	48.3	103	0
T5_B2	30.7	32.0	38.9	37.1	>63.4	60.3	0	80
T6_B1	29.7	32.0	37.1	35.4	69.1	54.3	0	0
T6_B2	27.4	32.0	39.8	36.3	>69.3	59.7	0	0

3.3 Development of charring equations

The modification factors for the charring rate (also called the charring equations) are developed based on the charred areas obtained from thermal FE simulations. The equations are valid for flange widths greater than 38 mm and flange depths greater than 36 mm. The post-protection coefficient is valid for failure times up to 90 minutes.

3.3.1 Methodology (Script 3)

The development of the modification factors for charring (also called charring coefficients) utilised Script 3. The updated expressions for charring coefficients were developed based on charred areas from all thermal simulations using an iterative optimisation script starting with equations from Publication V.

The optimisation utilised the FMINSEARCH function of MATLAB. The function uses an iterative process and aims to find parameter values that minimise the objective function. The objective function would calculate the mean square error (MSE) between the calculated and simulated charred areas.

Mean square error (MSE) is calculated according to equation (16):

$$MSE = \frac{1}{p} \sum_{m=1}^p (Y_m - \widehat{Y}_m)^2 \quad (16)$$

where

- MSE is the mean square error;
- p is the number of data points;
- Y_m are the observed values;
- \widehat{Y}_m are the predicted values.

The unit of the MSE is the square of the unit of the value. The benefit of using MSE as the objective function is that it significantly penalises large deviations. For the purposes of this thesis, the reduction of large deviations is beneficial in order to more accurately capture the simulations with the equations.

The charring model described in chapter 5.1 was implemented to calculate the char depths on the exposed and lateral sides of the flange for each time step and the charred areas. Then, the calculated area was compared to the simulated area at each time step and the MSE was found for every simulation case.

Then, MATLAB would iteratively change the input parameters (charring coefficients) and converge towards a combination of inputs which yields the minimum MSE value based on the algorithm of FMINSEARCH function.

3.3.2 Results and analysis

The charring equations were developed using the FMINSEARCH function of MATLAB. The function uses an iterative process and aims to find parameter values that minimise the objective function. The objective function would calculate the mean square error between the calculated and simulated charred areas.

The optimisation script showed relatively similar values for assemblies insulated with stone or glass wool for the combined section and conversion coefficient. This shows that the equations appropriately decouple different effects. Since the combined section and conversion coefficient should only consider the effect of the cross-section dimensions on the charring rate, it should not be dependent on the type of cavity insulation.

The combined section and conversion coefficient for the exposed side is calculated as shown in equation (17):

$$k_{s,n,1} = 7.6 \cdot b_f^{-0.35} \quad (17)$$

where

$k_{s,n,1}$ is the combined section and conversion factor for the exposed side [-];
 b_f is the initial flange width [mm].

The combined section and conversion coefficient for the lateral side is calculated as (18):

$$k_{s,n,2} = 220 \cdot h_f^{-1.2} \quad (18)$$

where

$k_{s,n,2}$ is the combined section and conversion factor for the lateral side [-];
 h_f is the initial flange depth [mm].

The consolidation time was also independent of the cavity insulation and was set as (19):

$$t_a = 1.05 \cdot t_f \quad (19)$$

where

t_a is the consolidation time [min];
 t_f is the failure time of the fire protection system [min].

The previous expressions were fixed, and the optimisation script was run for a second time to develop the post-protection and consolidation coefficients.

The post-protection coefficient describes the increased charring rate which occurs after the fall-off of the protection system. On the fire exposed side, the charring rate slows down after the consolidation time. As the consolidation time is longer for longer fall-off times, but the charring rate is more rapid in the case of shorter fall-off times, the post-protection coefficient for the exposed side depends on the fall-off time linearly with a negative slope (20):

$$k_{3,1} = 9 - 0,093 \cdot t_f \quad \text{with PL1 (stone wool) insulation} \quad (20)$$

$$k_{3,1} = 5.5 - 0,015 \cdot t_f \quad \text{with PL2 (glass wool) insulation}$$

where

$k_{3,1}$ is the post-protection coefficient for the exposed side [-].

The post-protection coefficient for the lateral sides is used until the end of the fire exposure, as no significant change in the charring rate is observed. The best fit expressions are as follows (21):

$$k_{3,2} = 0.024 \cdot \max \left\{ \frac{t_{ch,2}}{t_f} - 0.41 \quad \text{with PL1 (stone wool) insulation} \right. \quad (21)$$

$$k_{3,2} = 0,043 \cdot \max \left\{ \frac{t_{ch,2}}{t_f} - 0.068 \quad \text{with PL2 (glass wool) insulation} \right.$$

where

$k_{3,2}$ is the post-protection coefficient for the lateral side [-];
 $t_{ch,2}$ is the start time of charring on the lateral side [min].

The consolidation coefficients for the fire exposed side are (22):

$$\begin{aligned}
 k_4 &= 1.3 - 0.0018 \cdot t_a && \text{with PL1 (stone wool) insulation} \\
 k_4 &= 0.0088 \cdot t_a + 2.3 && \text{with PL2 (glass wool) insulation}
 \end{aligned}
 \tag{ 22 }$$

where

k_4 is the consolidation coefficient for the lateral side [-].

The consolidation coefficient for PL1 is negatively correlated with the consolidation time, which shows that for longer consolidation times, the charring rate will be reduced relatively more. For PL2 insulation materials, this effect was not observed. Although the charring rate is lesser than in Phase 3, PL2 insulation materials do not offer as great of protection after the consolidation time. Possibly, PL2 thermal insulation is thermally degrading in case of longer failure and consolidation times.

The above expressions yielded a MSE of 7863 mm⁴ for assemblies with stone wool cavity insulation and 6603 mm⁴ for assemblies with glass wool cavity insulation.

The following graphs (Figure 30, Figure 31, Figure 32, Figure 33) show the comparison of the simulated and calculated relative charred areas. The relative charred areas are calculated by dividing the areas at each timestep by the initial flange area. The above expressions have been used to calculate the charred areas.

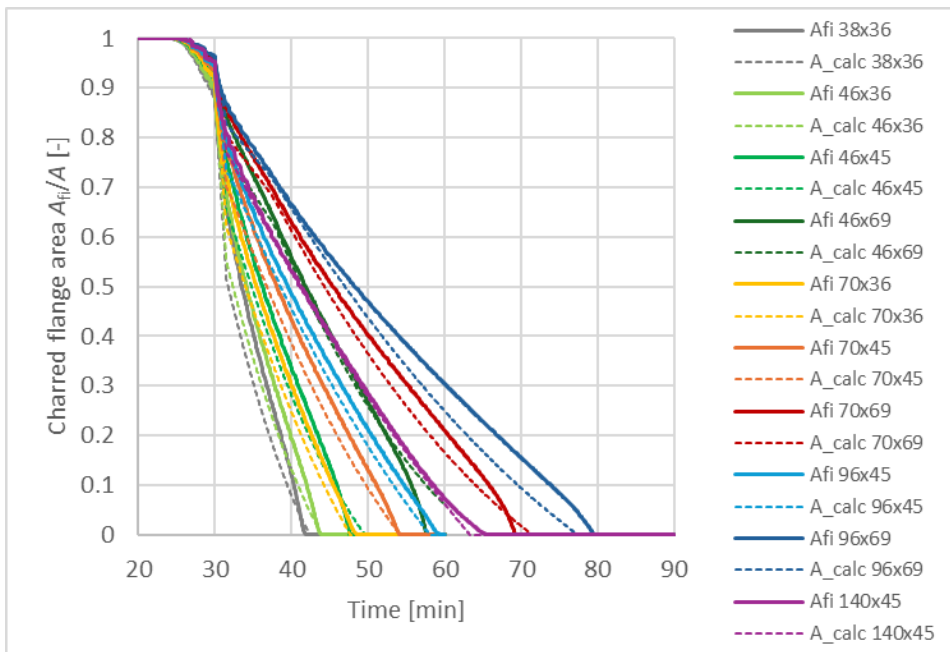


Figure 30. Comparison of simulated and calculated charred areas for assemblies insulated with stone wool and protected by 13-mm gypsum plasterboard with 30-minute fall-off time.

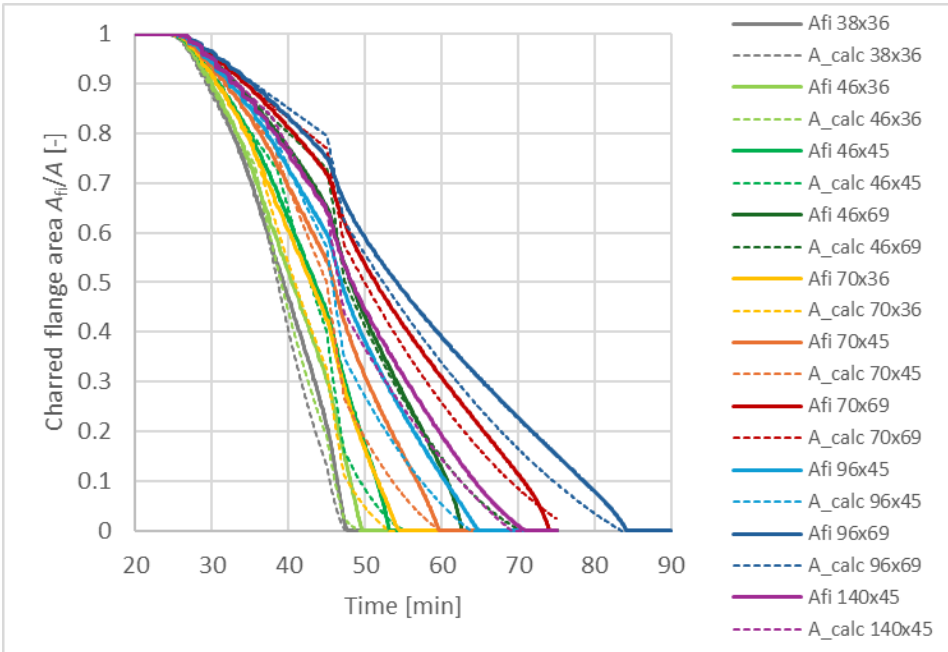


Figure 31. Comparison of simulated and calculated charred areas for assemblies insulated with stone wool and protected by 13-mm gypsum plasterboard with 45-minute fall-off time.

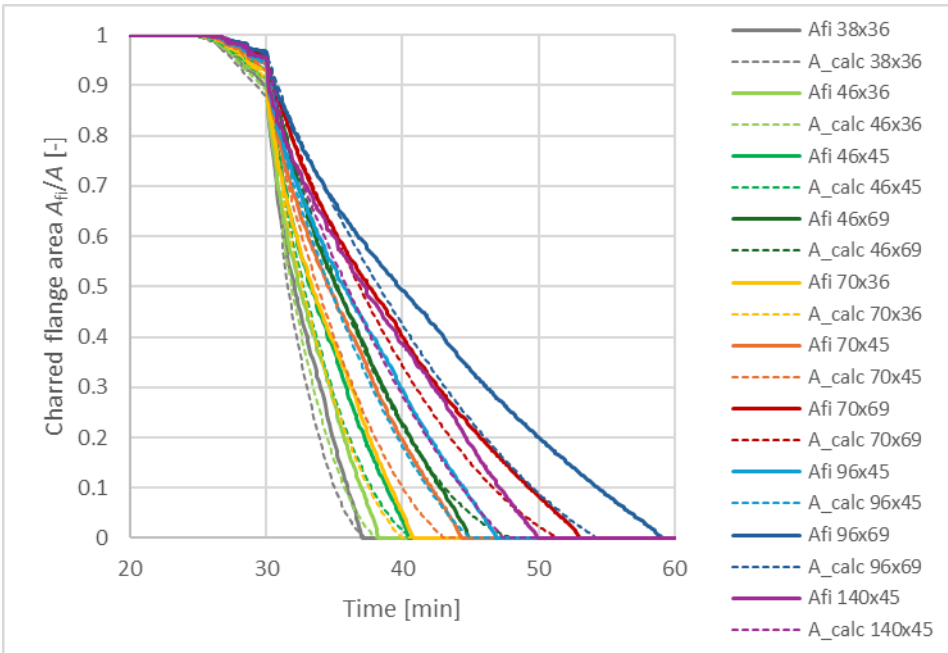


Figure 32. Comparison of simulated and calculated charred areas for assemblies insulated with glass wool and protected by 13-mm gypsum plasterboard with 30-minute fall-off time.

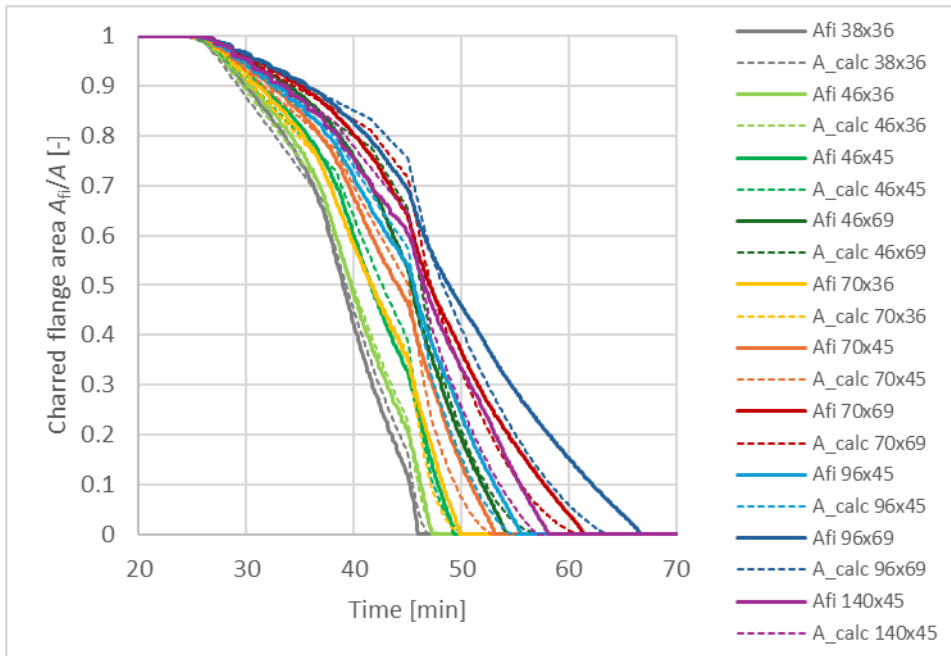


Figure 33. Comparison of simulated and calculated charred areas for assemblies insulated with glass wool and protected by 13-mm gypsum plasterboard with 45-minute fall-off time.

The calculated charred areas are more conservative in the case of shorter fall-off times and larger cross-sections. For the most part, the calculations show slightly smaller areas compared to the simulation results. The calculations are slightly unconservative for short periods of time in the case of long fall-off times and very small cross-sections. The charring is well captured by the developed equations and model parameters.

4 Investigation of mechanical behaviour

The following chapter describes the steps taken to develop the charring model and the parameters shown in Chapters 5.2, 5.3 and 5.4. Mechanical behaviour of I-joists was investigated by loaded model-scale furnace fire tests, normal temperature compression tests and finite element (FE) simulations.

4.1 Loaded model-scale tests

Model scale furnace test data from the FIREWOOD project was available for validation of the design equations. The tests were conducted to investigate the performance of different adhesives used in finger-joints in the tension flange.

4.1.1 Methodology

14 loaded model-scale tests were conducted in the FIREWOOD project with I-joists. In the following, the test specimens and test procedure are described. All data is taken from the report (Olofsson et al., 2022) and Publication III.

Finger-jointed blanks were produced with different adhesives. These blanks had double the width of the flange and were used to produce the fire exposed flanges for two “sister” beams. All beams were tested for modulus of elasticity (MOE). One of the pair of beams was tested at ambient temperature in 4-point bending until rupture and the ratio of bending strength to MOE was determined. The same ratio was assumed for the other beam of the pair and used to determine the fire test load. The fire test specimens were loaded to 40% of the ambient bending strength.

Table 18 shows the MOE, bending strength and applied loads in loaded model-scale tests. The first number in the test beam name represents the adhesive.

Table 18. Loaded model-scale furnace tests.

Test beam	Modulus of Elasticity [MPa]	Bending strength [MPa]	Test load [kN]
		f_m	F
1.2	11600	28.3	2.53
2.2	12412	35.5	3.10
2.4	11718	28.8	2.57
3.3	11301	26.9	2.41
4.3	13824	40.9	3.55
5.1	12902	33	3.0
5.2	15564	47.5	4.08
6.3	14489	43.4	3.75
7.4	12930	34.3	3.01
8.3	13556	39.8	3.46
8.4	13774	38.1	3.1
8.4	13774	38.1	3.1
9.2	12399	35.5	3.11
11.1	12902	33	3.0

11.2	13995	41.5	3.6
11.4	12410	35.5	3.1
12.2	12412	35.5	3.1
12.3	14489	43.4	3.5
12.4	13774	38.1	3.32

Five additional tests with the same configuration were conducted on extra beams from the batch produced for the project. These tests have been included in the current analysis.

In the following, the test specimens and test procedure are described. All data is taken from the report (Olofsson et al., 2022).

The loaded model scale tests were conducted with the aim of investigating the load-bearing behaviour of different adhesives in the finger joints of the fire exposed flange. For that reason, there were 3 finger joints in the middle of the beam span. Temperatures were measured by several type K thermocouples mounted in the specimen at various locations (see Figure 34). All I-joists had a total depth of 200-mm and the flange dimensions 47x47 mm.

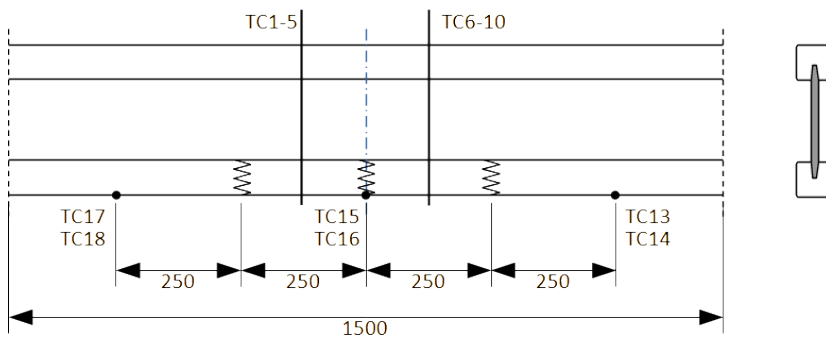


Figure 34. Location of thermocouples and finger-joints.

The beams were initially protected by a 15-mm thick gypsum plasterboard type F. The tested beam was protected on both sides by stone wool cut into the shape of the I-joists. The sides of the specimen had steel clamps holding the gypsum in front of the specimen. The backing board (OSB) was cut into strips to prevent it from taking any load. See Figure 35 for the section of the specimen with more detailed placements of thermocouples.

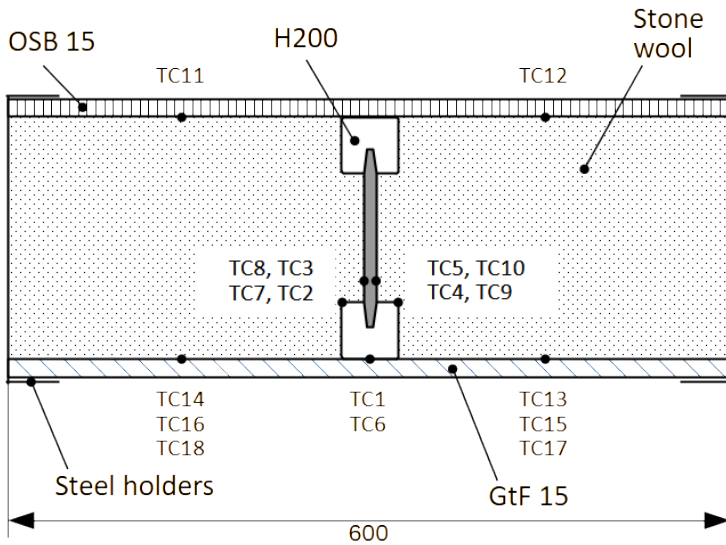


Figure 35. Section of the specimen and location of thermocouples.

The specimens were loaded to 40% of the estimated bending strength at ambient temperature. Loading was applied outside the furnace, with pushing cylinders (see Figure 36).

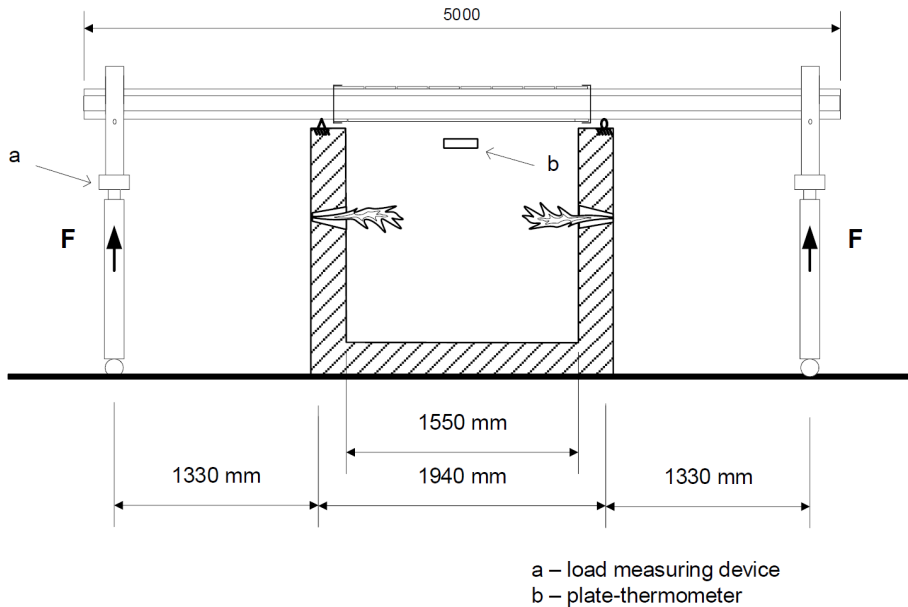


Figure 36. Loaded model-scale test setup from the FIREWOOD report (Olofsson et al., 2022).

The tests were conducted until rupture and then extinguished quickly with water to preserve the residual charred cross-section. Slices were cut from the I-joists close to the rupture and thermocouples.

4.1.2 Results and analysis

The tested start times of charring, fall-off times of gypsum boards, test durations and failure descriptions for loaded model-scale tests are shown in Table 19.

Table 19. Tested start times of charring, fall-off times of gypsum boards and test durations from loaded MST.

Test beam	Start time of charring [min]	Fall-off time [min]	Start of lateral charring [min]	Residual area [mm ²]	Test duration [min]	Failure description
	t_{ch}	t_f	$t_{ch,2}$	A_{res}	t_{test}	
1.2	17.8	20.3	-	1706	24.3	Side joint, adhesive
2.2	20.3	-	-	2034	26.4	Middle joint but also on the cold side finger joint
2.4	17.5	19.8	27.8	1130	29.7	
3.3	19.0	19.9	23.5	1064	29.3	No joint failure
4.3	19.0	-	-	2209	22.5	Middle joint, adhesive/wood
5.1	-	-	-	2209	23.1	
5.2	-	-	-	2209	11.7	Side joint, adhesive/wood
6.3	20.9	-	-	1505	38.8	Side joint, wood finger
7.4	-	-	-	2209	15.2	Side joint, adhesive
8.3	19.7	-	-	1979	26.1	Middle joint, knot adhesive, wood
8.4	26.5	-	-	n/a	36.7	Side joint, wood finger
8.4-2	-	-	-	2183	23.9	
9.2	21.1	-	-	2022	24.1	Middle joint, adhesive/wood
11.1	25.4	-	-	1663	36.7	
11.2	11.7	11.7	-	2209	12.1	Side joint, finger, knot wood
11.4	20.5	-	-	2209	29.4	
12.2	25.8	-	-	2130	26.6	
12.3	25.4	-	-	1705	36.3	
12.4	21.2	-	-	1912	32.4	

Figure 37 shows the recorded deflections from all loaded model-scale tests. The different adhesives are each shown in a different colour.

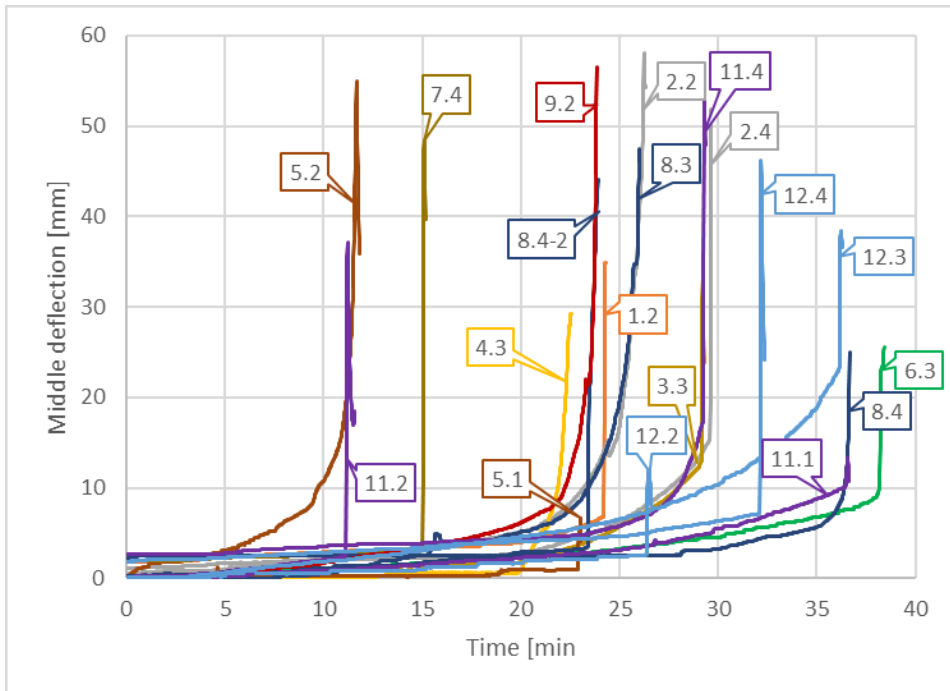


Figure 37. Deflections from loaded MST.

The variability of the loaded MST results can be somewhat attributed to the effect of knots and different adhesive performance. Knots in machine graded timber (such as was used in the flanges) may become relatively more prevalent as the char depth increases. Additionally, they may have been invisible within the timber planks and occurred close to the finger joints.

Various adhesives perform differently at elevated temperatures. Some decline in stickability at temperatures below the charring temperature of timber. Based on the adhesive classification methods developed within the FIREWOOD project, the adhesive performance is divided into three classes. The adhesive classification method is given in Chapter B.4 of FprEN 1995-1-2:2025 (CEN, 2025b).

4.2 Mechanical FE simulations

Mechanical FE simulations were conducted in order to analyse the structural performance of I-joists in bending at elevated temperatures and in fire. The FE simulation results were compared to loaded model-scale test results.

Unfortunately, the deflections from the mechanical simulations differed from the fire tests. The FE results were much stiffer and showed less deflection and shorter resistance times. Therefore, the mechanical simulation results were only generally compared with the design model.

The possible reason for the difference in the deflections is the behaviour of adhesives which is not considered explicitly in the simulations. Additionally, the cross-section is assumed to remain planar in the simulations but may distort in the tests, therefore being able to deflect more while still taking the imposed load.

4.2.1 Methodology

The structural analysis in SAFIR is a sequential process, where first the temperatures in the cross-section are calculated and this output file is further used as one of the inputs for the mechanical analysis. In SAFIR, the mechanical analysis does not influence the temperature field in the structure. This simplification may not be entirely realistic, especially in cases with cracks forming due to large deformations.

The mechanical simulations were conducted on 2D BEAM elements using the SAFIR v2022.a.2 software. Each BEAM element is defined by three nodes which have three degrees of freedom. A static analysis is conducted using pure Newton-Raphson procedure for convergence. Precision value 0.002 was used as the convergence criterion.

The thermal simulation input files were prepared according to the cross-sections and protection applied in the loaded model-scale furnace tests. The duration of the thermal simulations was also similar to the tests.

The mechanical simulation input file was created to mimic the setup used in the furnace tests. The length of the beam was divided into approximately equal parts (called beams in the input) so that the load, the supports and the edges of the furnace were defined at the nodes surrounding the elements (see Figure 38). In the following figure, the elements in orange are exposed to the standard fire and elements in blue are at ambient conditions. The black dots signify nodes. Each beam element has two end nodes and one middle node.

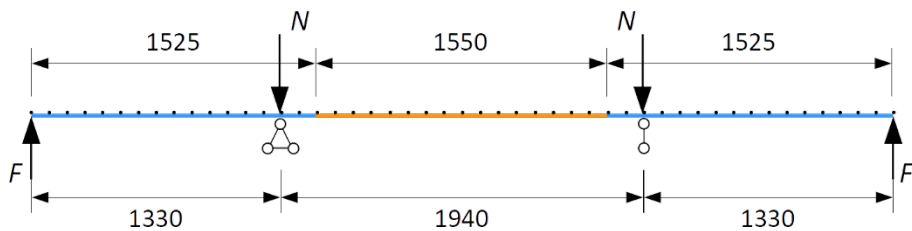


Figure 38. Thermo-mechanical simulation setup.

The mechanical simulation in SAFIR needs one continuous temperature file per section (i.e. for orange or blue parts in Figure 38). The only way to simulate fall-off of gypsum is to conduct two thermal simulations. These yield two temperature files. Script 6 was used to combine the temperature files before and after fall-off. the script is described in chapter 4.2.1.1.

The deflections measured in loaded model-scale furnace tests as presented in chapter 4.1 and the mechanical simulations were compared. An attempt was made to calibrate the thermo-mechanical simulations to fit the test results. The mechanical properties of the I-joists were changed but the fit was not improved significantly.

Mechanical properties of OSB/3 were taken according to EN 12369-1, elastic modulus in bending 4930 MPa, bending strength 18 MPa, compression strength 15.9 MPa, tensile strength 9.9 MPa.

A subsequent thermo-mechanical simulation study was conducted to further investigate the zero-strength layer depths depending on the applied load, cross-section dimensions, thermal insulation and fire protection. Bending was simulated.

The first set of thermo-mechanical simulations within this further study were conducted on a variety of setups shown in Table 20. Both stone wool and glass wool thermal insulation were simulated. The mesh size for the thermal simulations was similar to the mesh used in the thermal simulations as described in the previous chapter.

Table 20. Overview of thermo-mechanical simulations.

Depth H (mm)	Flange sizes b×h (mm)	Protection h_p/t_f , (mm/min)
200	38×36	13/30, 15/45, 15/60, 20/60
	46×45	13/30, 15/45, 15/60, 20/60
	70×69	13/30, 15/45, 15/60, 20/60
	96×45	13/30, 15/45, 15/60, 20/60
400	46×45	13/30, 15/45, 15/60, 20/60
	70×69	13/30, 15/45, 15/60, 20/60
	96×45	13/30, 15/45, 15/60, 20/60
600	70×69	13/30, 15/45, 15/60, 20/60
	96×45	13/30, 15/45, 15/60, 20/60

Reversed 4-point bending was implemented in the mechanical simulations with a load of 40% of the maximum bending strength applied. The total length of the beam and the support and load distances were chosen according to EN 408:2010 (CEN, 2010). The standard provides the distances as a function of the total beam depth (H), all beam elements in the mechanical analysis were chosen to be the same length as the beam depth H. The ends of the beam were at ambient temperature.

See Figure 39 for the element length, beam length and thermal exposure used in the reverse 4-point bending simulations. In the following figure, the elements in orange are exposed to the standard fire and elements in blue are at ambient conditions. The black dots signify nodes. Each beam element has two end nodes and one middle node. “H” denotes the cross-section height.

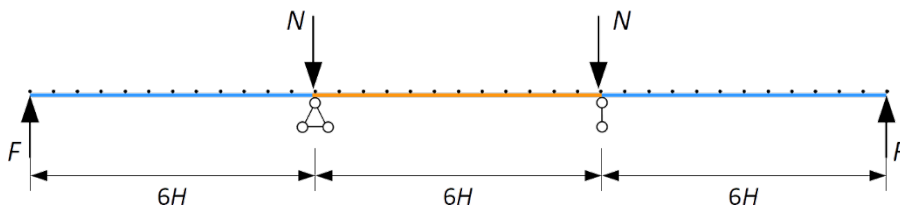


Figure 39. Schematic of mechanical simulation beam.

Two temperature files were created for each one mechanical analysis – one for the fire exposed middle part and the other for the “cold” ends. According to Table 18, the fire exposed part was subjected to fall-off of gypsum. Therefore, the two thermal output files were merged using a MATLAB script.

The output of thermo-mechanical simulations are the time-deflection graphs and the last time to reach convergence, which was taken as the total fire resistance time.

4.2.1.1 Script 6

The purpose of script 6 is the preparation of thermal data files for mechanical simulations in the case of fall-off of gypsum board.

SAFIR has a peculiarity that it easily allows the user to remove a part of the structure in thermal simulations. This is typically used to simulate a part of the structure, such as a gypsum board, falling off of the structure. This is done using a continuation command. The result is two temperature files, the first one until the fall-off and the second after.

The mechanical analysis is conducted strictly after the thermal analysis is finished. For the thermo-mechanical simulation, the inputs are the thermal file and the separate mechanical input file which includes the information about the loads, supports and the load-bearing member. Temperatures must be given for all parts of the member.

In the case of fall-off of a part of the structure, the two thermal files must be combined in order for them to be accessible for the thermo-mechanical simulation. For this purpose, script 6 was prepared.

This script would determine the numbers of nodes which are present throughout the fire duration (both before and after fall-off). Then, the temperature data from the first and second thermal output files are combined sequentially over time, while keeping only the data of nodes which are in place throughout the exposure.

4.2.2 Results and analysis

The overview of results of mechanical simulations is given below. The main phenomena investigated in the thermo-mechanical simulations are deflection and the fire resistance time as the time when the simulation cannot reach convergence.

The criterion of the time to converge was chosen as the end of the simulation due to the large differences in the deflections as seen in the following figures. The calibration of mechanical properties was unsuccessful as the lowering of the strength and/or stiffness shortened the simulation end time but did not significantly change the deflection.

The comparisons of deflections from loaded model-scale furnace fire tests are shown in Figure 40 and Figure 41.

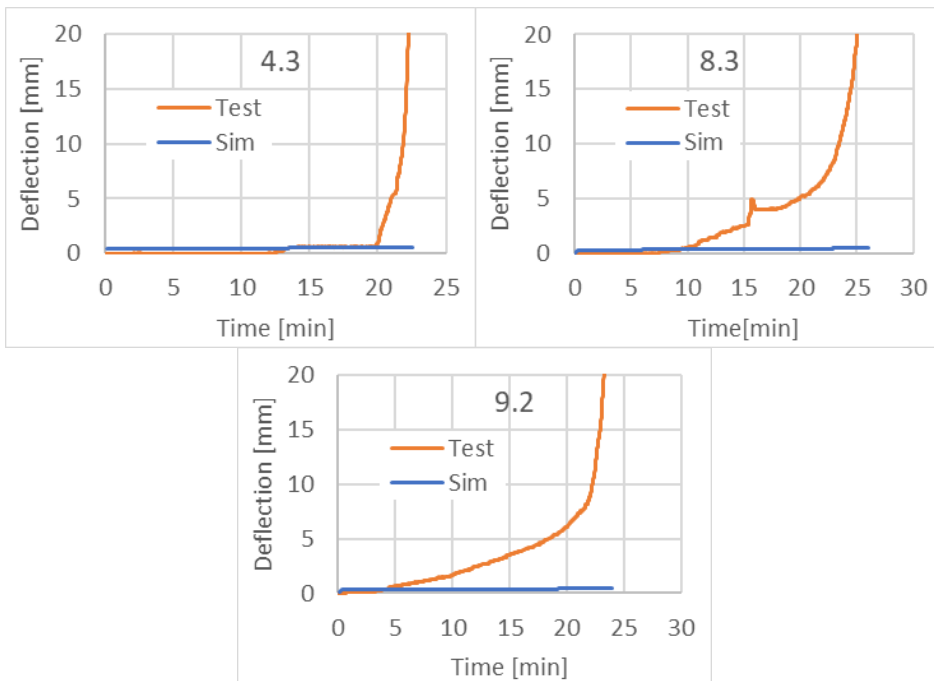


Figure 40. Comparison of deflections from loaded model-scale tests, part 1.

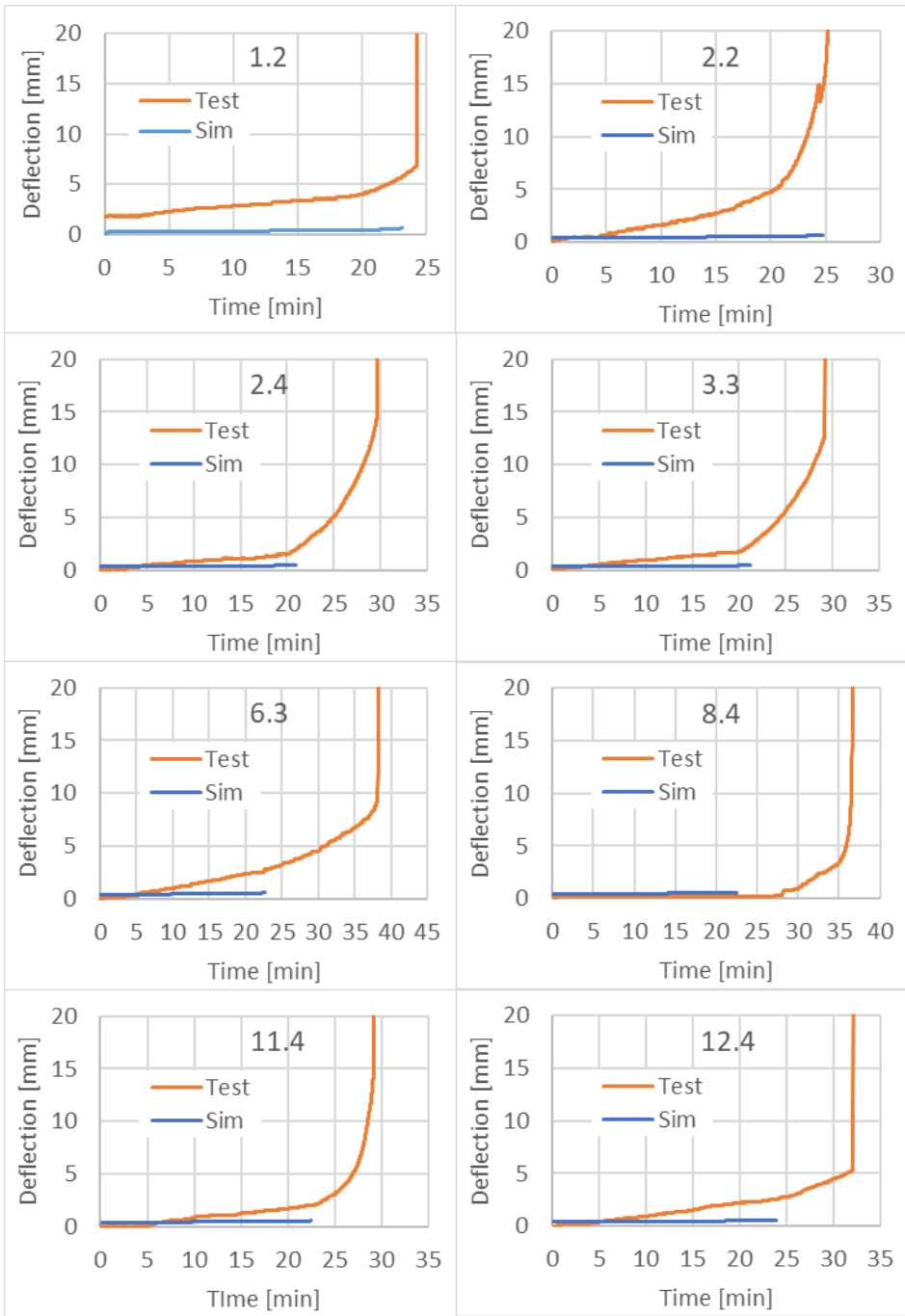


Figure 41. Comparison of deflections from loaded model-scale tests, part 2.

Simulations stop reaching convergence much earlier than the failure occurred in the tests in the cases displayed in Figure 41. For the cases shown in Figure 40, the simulations are longer than the tested failure times. The deflections are mostly much smaller than test measurements. These effects (shorter duration and less deflection) may be related

to the simulation assumptions which may not be entirely valid for the real behaviour leading to the simulations not being able to reach convergence.

The cross-section is assumed to remain planar in the simulations. When the simulation cannot reach an equilibrium in the forces and the strength, it will stop converging. However, in the tests it seems possible that the large deflections are caused by non-planarity of the section. Some torsion or other warping of the section could occur in the test beams and be recovered after the break and extinguishment.

The second set of thermo-mechanical simulations was compared to calculation results obtained from the same configurations. The results of the calculations and simulations are shown in Table 21 and Figure 42.

Table 21. Simulated and calculated load-bearing capacities and times to failure.

Depth [mm]	Flange size [mm]	Protection [mm/min]	Bending moment [kNm]	Simulation duration [min]	Bending capacity [kNm]	Calculated duration [min]
H	$b_f \times h_f$	h_p/t_f	M_{sim}	t_{sim}	M_{calc}	t_{calc}
200	38x36	13/30	2.35	22.7	1.93	15.3
200	38x36	15/45	2.35	26.8	1.89	16.1
200	38x36	15/60	2.35	26.8	1.89	16.1
200	38x36	20/60	2.35	37.6	1.64	18.3
200	46x45	13/30	3.07	27	1.83	22.8
200	46x45	15/45	3.07	31.5	1.96	26.4
200	46x45	15/60	3.07	31.5	1.96	26.4
200	46x45	20/60	3.07	43.4	2.19	30.1
200	70x69	13/30	5.24	34.6	3.04	28.6
200	70x69	15/45	5.24	43.6	2.66	33.4
200	70x69	15/60	5.24	43.6	2.66	33.4
200	70x69	20/60	5.24	56.6	2.59	45.8
200	96x45	13/30	6.27	30.1	4.80	26.2
200	96x45	15/45	6.27	34.9	4.96	31.2
200	96x45	15/60	6.27	34.9	4.96	31.2
200	96x45	20/60	6.27	47	5.21	44.0
400	46x45	13/30	8.98	10.7	8.86	9.8
400	46x45	15/45	8.98	12.1	8.76	10.3
400	46x45	15/60	8.98	12.1	8.76	10.3
400	46x45	20/60	8.98	15.9	8.54	11.7
400	70x69	13/30	16.32	29.3	13.04	25.1
400	70x69	15/45	16.32	33.8	13.27	29.8
400	70x69	15/60	16.32	33.8	13.27	29.8
400	70x69	20/60	16.32	45.8	13.59	42.3

400	96x45	13/30	17.19	23.5	16.98	23.3
400	96x45	15/45	17.19	27.5	17.50	28.3
400	96x45	15/60	17.19	27.5	17.50	28.3
400	96x45	20/60	17.19	37.3	16.81	34.0
600	70x69	13/30	29.45	24.9	26.49	22.7
600	70x69	15/45	29.45	29.1	27.25	25.0
600	70x69	15/60	29.45	29.1	27.25	25.0
600	70x69	20/60	29.45	40.3	26.96	28.5
600	96x45	13/30	29.85	11.1	30.88	15.5
600	96x45	15/45	29.85	12.6	30.67	16.3
600	96x45	15/60	29.85	12.6	30.67	16.3
600	96x45	20/60	29.85	16.5	30.26	18.6

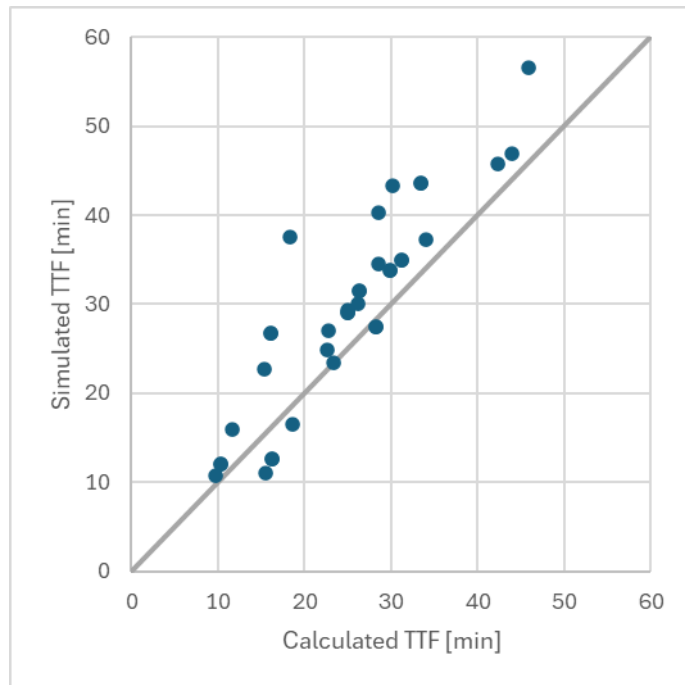


Figure 42. Comparison of simulated and calculated times to failure.

The calculated times to failure are mostly conservative compared to the simulations. The cases which are below the line (unsafe side) in Figure 42 are quite specific, meaning that in those cases the failure in the simulations occurred before the start of charring. The simulations for the 600-mm cross-section stopped converging quite early.

4.3 Thermal FE simulations with strength reduction factors

Thermal FE simulation results were combined with the temperature-dependent strength reduction factors in order to analyse the loss of strength of the fire exposed flange at elevated temperatures. The goal of this analysis is the calculation of the zero-strength layer depths for each simulation case for all timesteps.

4.3.1 Methodology

The temperature-dependent mechanical response of timber-based materials was calculated according to the strength and stiffness reduction factors given in Table 22. Timber loaded in tension parallel to the grain was considered to fail in a brittle manner, with rupture occurring once the reduced tensile strength was exceeded. In compression parallel to the grain, the behaviour was assumed to be more plastic-like, allowing for limited stress redistribution before failure. In bending members, failure was governed by tensile rupture on the tension side, while the compressive zone was assumed capable of plastic deformation until instability or crushing occurred.

Unless stated otherwise, the flanges were simulated with sawn wood of the strength class C24 according to EN 338:2016 (CEN, 2016) and the web with OSB/3 according to EN 300:2006 (CEN, 2006) and EN 12369-1:2005 (CEN, 2005).

Table 22. Mechanical properties of timber at elevated temperatures used in FE simulations.

T [°C]	Strength			Modulus of elasticity		
	Compression	Tension	Shear	Compression	Tension	Shear
20	1.00	1.00	1.00	1.00	1.00	1.00
100	0.25	0.65	0.40	0.35	0.50	0.40 ¹
300	0	0	0	0	0	0

Note: ¹ Value for rolling shear from FprEN 1995-1-2:2025

4.3.1.1 Script 4

Script 4 was developed in MATLAB to analyse the reduction of strength in the fire exposed flange. The reduction in strength was analysed based on the same set of thermal simulations from Chapter 3.2 by substituting the average temperature in each element of the wood flange with the tensile or compressive strength reduction factors corresponding to that temperature. The reduction factors were taken from FprEN 1995-1-2:2025 (CEN, 2025b).

The fire exposed flange was comprised of 1x1 mm² elements in the thermal simulations. Therefore, the strength reduction factor based on the average temperature in each element is equal to the effective area of that element. The effective areas of the flange for each timestep were calculated as the sum of all elements of the flange. The areas are used for the development of the zero-strength layer depth expressions.

4.3.2 Results and analysis

The resulting effective areas from the analysis of Script 4 are shown in Figure 43 and Figure 44 for assemblies with stone wool and 15-mm gypsum plasterboard with a 30-minute failure time.

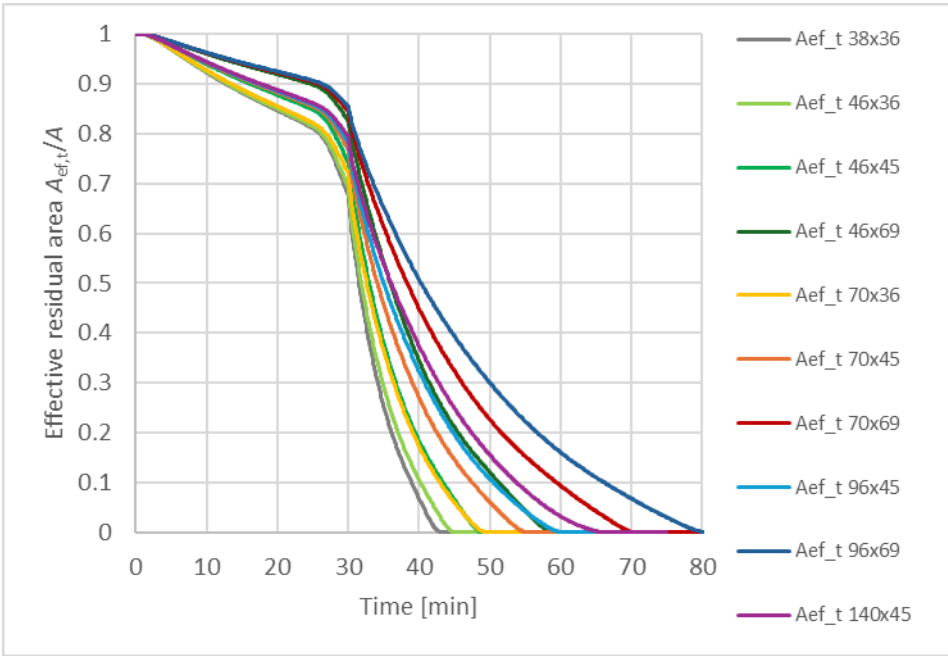


Figure 43. Effective areas in tension of simulations with 15-mm thick gypsum with 30-min fall-off time with stone wool.

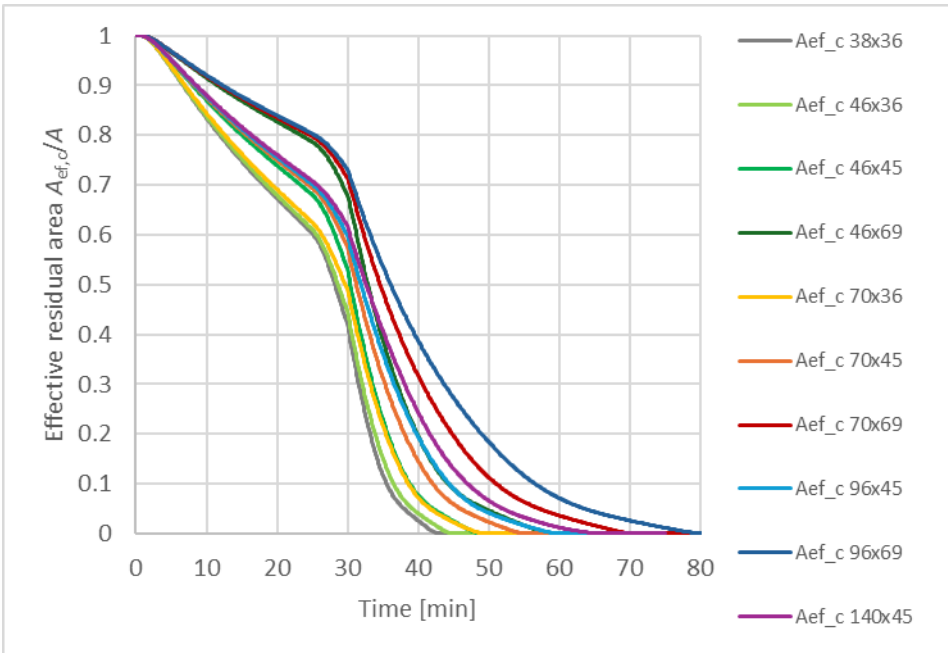


Figure 44. Effective areas in compression of simulations with 15-mm thick gypsum with 30-min fall-off time with stone wool.

4.4 Development of zero-strength layer depth expressions

4.4.1 Methodology (Script 5)

The calculation of the zero-strength layer depth and the development of the expressions utilised Script 5 and the effective flange areas from simulations.

The effective areas at each timestep are smaller than the charred areas, as the strength of timber is reduced also at temperatures lower than 300 °C. The rectangular charred area for each timestep is calculated according to equation (23):

$$A_{fi}(t) = (h_f - d_{char,n,1}(t)) \cdot (b_f - 2 \cdot d_{char,n,2}(t)) \quad (23)$$

where

- A_{fi} is the charred area of the flange [mm²];
- h_f, b_f are the initial flange height and width [mm];
- $d_{char,n,1}$ is the notional char depth on the fire exposed side [mm];
- $d_{char,n,2}$ is the notional char depth on the lateral side [mm].

The depth of the zero-strength layer must compensate for the difference between the charred and effective areas. The depth of the zero-strength layer was simplified to be equal for the fire exposed side and the lateral sides of the flange. The rectangular effective area is calculated according to equation (24):

$$A_{ef}(t) = (h_f - d_{char,n,1}(t) - d_0(t)) \cdot (b_f - 2 \cdot d_{char,n,2}(t) - 2 \cdot d_0(t)) \quad (24)$$

where

- A_{ef} is the effective area of the flange [mm²];
- d_0 is the zero-strength layer depth [mm].

The notional char depths were calculated based on the previously developed charring equations. The depth of the zero-strength layer was calculated by solving the quadratic equation (25) for d_0 and accepting the smaller positive solution. The charred area at each timestep $A_{fi,calc}(t)$ is calculated according to the equations in chapter 3.3.2 and the effective area for each timestep $A_{ef,sim}(t)$ is taken from the simulation results.

$$2 \cdot d_0^2(t) - (2 \cdot h_{fi} + b_{fi}) \cdot d_0(t) + A_{fi,calc}(t) - A_{ef,sim}(t) = 0 \quad (25)$$

where

- h_{fi}, b_{fi} are the calculated charred flange height ($h_{fi} = h_f - d_{char,n,1}$) and width ($b_{fi} = b_f - 2 \cdot d_{char,n,2}$) [mm];
- $A_{fi,calc}$ is the calculated charred area of the flange ($A_{fi} = h_{fi} \cdot b_{fi}$) [mm²].

The depths of the zero-strength layer were calculated separately for tension and compression and stone and glass wool insulation.

The equations to calculate the zero-strength layer depth were fitted to the results of equation (25) using a two-part regression approach. A piecewise function consisting of two parts was implemented separately for tension and compression. The zero-strength layer depths were fitted with:

1. A constrained linear model before the start time of charring t_{ch} ;
2. A quadratic polynomial model after t_{ch} .

The linear part was constrained with the intercept at 0 according to equation (26):

$$d_0(t \leq t_{ch}) = a_1 \cdot t \quad (26)$$

where

- a_1 is the slope of the linear segment [-].

After finding the slopes for all simulation cases before the start of charring, the equation to calculate the zero-strength layer depth for this time period was found using stepwise regression. The regression script would check The protection coefficient k_2 and the flange dimensions were chosen as the possible terms. The interaction (multiplication) of terms was allowed.

The quadratic segment was fitted with continuity at time t_{ch} according to equation (27):

$$d_0(t > t_{ch}) = a_2 \cdot (t - t_{ch})^2 + b_2 \cdot (t - t_{ch}) + c_2 \quad (27)$$

where

a_2 is the quadratic term in the second segment [-];

b_2 is the linear term in the second segment [-];

c_2 is the intercept in the second segment [-].

The intercept c_2 was calculated for each case according to the equation from step 1.

After finding the quadratic model parameters for all simulation cases after the start of charring, the equation to calculate the zero-strength layer depth for this time period was found using stepwise regression. Each factor (a_2 , b_2) was fitted using the flange dimensions, failure time t_f and gypsum board thickness h_p as the possible terms. The interaction (multiplication) of terms was allowed.

The fit was assessed across all simulation results using the coefficient of determination (R^2), mean square error (MSE) and root mean square error (RMSE) metrics.

4.4.2 Results and analysis

Some examples of the depths of the zero-strength layer over the fire duration obtained from simulations are shown in the following graphs.

Figure 45 to Figure 48 present the d_0 in tension or compression members in assemblies with stone wool protected by a 15-mm gypsum plasterboard with a fall-off time of 30 or 60 minutes. Figure 49 to Figure 52 present the d_0 in tension or compression members in assemblies with glass wool protected by a 15-mm gypsum plasterboard with a fall-off time of 30 or 60 minutes.

Generally, the depth of the zero-strength layer is greater for compression members than for the same sized flanges in tension. The depth is also influenced by the flange size and the fall-off time of the protection layer. Additionally, there is some development of the d_0 before the start of charring. The graphs have a linear tendency until about the start time of charring. There is a dip after the fall-off time and a non-linear shape after that. The decrease of the depth after the fall-off time can be explained by the rapid increase in the charring rate in phase 3 which occurs for a brief time after fall-off. This phase represents the charring of the preheated wood which is opened to the fire and, therefore, chars at a rapid rate causing the decrease in the zero-strength layer depth.

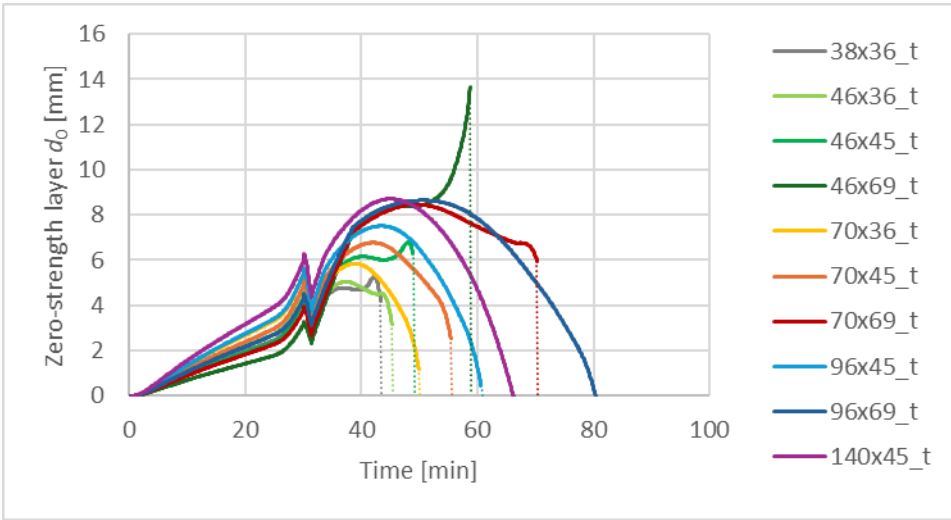


Figure 45. Zero-strength layer depths for tension in assemblies insulated with stone wool and protected by 15-mm gypsum plasterboard with 30-minute fall-off time.

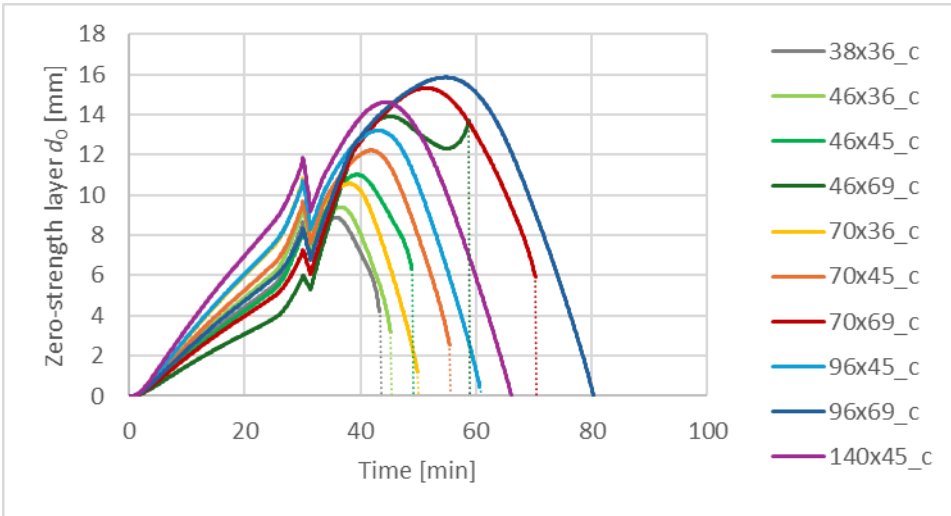


Figure 46. Zero-strength layer depths for compression in assemblies insulated with stone wool and protected by 15-mm gypsum plasterboard with 30-minute fall-off time.

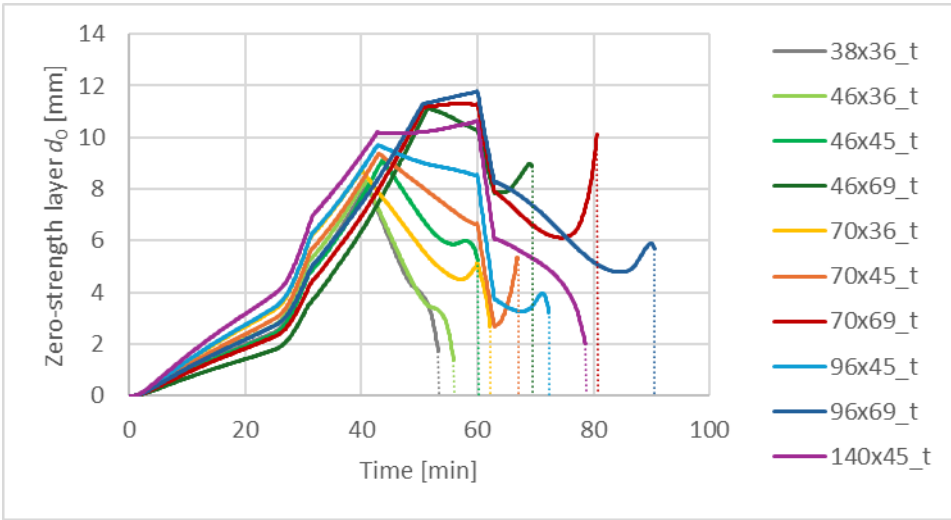


Figure 47. Zero-strength layer depths for tension in assemblies insulated with stone wool and protected by 15-mm gypsum plasterboard with 60-minute fall-off time.

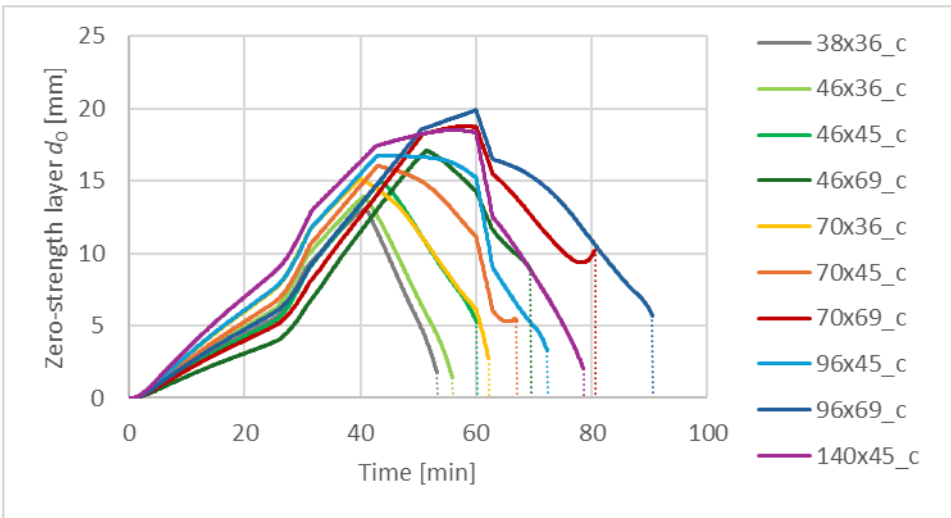


Figure 48. Zero-strength layer depths for compression in assemblies insulated with stone wool and protected by 15-mm gypsum plasterboard with 60-minute fall-off time.

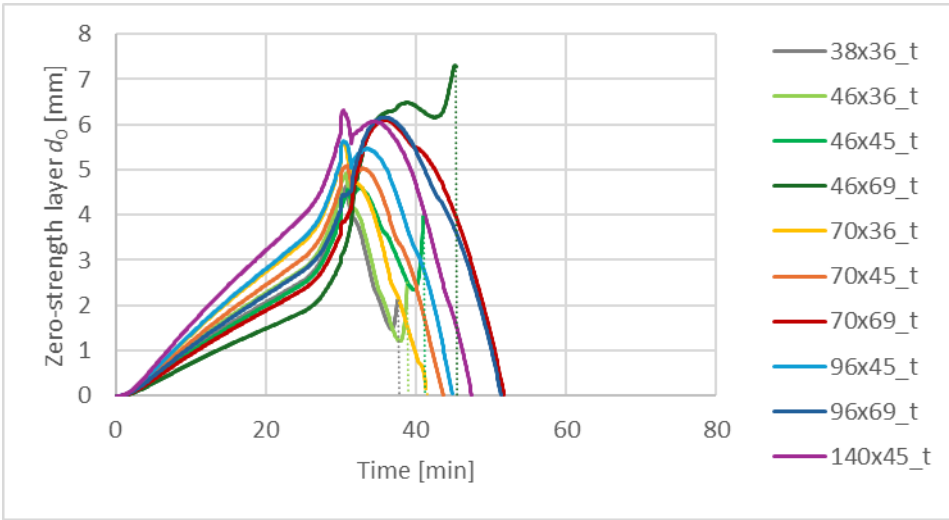


Figure 49. Zero-strength layer depths for tension in assemblies insulated with glass wool and protected by 15-mm gypsum plasterboard with 30-minute fall-off time.

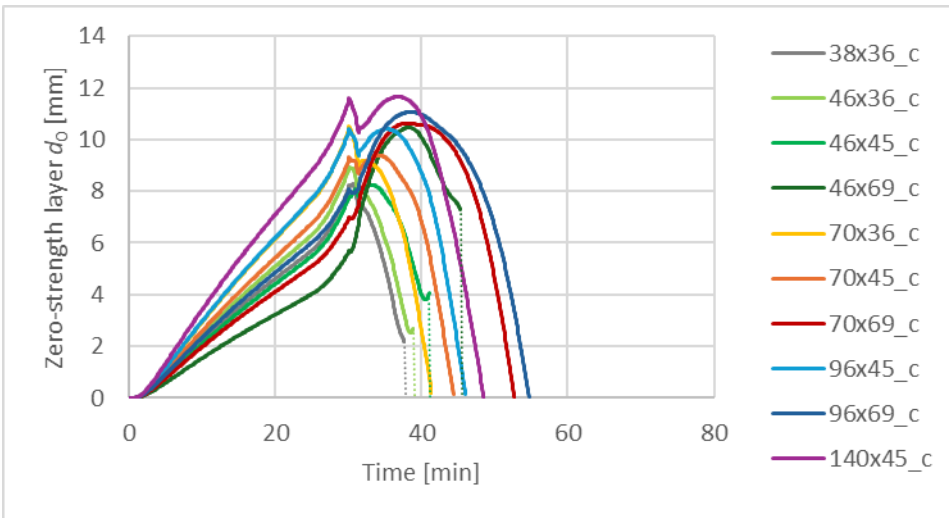


Figure 50. Zero-strength layer depths for compression in assemblies insulated with glass wool and protected by 15-mm gypsum plasterboard with 30-minute fall-off time.

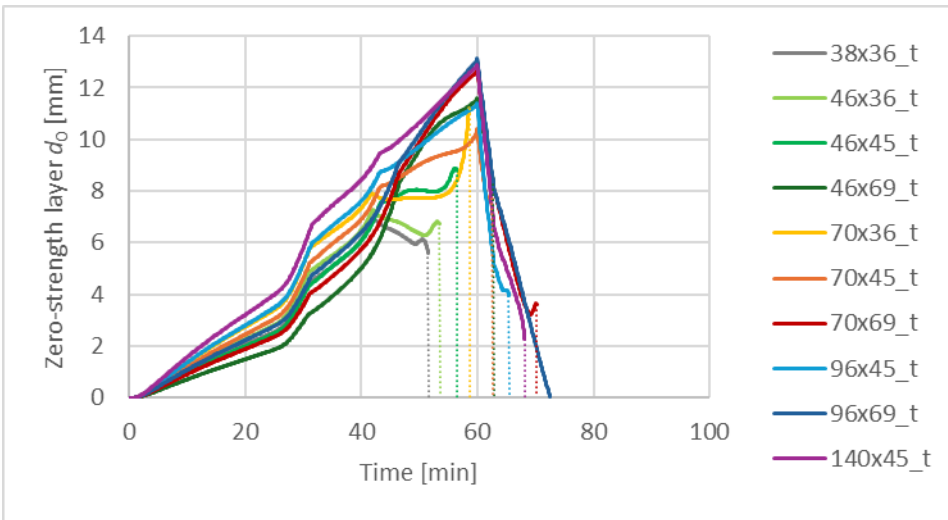


Figure 51. Zero-strength layer depths for tension in assemblies insulated with glass wool and protected by 15-mm gypsum plasterboard with 60-minute fall-off time.

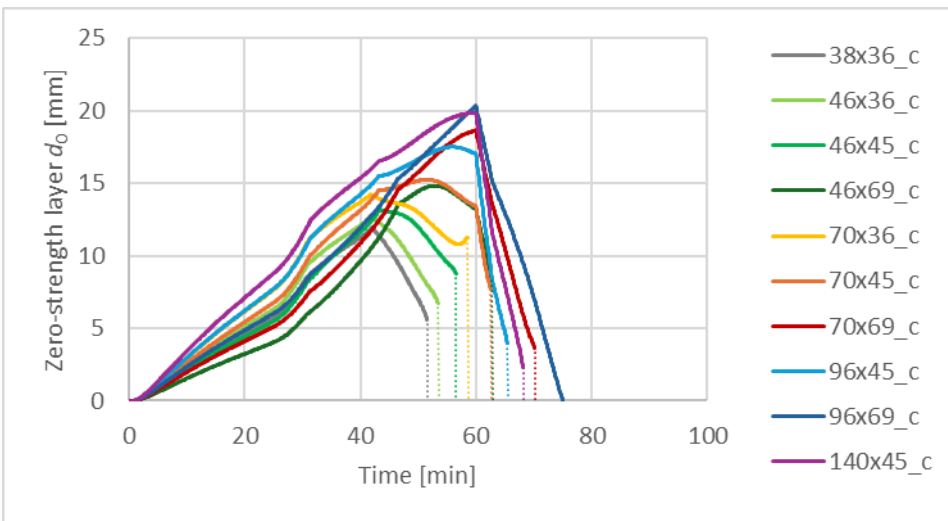


Figure 52. Zero-strength layer depths for compression in assemblies insulated with glass wool and protected by 15-mm gypsum plasterboard with 60-minute fall-off time.

The zero-strength layer depths are greater for compression compared to tension members. Assemblies with stone wool cavity insulation show longer fire resistance, especially after the fall-off of gypsum protection compared to glass wool cavity insulation. Generally, the development of the zero-strength layer depth is linear until the start time of charring, after which the depth increases more rapidly until the fall-off time. After that, the depth decreases (due to the fast charring) in a non-linear shape.

In some extreme cases, the graphs show an increase in the zero-strength layer depth at the end of the exposure. This is explained by the methodology of calculating the depth as a difference of the calculated charred area and the simulated effective area. In some

cases, the calculated charred area is larger than in the simulations and therefore, the depth of the zero-strength layer is increased to compensate.

The zero-strength layer depths were calculated by solving a quadratic equation derived from the assumption that the depth is equal for the fire exposed and the lateral sides of the fire exposed flange. The independent variable was the time.

The zero-strength layer depths increase mostly linearly between the start of the fire exposure and the start time of charring. The slopes were fitted with the assumption that the intercept would be 0 and that the regression line never underestimates the simulated value by more than 5 %.

After the start time of charring the graphs have a quadratic appearance, therefore a quadratic regression was applied with the curve set to start from the end of the linear part.

A stepwise regression with interaction terms was applied to investigate the most significant predictor variables.

For the time before the start of charring, no significant difference was observed between the zero-strength layer depths for I-joists in assemblies with stone and glass wool insulation. Therefore, the derived expressions for tension and compression members were independent of the insulation type, see Table 23. The most significant factors influencing the d_0 are the flange width and the protection factor k_2 .

Table 23. Expressions for zero-strength layer depth from the start of exposure until the start of charring.

Tension	Compression
$d_0 = \frac{k_2}{\ln b_f} \cdot t$	$d_0 = \frac{2k_2}{\ln b_f} \cdot t$

After the start of charring, the zero-strength layer depth is significantly influenced by the flange dimensions (b_f and h_f) and the failure time of the fire protection system t_f . Due to the use of interaction terms, the equations include multiplications or divisions of the terms (b_f , h_f and t_f). Additionally, the different protection offered by stone or glass wool cavity insulation has an effect on the d_0 . Therefore, two sets of equations were developed depending on the cavity insulation for tension and compression members, see Table 24.

Table 24. Expressions for zero-strength layer depth after the start of charring.

Stone wool TENSION	$d_0 = -\frac{1.9 \cdot t_f^{0.42} \cdot (t - t_{ch})^2}{b_f^{0.22} \cdot h_f^{1.5}} + \frac{t_f^{0.76} \cdot (t - t_{ch})}{34.5 \cdot b_f^{0.1}} + \frac{k_2 \cdot t_{ch}}{\ln b_f}$
Stone wool COMPRESSION	$d_0 = -\frac{28 \cdot (t - t_{ch})^2}{t_f^{0.14} \cdot b_f^{0.5} \cdot h_f^{1.1}} + \frac{t_f^{0.4} \cdot (t - t_{ch})}{2.111 \cdot b_f^{0.25}} + \frac{2k_2 \cdot t_{ch}}{\ln b_f}$
Glass wool TENSION	$d_0 = -\frac{3.13 \cdot b_f^{0.035} \cdot (t - t_{ch})^2}{t_f^{0.9} \cdot h_f^{0.5}} + \frac{t_f^{0.8} \cdot b_f^{0.11} \cdot (t - t_{ch})}{83} + \frac{k_2 \cdot t_{ch}}{\ln b_f}$
Glass wool COMPRESSION	$d_0 = -\frac{200 \cdot (t - t_{ch})^2}{t_f^{0.9} \cdot b_f^{0.3} \cdot h_f^{0.9}} + \frac{t_f^{0.5} \cdot (t - t_{ch})}{3.5 \cdot b_f^{0.13}} + \frac{2k_2 \cdot t_{ch}}{\ln b_f}$

The above expressions were compared with simulated d_0 values. The fit was evaluated both visually and by calculating the appropriate metrics as shown in Table 25.

Table 25. Goodness of fit parameters for zero-strength layer expressions.

Insulation	Load	R ² [-]	MSE [mm ²]	RMSE [mm]
SW	Tension	0.6305	3.0675	1.7514
	Compression	0.4493	13.0949	3.6187
GW	Tension	0.3214	4.5098	2.1236
	Compression	-0.0017	19.2226	4.3844

The equations were fitted based on reducing the complexity and the RMSE value. In the following graphs (Figure 53 – Figure 60), some comparisons of calculations and simulations of the effective areas are shown.

As seen below, the effective areas from calculations are conservative compared to simulation results. For approximately the first 30 minutes, the calculations are relatively more conservative. This is due to the examples having a relatively long duration of Phase 0 (encapsulation phase). The calculated effective areas are smaller than the simulated values for nearly all cases and throughout the full duration.

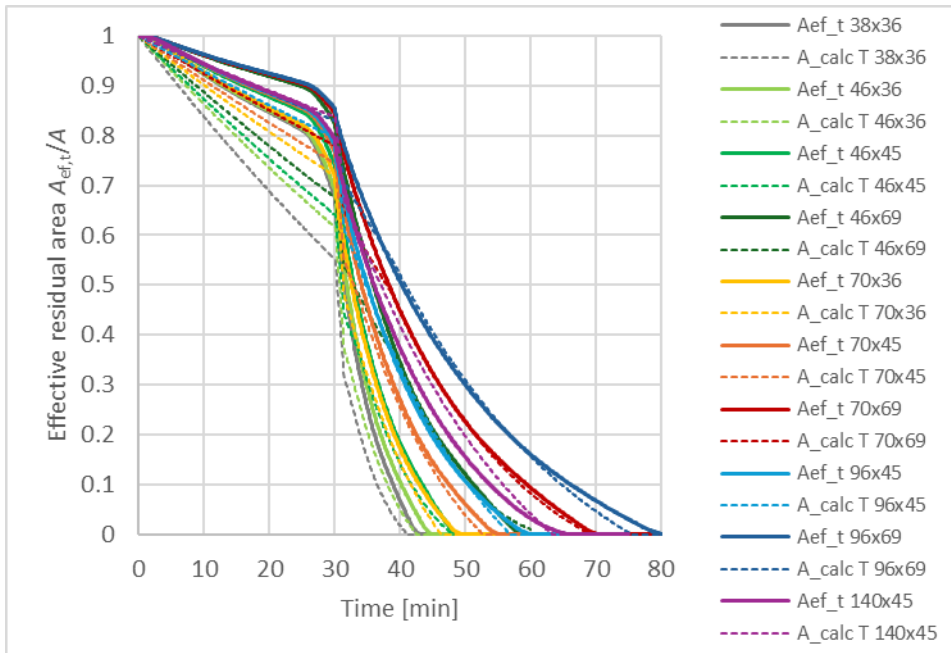


Figure 53. Comparison of simulated and calculated effective areas in tension for assemblies insulated with stone wool and protected by 15-mm gypsum plasterboard with 30-minute fall-off time.

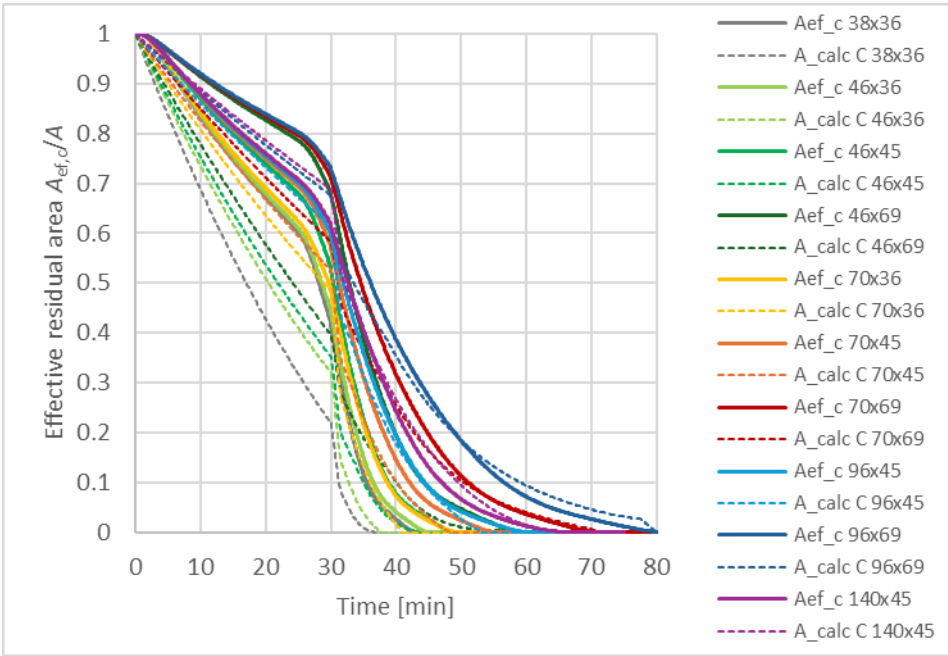


Figure 54. Comparison of simulated and calculated effective areas in compression for assemblies insulated with stone wool and protected by 15-mm gypsum plasterboard with 30-minute fall-off time.

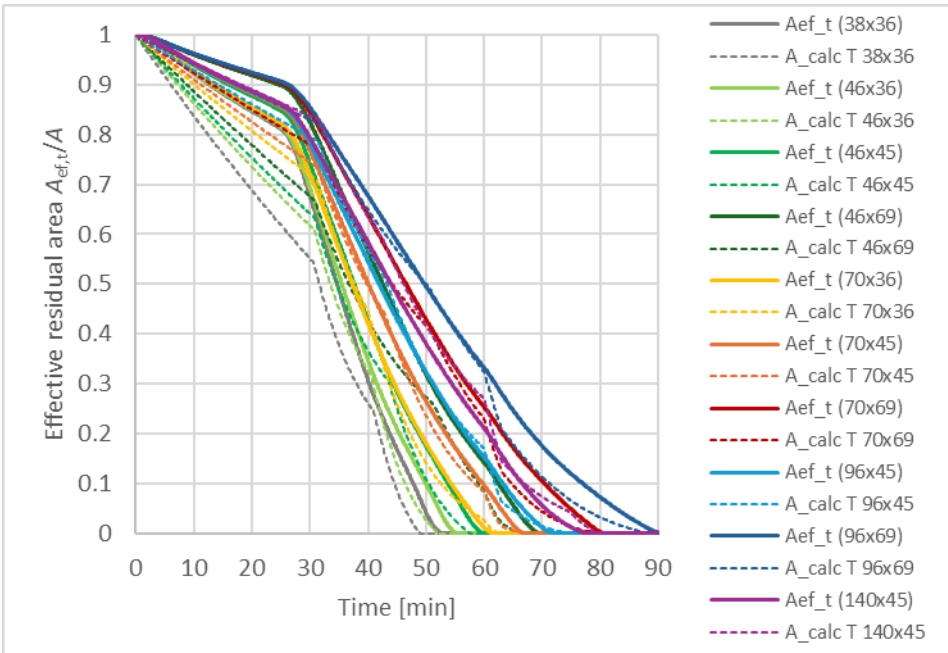


Figure 55. Comparison of simulated and calculated effective areas in tension for assemblies insulated with stone wool and protected by 15-mm gypsum plasterboard with 60-minute fall-off time.

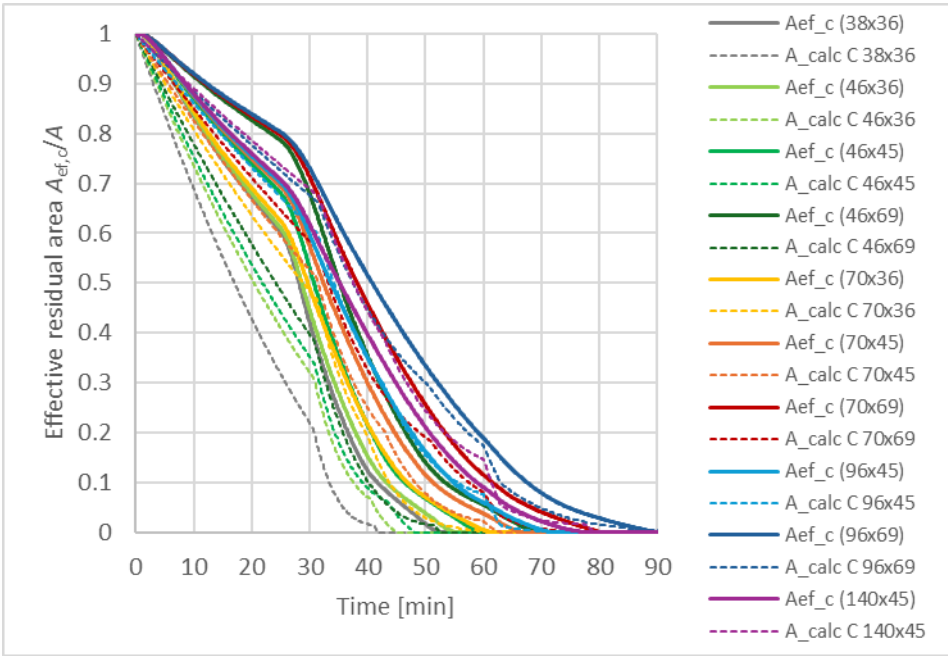


Figure 56. Comparison of simulated and calculated effective areas in compression for assemblies insulated with stone wool and protected by 15-mm gypsum plasterboard with 60-minute fall-off time.

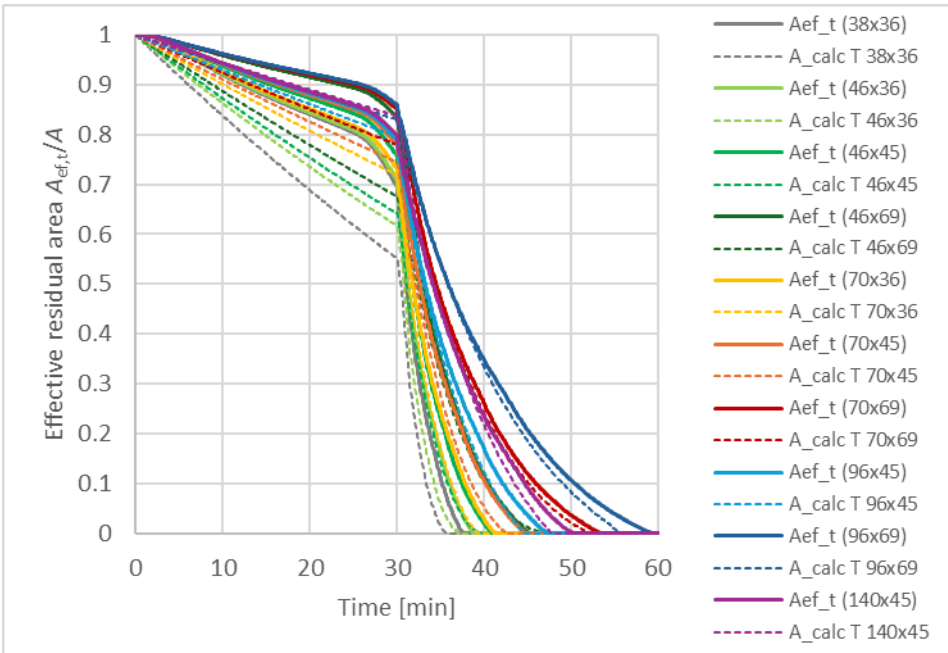


Figure 57. Comparison of simulated and calculated effective areas in tension for assemblies insulated with glass wool and protected by 15-mm gypsum plasterboard with 30-minute fall-off time.

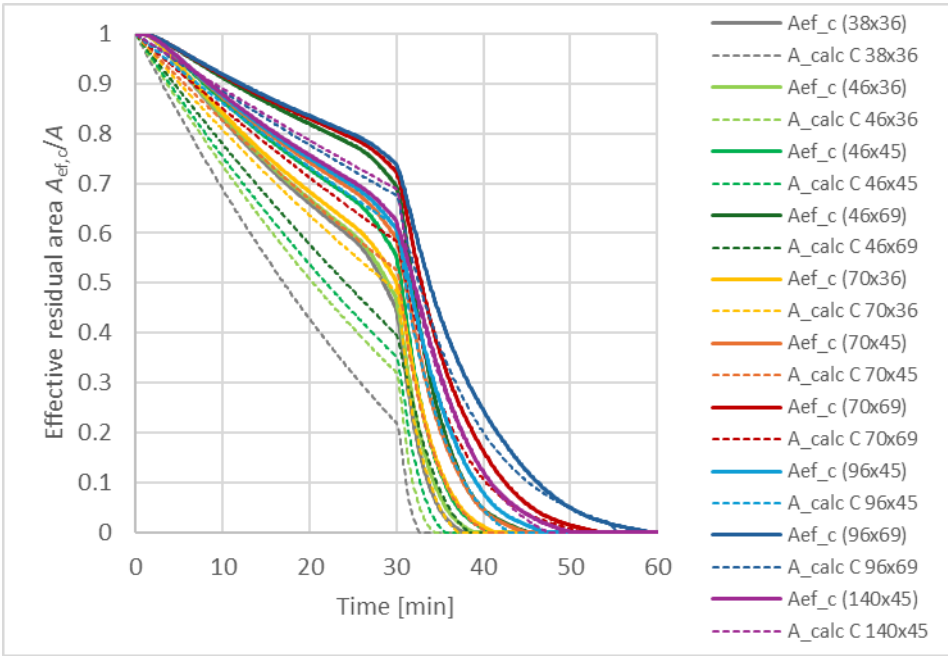


Figure 58. Comparison of simulated and calculated effective areas in compression for assemblies insulated with glass wool and protected by 15-mm gypsum plasterboard with 30-minute fall-off time.

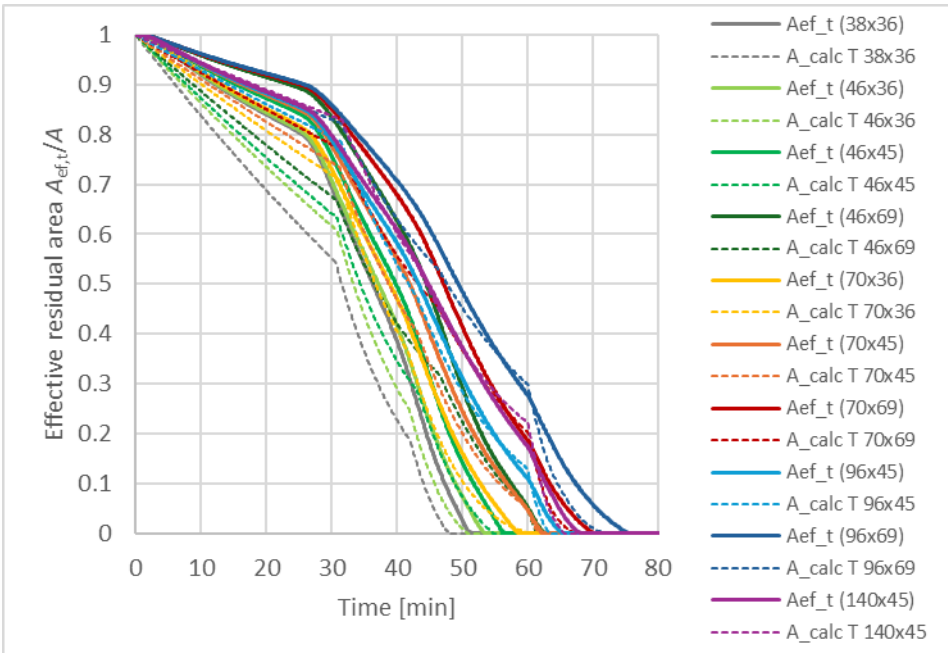


Figure 59. Comparison of simulated and calculated effective areas in tension for assemblies insulated with glass wool and protected by 15-mm gypsum plasterboard with 60-minute fall-off time.

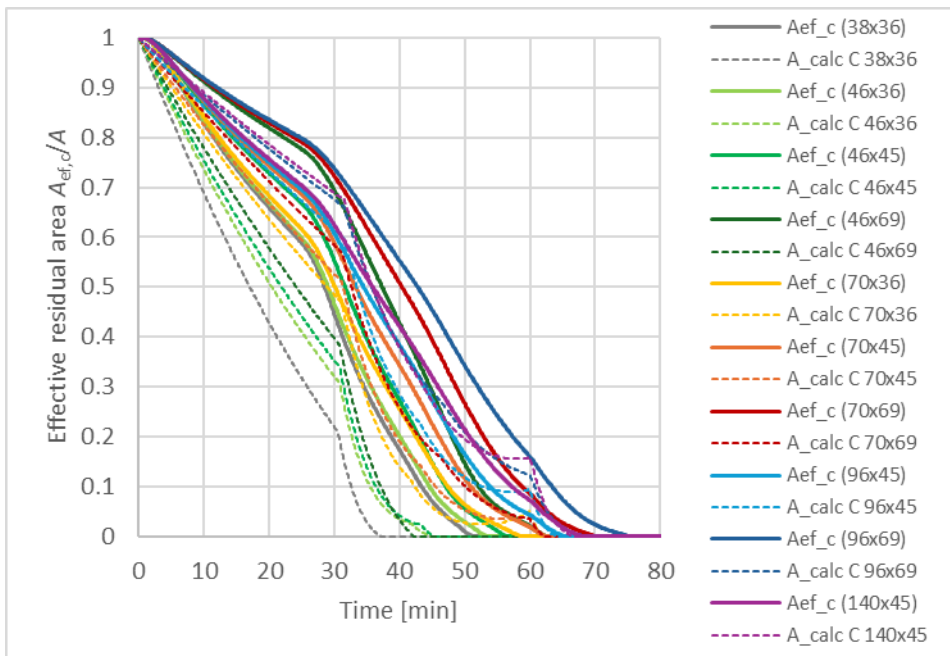


Figure 60. Comparison of simulated and calculated effective areas in compression for assemblies insulated with glass wool and protected by 15-mm gypsum plasterboard with 60-minute fall-off time.

4.5 Compression at normal temperature

The load-bearing capacity of I-joists in compression was investigated by normal temperature compression tests and FE simulations. The effect of cross-section dimensions, bracing and specimen length was investigated. Especially the behaviour of I-joists with one unbraced flange was of interest as this situation is significant in fire design for structural calculations after the failure of claddings (bracings) on the fire side.

4.5.1 Experimental investigation

Numerous ambient temperature compression tests were conducted to investigate the buckling behaviour of I-joists. Two series of compression tests were carried out at RISE in Skelleftea in 2019 and 2020 and series 3 in TalTech in 2024. Test series 3 was conducted and analysed by Grete Kerge (Kerge, 2024) and Tõnis Orav (Orav, 2024) as part of their MSc theses which were part of this doctoral project.

The compression tests were conducted on a variety of configurations as shown in Figure 61. The first parameter which affects the capacity in compression is bracing. In the tests, bracing was used on at least one flange. Additionally, the load placement was varied between the centre of the original cross-section and the braced or unbraced flange. Rotation of the compression element was avoided at the supports in series 1 and 2 by vertical stabilization bars and in series 3 by plywood endplates.

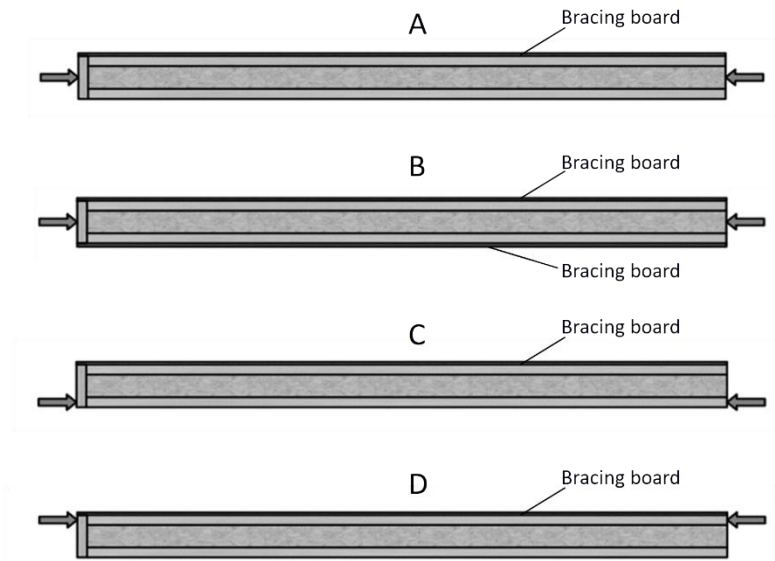


Figure 61. Bracing and load placement in ambient compression tests.

In some tests, the size of the unbraced flange was reduced according to the types shown in Figure 62 to mimic the reduction of the flange in the fire situation.

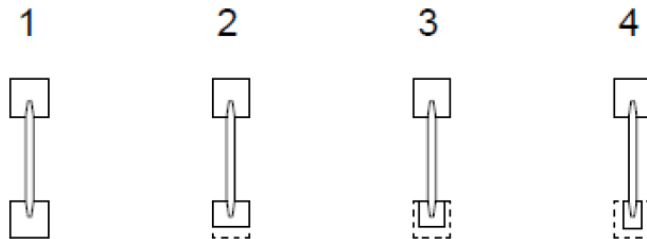


Figure 62. Types of reduced cross-sections of I-joists.

In the following test series, the specimens have been named according to the following convention:

1. Test series number
2. Bracing and load placement
3. Cross-section size
4. Cross-section height in mm
5. Cross-section reduction
6. Other (web material, specimen length)

Table 26 provides the naming key for ambient compression test specimens.

Table 26. Naming key for ambient compression test specimens.

Bracing		Size	$b_f \times h_f$	Reduction	
A	Centric loading, one flange braced	S	47x47	1	Original flange
B	Centric loading, both flanges braced	M	70x47	2	Reduced on fire exposed side
C	Loading on unbraced flange	L	97x47	3	Reduced on exposed and lateral sides
D	Loading on braced flange			4	Equal reduction on the exposed and lateral sides

In test series 1 the effect of the size of flange cross-section on the fire exposed side was studied. Two different cross-section heights of I-joists were tested – 200 mm and 500 mm. Two different flange sizes (width x height) were tested – 47x47 mm and 70x47 mm. Rotational bracing was applied at the supports. The tested specimens had a length of 3 m and flanges of C30 finger-jointed sawn wood.

All test specimens in test series 1 were loaded in the middle of original cross-section height. The non-exposed flange was braced with a wooden board and fasteners with 200 mm distance between them. Compression force and time to failure was recorded.

The cross-section parameters for test series 1 are presented in Table 27.

Table 27. Compression tests at ambient temperature. Series 1.

Specimen number	I-joist $b_f \times h_f$ (mm)	Type of reduced cross-section	Initial cross-section height (mm)	Reduced cross-section height (mm)	Reduced flange size $b_f \times h_f$ (mm)	Number of tests
1-A-S-200-1	47x47	1	200	200	47x47	6
1-A-S-200-2	47x47	2	200	186	47x33	6
1-A-S-200-3	47x47	3	200	186	33x33	6
1-A-S-200-4	47x47	4	200	176	35x23	5
1-A-M-200-1	70x47	1	200	200	70x47	3
1-A-M-200-4	70x47	4	200	176	35x35	3
1-A-S-500-1	47x47	1	500	500	47x47	3
1-A-S-500-4	47x47	4	500	476	35x23	3

In test series 2, the effect of load placement and bracing was studied. All I-joists had 47x47 mm flanges with original dimensions. Three different cross-section heights of I-joists were tested – 200 mm, 300 mm and 400 mm. The test load was placed in the middle of the original cross-section height, on the non-exposed flange or on the exposed flange. The tested specimens had a length of 3 m and flanges of C30 finger-jointed sawn wood.

The non-exposed flange was braced with wooden board and fasteners with 200 mm distance between them. The exposed flange was un-braced or braced similarly to the non-exposed flange. Compression force and time to failure were recorded.

The cross-section parameters for test series 2 are presented in Table 28.

Table 28. Compression tests at ambient temperature. Series 2.

Specimen number	Test setup		Cross-section height	Number of tests
2-A-S-200-1	A	Centric loading, one flange braced	200	3
2-A-S-300-1			300	3
2-A-S-400-1			400	3
2-B-S-200-1	B	Centric loading, both flanges braced	200	3
2-B-S-300-1			300	3
2-B-S-400-1			400	3
2-C-S-200-1	C	Loading on unbraced flange	200	3
2-C-S-300-1			300	3
2-C-S-400-1			400	3
2-D-S-200-1	D	Loading on braced flange	200	3
2-D-S-300-1			300	3
2-D-S-400-1			400	3

In test series 3, the load distribution between flanges, deformations and the effect of different web materials was studied. All cross-sections had an initial height of 400 mm. The cross-section parameters for test series 3 are presented in Table 29.

Table 29. Compression tests at ambient temperature. Series 3.

Specimen number	Type of reduced cross-section	Initial cross-section height (mm)	Reduced flange size $b_f \times h_f$ (mm)	Web material	Length (mm)	Number of tests
3-A-S-400-1(o)	1	400	47x47	OSB	3050	3
3-A-S-400-2(o)	2	400	47x27	OSB	3050	3
3-A-L-400-1(o)	1	400	97x47	OSB	3050	2
3-A-L-400-4(o)	4	400	57x27	OSB	3050	2
3-A-S-400-1(p)	1	400	47x47	PB	3050	2
3-A-S-400-2(p)	2	400	47x27	PB	3050	2
3-A-L-400-1(p)	1	400	97x47	PB	3050	2
3-A-L-400-4(p)	4	400	57x27	PB	3050	2
3-A-S-400-1(o2)	1	400	47x47	OSB	2000	2
3-A-S-400-1(p2)	1	400	47x47	PB	2000	2
3-C-S-400-1(o)	1	400	47x47	OSB	3050	1
3-C-S-400-2(o)	2	400	47x27	OSB	3050	1
3-C-L-400-1(o)	1	400	97x47	OSB	3050	1
3-C-L-400-4(o)	4	400	57x27	OSB	3050	1
3-C-S-400-1(p)	1	400	47x47	PB	3050	1
3-C-S-400-2(p)	2	400	47x27	PB	3050	1
3-C-L-400-1(p)	1	400	97x47	PB	3050	1
3-C-L-400-4(p)	4	400	57x27	PB	3050	2

The test load was placed in the middle of the original cross-section height (variant A in Figure 61) or on the exposed flange (variant C in Figure 61). The non-exposed flange was braced with a wooden board and fasteners with a 200 mm distance between them. The exposed flange was un-braced. A recess was cut into the web at the supports to avoid loading it directly. Figure 63 shows the test specimen in series 3.

Two different web materials were tested – oriented strand board (OSB) and particle board (PB). All flanges were of C30 finger-jointed sawn wood. Four tests were conducted on 2 m joists, all others were 3 m long. Three force sensors and five displacement sensors were applied to various points of the test specimen.

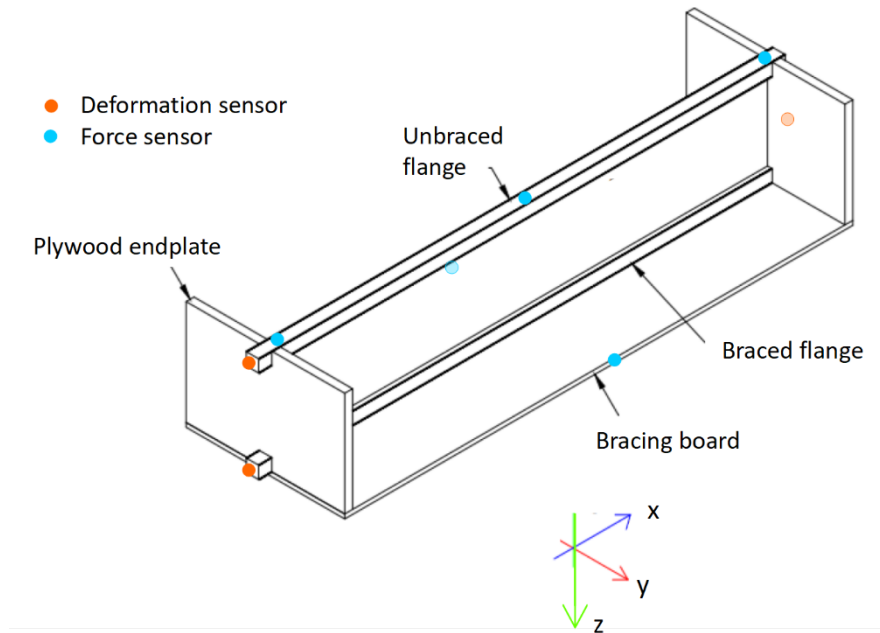


Figure 63. Compression test specimen for test series 3.

4.5.2 Numerical investigation

This section summarises the simplified analysis presented at the 2020 INTER meeting (Publication VI) and the finite element simulations conducted by Grete Kerge as part of her MSc thesis (Kerge, 2024). The two procedures have been combined and the naming and symbols have been unified with the principles of FprEN 1995-1-1:2025 (CEN, 2025a).

The analysis of test series 1 and 2 was presented at the INTER meeting in 2020. The unbraced flange was considered as an axially loaded member with the load distribution calculated as proportional to the areas of the braced and unbraced flanges. The web is considered as a continuous spring support which provides some lateral bracing for the unbraced flange. Additionally, the web can be seen as a cantilever beam with its rigid support being the braced flange. Figure 64 left shows the lateral deflection of the unbraced flange, the right schematic shows the substituted effective length proposed for the calculation model.

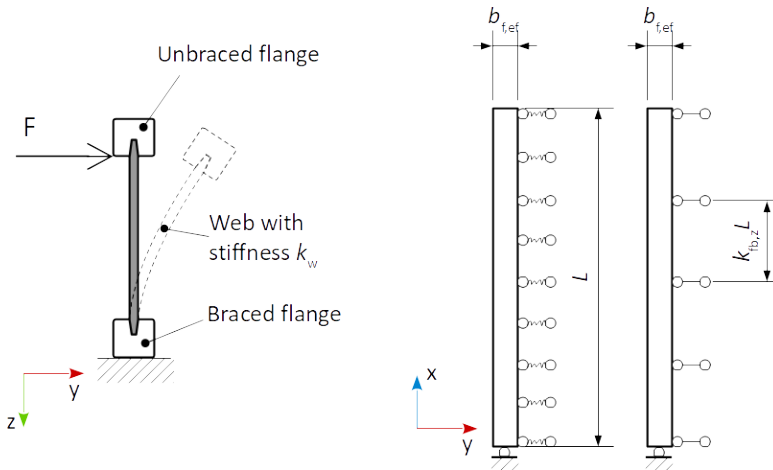


Figure 64. Web acting as a cantilever beam (left), unbraced flange on a continuous spring support (middle), web substituted by the effective length for lateral buckling (right).

The relationship between the lateral stiffness of the web k_w and the load-bearing capacities recorded in the tests was used to derive the factor $k_{bf,z}$ to consider the buckling length based on the stiffness of the web. The factor was back calculated from the load-bearing capacities measured in the tests.

The deflection of a cantilever beam from a force acting on the free end is:

$$\delta = \frac{F \cdot l^3}{3EI} \quad (28)$$

where

- F is the force [N];
- l is the length of the cantilever beam [mm];
- E is modulus of elasticity of the beam [MPa];
- I is the moment of inertia [mm⁴].

Assuming the web acts as a cantilever beam, and receives a unit deformation, it can be calculated at the base of the unbraced flange as:

$$\delta = \frac{F \cdot h_w^3}{3 \cdot E_{w,x} I_{w,x}} = 1 \quad (29)$$

where

- F is the force which causes the unit deformation [N];
- h_w is the cross-section height of the web (between flanges) [mm];
- $E_{w,x} I_{w,x}$ is the bending stiffness of the web about the x-axis with the width of the cross-section taken as the entire height of the column [Nmm²].

The buckling length of the unbraced flange is equal to the total wall height L which should be reduced by considering the stiffness of the web using $k_{bf,z}$. The values of $k_{bf,z}$ were derived from test data by approximating the buckling length required to obtain the load-bearing capacity that was recorded in the tests.

The MSc thesis of Kerge was a continuation of the above procedure with the aim of investigating the stiffness of the web further, based on compression test series 3, and expanding the test results by FE analysis.

The FE analysis used the Dlubal RFEM 6 software to numerically determine the elastic critical load for the unbraced flange. Furthermore, the buckling lengths $l_{eff,z}$ of the unbraced flange were derived from the FE results. The software provides a critical load factor for different buckling modes. Within this analysis, the first buckling mode (half of a sine wave) yielded the lowest value which was in good agreement with the test results.

The full I-joist was modelled as a 3D spatial body. Supports were added to both ends of the stud, and a line support was introduced to the side of the unexposed flange to simulate a fire scenario where only the braced flange retains a reinforcing plate that prevents lateral displacement. Figure 65 shows different views of the modelled joist with the supports.

Hinged supports were placed at both ends as rigid links. These would restrict movement along the y- and z-axes while allowing movement along the x-axis at the top support. Figure 66 shows a detailed view from the software.

A compressive load was applied at the upper support. The lower supports of the stud were fixed hinge supports, and the line support simulating the stiffening plate allowed movement only along the x-axis.

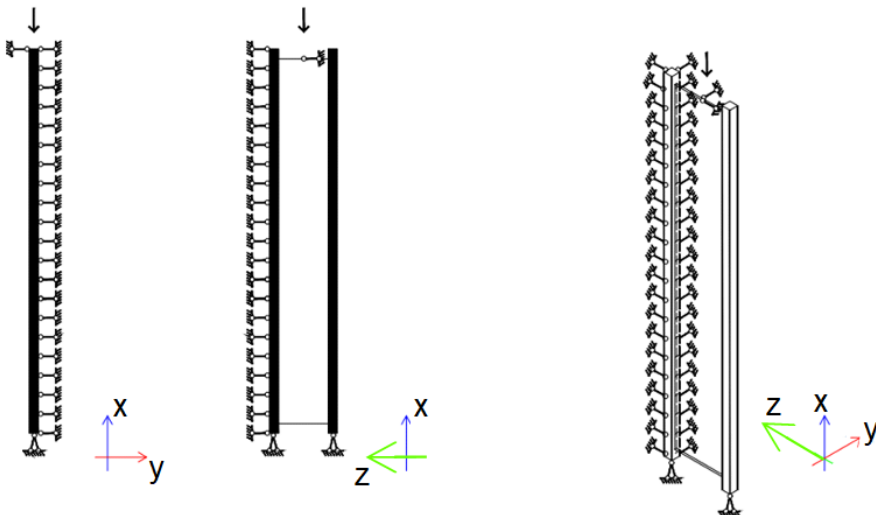


Figure 65. Different views of the FE structural model for compression members.

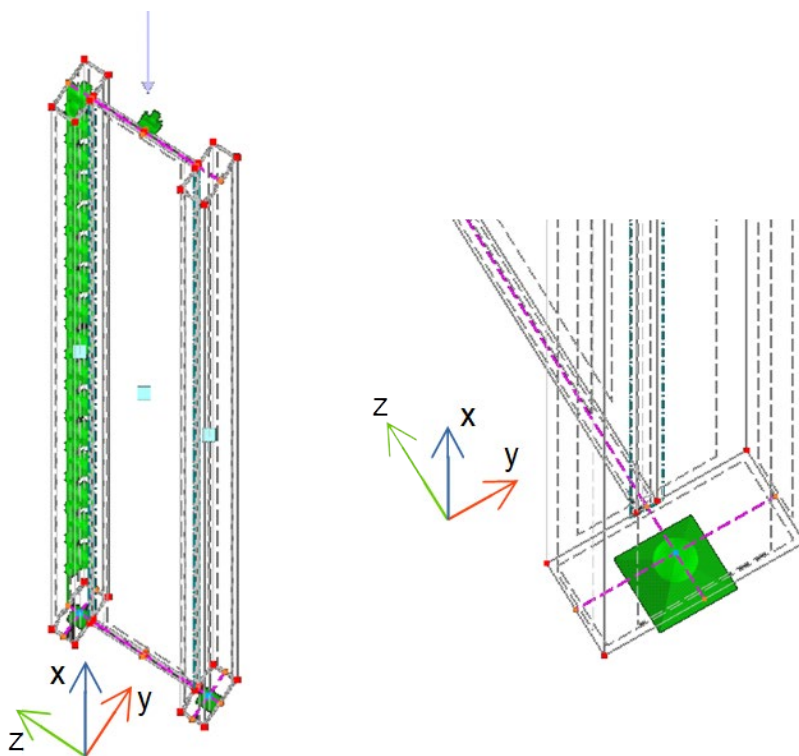


Figure 66. 3D body created in the model (left); rigid links present in the support are depicted (right).

Such a model was created for each cross-section used in the experiments, resulting in a total of eight models (see Table 30). The computational results indicated that variations in wall material did not significantly impact the critical load. Therefore, further calculations were conducted solely with OSB wall material.

Table 30. Tested configurations used in simulations.

Specimen number	Type of reduced cross-section	Initial cross-section height (mm)	Reduced flange size $b_f \times h_f$ (mm)	Web material	Length (mm)
3-A-S-400-1(o)	1	400	47x47	OSB	3050
3-A-S-400-2(o)	2	400	47x27	OSB	3050
3-A-L-400-1(o)	1	400	97x47	OSB	3050
3-A-L-400-4(o)	4	400	57x27	OSB	3050
3-A-S-400-1(p)	1	400	47x47	PB	3050
3-A-S-400-2(p)	2	400	47x27	PB	3050
3-A-L-400-1(p)	1	400	97x47	PB	3050
3-A-L-400-4(p)	4	400	57x27	PB	3050

The 3D model was validated by comparing it with the calculated Euler critical force of a straight member. To model a straight member, the line support was removed from the braced unexposed flange.

In addition to the studs comparable to experimental results, simulations were also performed for new profiles, where both the total cross-section height and the overall height of the stud varied. OSB material properties were used as the web. Table 31 describes the input parameters of the corresponding models.

Table 31. Extended selection of cross-sections modelled in compression.

Flange on the fire side [mm]	Flange on the unexposed side [mm]	Cross-Section height [mm]	Column height [mm]
47x97	47x97	200	3000
47x97	47x97	300	3000
47x67	47x97	200	3000
47x67	47x97	300	3000
47x67	47x97	400	3000
47x47	47x97	200	3000
47x47	47x97	300	3000
47x47	47x97	400	3000
47x97	47x97	200	2500
47x97	47x97	300	2500
47x97	47x97	400	2500
47x67	47x97	200	2500
47x67	47x97	300	2500
47x67	47x97	400	2500
47x47	47x97	200	2500
47x47	47x97	300	2500
47x47	47x97	400	2500
47x97	47x97	200	3500
47x97	47x97	300	3500
47x97	47x97	400	3500
47x67	47x97	200	3500
47x67	47x97	300	3500
47x67	47x97	400	3500
47x47	47x97	200	3500
47x47	47x97	300	3500
47x47	47x97	400	3500

Using FEM software, the critical loads corresponding to different cross-sections were obtained to identify the relationship between the stiffness of the web and the buckling capacity of the I-shaped stud in fire conditions. The elastic critical load for an I-profile post was determined, which in turn allowed for the calculation of the Euler critical load of the unbraced flange. From the critical load value, the buckling length of the unbraced flange was derived.

The web acts as a cantilever beam bending about the x-axis with its support being the braced flange. Therefore, the stiffness of the unit length of the web can be expressed as:

$$k_w = \frac{3 E_w b_w^3}{12 h_w^3} \quad (30)$$

where

k_w is the stiffness of the unit length of the web [MPa];
 E_w is the modulus of elasticity of the web material [MPa];
 b_w is the thickness of the web [mm];
 h_w is the height of the web between the flanges [mm].

According to Annex B of FprEN 1995-1-1:2025 (CEN, 2025a) and described above in Chapter 1.3, the relative stiffness of the smeared support K_{rel} is:

$$K_{rel} = \frac{k_w \cdot l^2}{N_{crit,0}} \quad (31)$$

Therefore, substituting the values for I-shaped members in the fire situation is:

$$K_{rel} = \frac{k_w \cdot l^2}{N_{crit,0}} = \frac{3 \cdot E_w \cdot b_{w,ef}^3 \cdot l^4}{\pi^2 \cdot h_w^3 \cdot E_f \cdot h_{f,ef} \cdot b_{f,ef}^3} \quad (32)$$

where

E_w is the modulus of elasticity of the web material [MPa];
 $b_{w,ef}$ is the effective thickness of the web [mm];
 h_w is the height of the web (distance between the flanges) [mm];
 E_f is the modulus of elasticity of the flange material [MPa];
 $h_{f,ef}$ is the effective height of the unbraced flange [mm];
 $b_{f,ef}$ is the effective width of the unbraced flange [mm].

Models created using FEM (Finite Element Method) software allow for a more precise analysis of the effect of the web on the load-bearing capacity of the unbraced flange. Using the critical load factor obtained from the model, it is possible to determine the buckling length of the unbraced fire exposed flange.

For symmetrical cross-sections, the load is evenly distributed between the flanges, whereas in asymmetrical cases, the load must be distributed according to the ratio of compressive stiffness (cross-sectional areas) of the flanges. By knowing the applied load, it can be multiplied by the critical load factor from the model to determine the corresponding Euler critical load for each unbraced flange. From the Euler critical load formula, the effective buckling length for lateral buckling about the z-axis obtained from the FE model can be expressed as:

$$l_{z,ef,m} = \sqrt{\frac{\pi^2 \cdot E \cdot I}{N_{crit}}} \quad (33)$$

The effective buckling lengths from the model are used as the basis for developing the buckling length reduction factor by plotting the ratio of the effective buckling length to the total height of the column against the relative stiffness of the web.

4.5.3 Experimental results

The results and discussion of the ambient test results obtained from test series 1-3 are presented below.

In test series 1 the effect of the cross-section height was investigated. The compression load capacities measured at rupture in the tests are shown in Table 32 and Figure 67.

Table 32. Results of series 1.

Specimen number	Maximum load [kN]						Average load [kN]
1-A-S-200-1	74.1	102.2	97.8	78.5	89.7	97.7	90.0
1-A-S-200-2	75.7	77.5	91.8	75.5	90.1	73.0	80.6
1-A-S-200-3	60.2	65.4	69.5	52.2	73.1	75.7	66.0
1-A-S-200-4	49.5	50.2	58.8	57.7	57.8		54.8
1-A-M-200-1	192	154.6	137.5				161.4
1-A-M-200-4	66.5	82.6	90.8				80.0
1-A-S-500-1	27.3	55.1	56.6				46.3
1-A-S-500-4	33.5	30.8	31.0				31.8

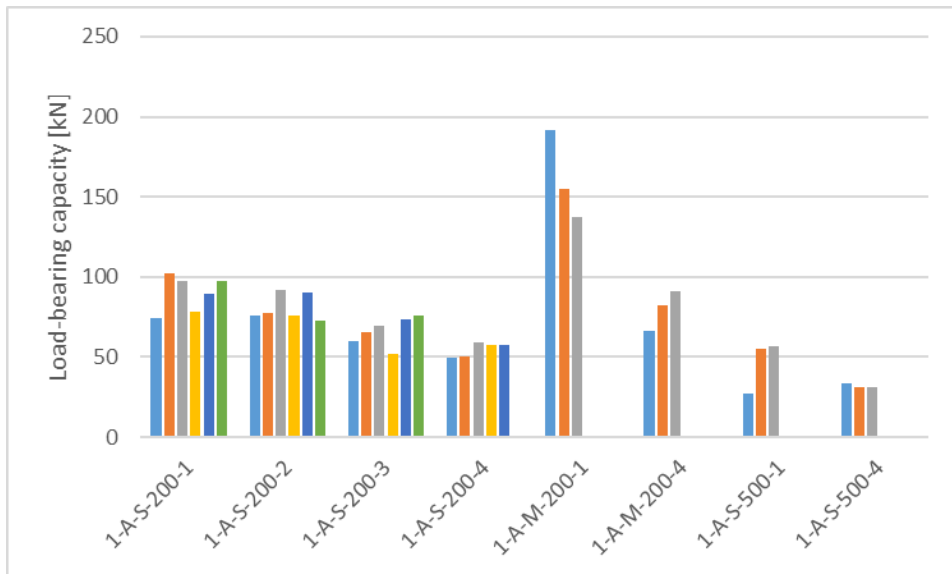


Figure 67. Results of compression test series 1.

From the results of test series 1 the load-bearing capacities of taller specimens are significantly lower than those of smaller ones. This is caused by the lower stiffness of the web of the higher cross-section which allows for buckling under lower load. The load-bearing capacity of the non-braced flange is crucial for the load-bearing capacity of the wall compression member.

In test series 2 the capacities under different load placement were studied. Differences were observed under load placed centrally or one of the flanges. The load-bearing capacities measured in test series 2 are shown in Table 33 and Figure 68.

Table 33. Results of series 2.

Specimen number	Maximum load [kN]			Average load [kN]
2-A-S-200-1	69.7	78.4	78.8	75.6
2-A-S-300-1	44.5	46.9	48.1	46.5
2-A-S-400-1	38.5	39.8	42.5	40.3
2-B-S-200-1	80.9	95.8	92.7	89.8
2-B-S-300-1	90.6	72.7	97.8	87.0
2-B-S-400-1	110.5	92.6	104.2	102.4
2-C-S-200-1	51.1	43.6	39.9	44.9
2-C-S-300-1	31.6	31.4	27.2	30.1
2-C-S-400-1	27.9	25.8	24.1	25.9
2-D-S-200-1	73.9	76.6	69	73.2
2-D-S-300-1	54.1	70.1	68.6	64.3
2-D-S-400-1	67.4	65.7	67.6	66.9

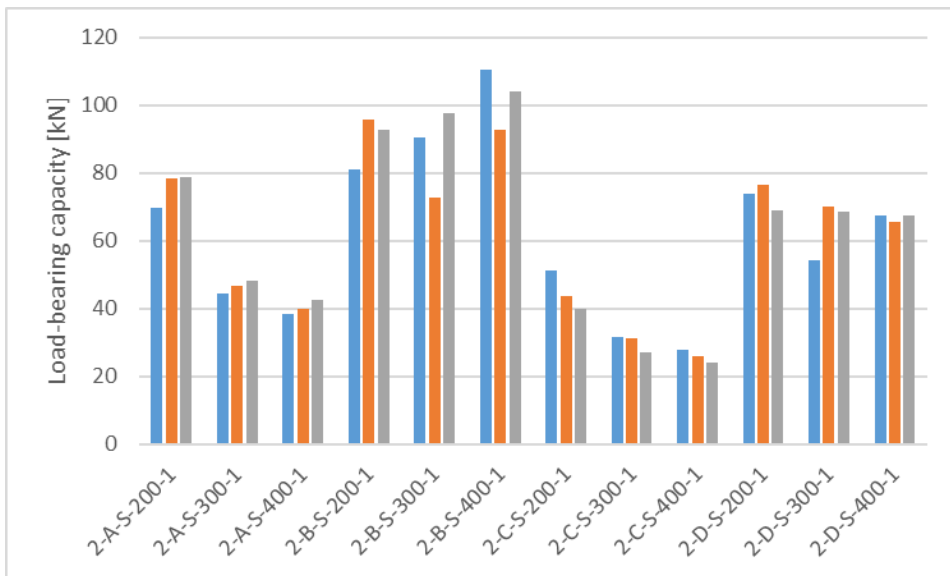


Figure 68. Results of compression test series 2.

Test results of test series 2 show that the load-bearing capacity of I-joists with a 200-mm cross-section height was reduced by 16% when one flange was released. I-joists with a cross-section height of 300 mm and 400 mm lost 47% and 60% of the initial capacity, respectively.

Rupture of the test specimens occurred always at the location of a knot in the unbraced flange at approximately 2 to 2.3 m from the support. Buckling occurred in wall plane in all tests in series 1 and 2.

Different web materials (OSB and particleboard) were investigated in test series 3, denoted by (o) and (p), respectively.

Table 34. Results of series 3.

Specimen number	Maximum load [kN]			Average load [kN]
3-A-S-400-1(o)	56.13	68.72	62	62.3
3-A-S-400-2(o)	44.58	46.34	42.98	44.6
3-A-L-400-1(o)	187.68	202.78		195.2
3-A-L-400-4(o)	62.89	62.26		62.6
3-A-S-400-1(p)	67.63	69.55		68.6
3-A-S-400-2(p)	45.72	46.15		45.9
3-A-L-400-1(p)	175.47	166.87		171.2
3-A-L-400-4(p)	57.93	61.48		59.7
3-A-S-400-1(o2)	86.76			86.8
3-A-S-400-1(p2)	68.19			68.2
3-C-S-400-1(o)	32.11			32.1
3-C-S-400-2(o)	23.39			23.4
3-C-L-400-1(o)	153.25			153.3
3-C-L-400-4(o)	31.39			31.4
3-C-S-400-1(p)	29.99			30.0
3-C-S-400-2(p)	26.73			26.7
3-C-L-400-1(p)	138.18			138.2
3-C-L-400-4(p)	36.53	28.49		32.5

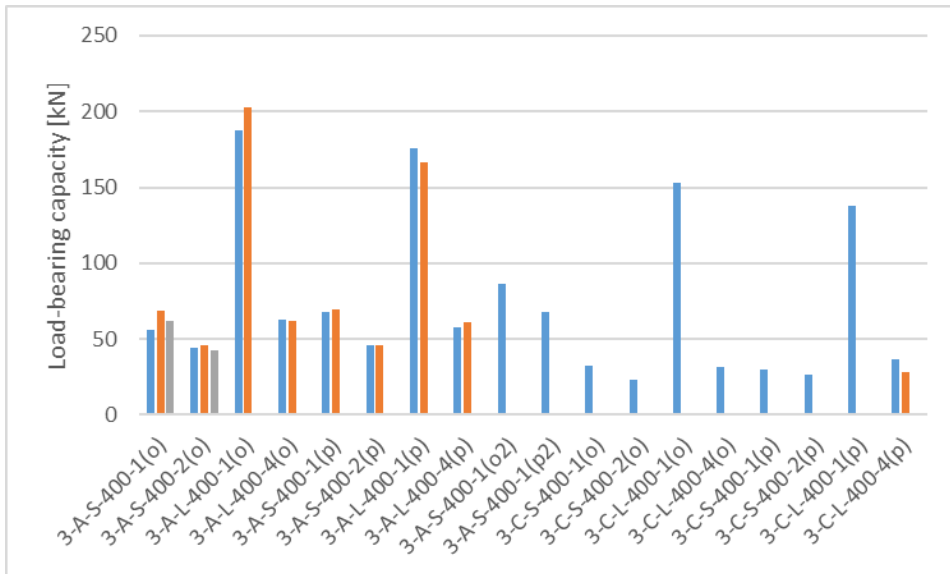


Figure 69. Results of compression test series 3.

The comparison of average maximum loads (load-bearing capacities in compression) for centrally loaded and full cross-sections are shown in Figure 70. Section depth was varied while keeping the flange dimensions constant. Larger depths (300; 400 and 500 mm) show a lower compression capacity due to increased slenderness. Column lengths were varied for some cross-section sizes. The capacity is greater for shorter

columns (2m). Flange widths are compared for section depths of 200- and 400-mm. Wider cross-sections (M and L) show a greater compression capacity. Different bracing is compared for cross-section depths of 200-, 300- and 400-mm. For higher depths, bracing on both sides (B) showed significantly higher compression capacities.

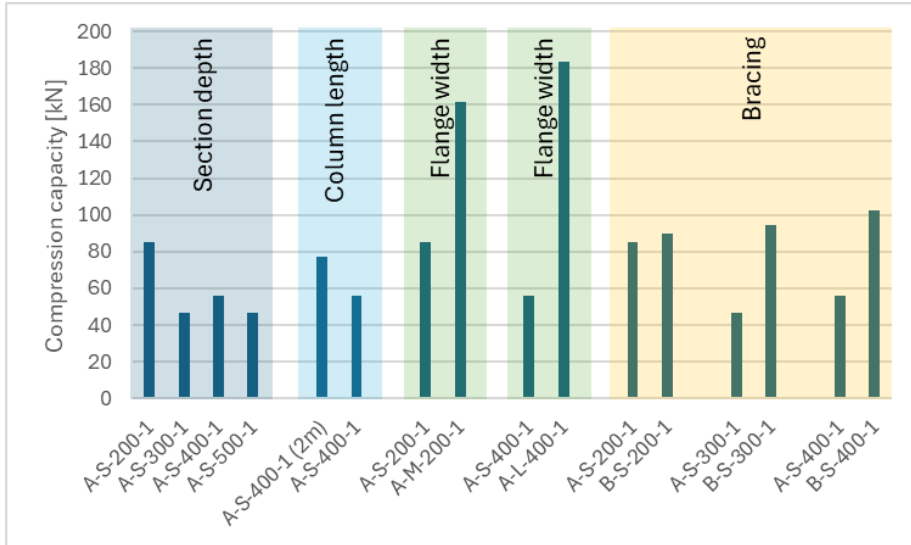


Figure 70. Average compression capacities in centrally loaded tests.

The comparison of load-bearing capacities under centric loading with different reduced flanges is shown in Figure 71.

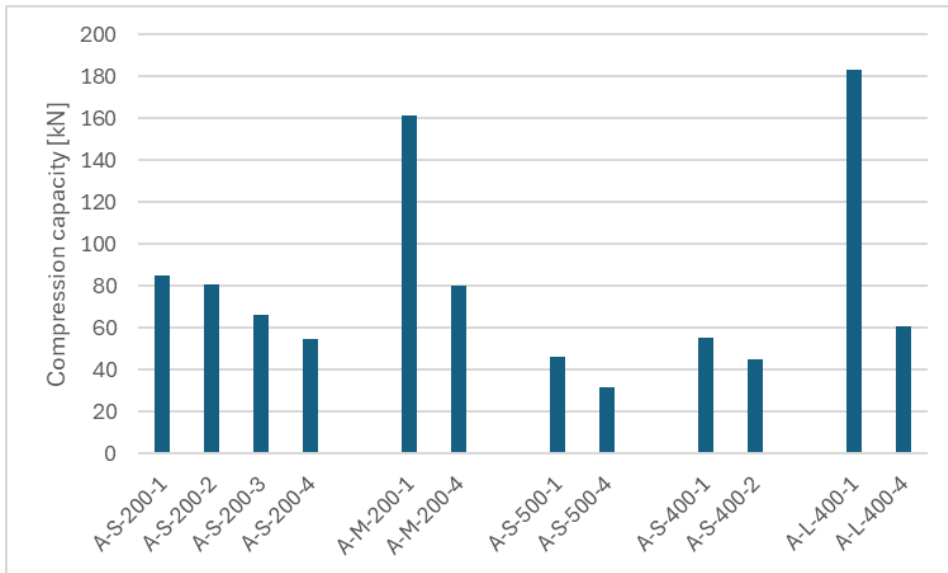


Figure 71. Comparison of full and reduced flanges under centric loading.

The comparison of the effect of different load placements on the load-bearing capacity is shown in Figure 72.

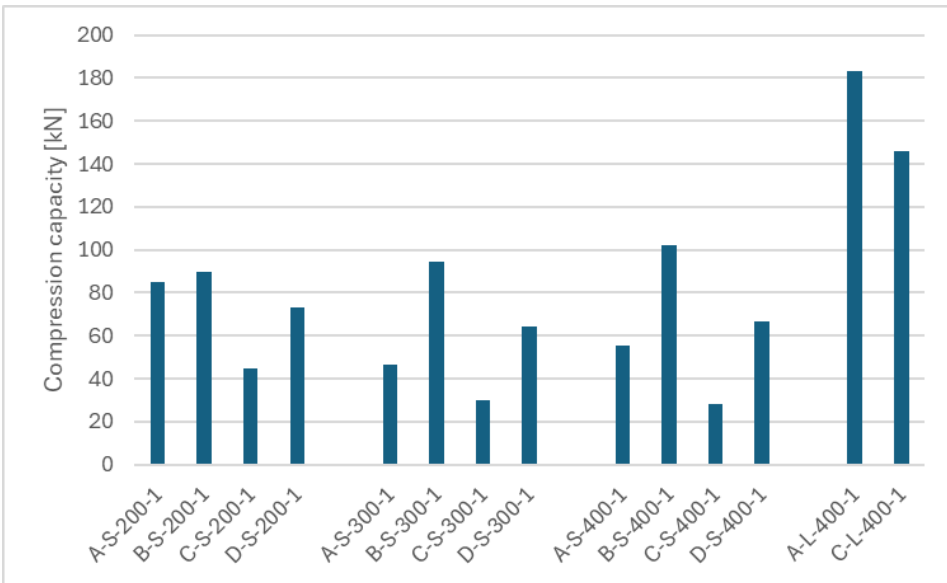


Figure 72. Comparison of different load placements.

The effect of reduced flange size on the load-bearing capacity under eccentric loading is shown in Figure 73.

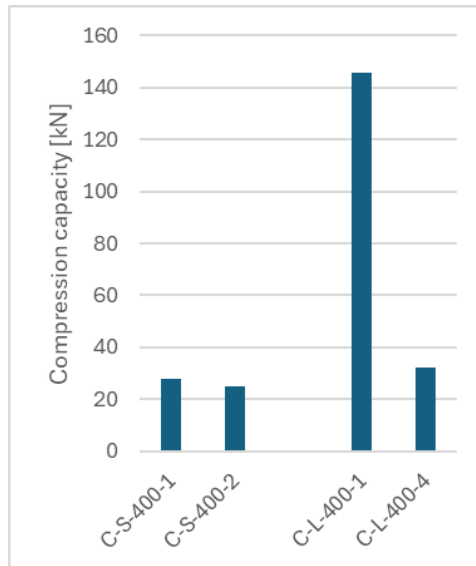


Figure 73. Comparison of reduced flanges in eccentric loading.

The compression tests showed that higher cross-section depths and longer columns have a lower compression capacity due to reduced stability. Wider flanges showed higher capacity, as did the sections which were braced on both sides (variant B in Figure 61). The reduction of the flange also reduced the load-bearing capacity. The lowest compression capacities were seen in the case where the load is acting directly on the unbraced flange.

4.5.4 Results of numerical investigations

The results of the validation of the FE simulations comparing the calculated Euler critical load and straight (without the line support) models are presented in Figure 74. The obtained results align, and it can be assumed that the computational model is sufficiently accurate for further simulations.

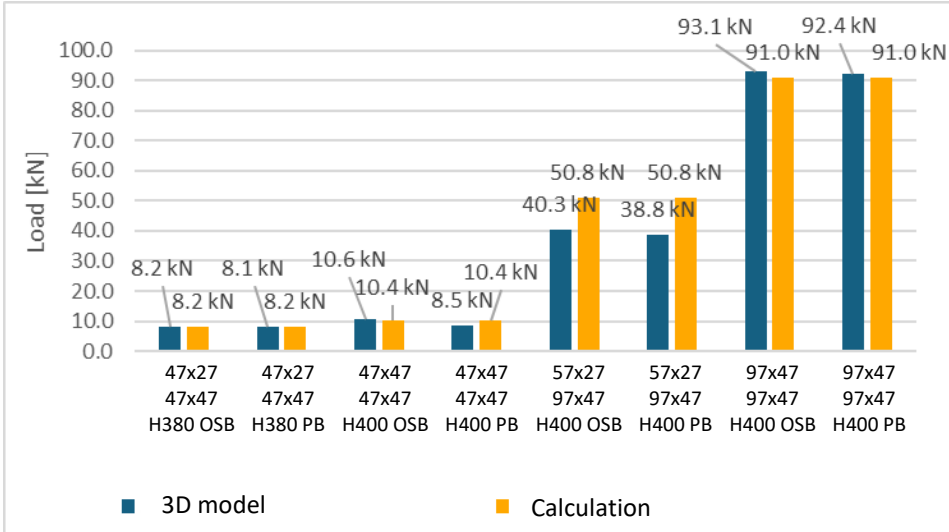


Figure 74. Validation of FE compression models.

Figure 74 shows that, for the most part, the results obtained from the model coincide with the Euler critical load calculation results. However, a noticeable difference arises in cases where the flange profiles on the exposed and unexposed side have the greatest variation.

By multiplying the critical load factor corresponding to the first buckling mode with the applied compressive force, the elastic critical load of the stud can be determined. These results are presented in Table 35 and Figure 75.

Table 35. Load-bearing capacity obtained from tests and Euler critical load values from the model.

Flange on the fire side $b_f \times h_f$ [mm]	Unexposed flange $h_f \times b_f$ [mm]	Cross-Section height [mm]	Column height [mm]	Web material	Load-bearing capacity [kN]		
					Model	Test results	
						Test 1	Test 2
47x27	47x47	380	3050	OSB	38.9	43.0	44.6
47x47	47x47	400	3050	OSB	49.9	56.1	62.0
57x27	97x47	380	3050	OSB	110.9	62.3	62.9
97x47	97x47	400	3050	OSB	291.3	187.7	202.8
47x27	47x47	380	3050	PB	38.3	46.2	45.7
47x47	47x47	400	3050	PB	50.9	67.6	69.6
57x27	97x47	380	3050	PB	105.0	61.5	57.5
97x47	97x47	400	3050	PB	283.3	166.9	175.5

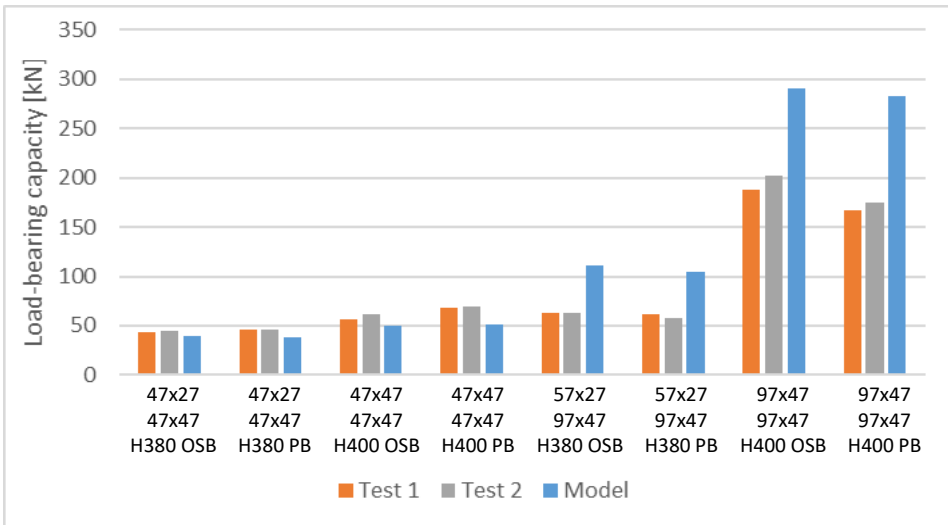


Figure 75. Graphical comparison of load-bearing capacity from tests and elastic critical load from the model.

Figure 75 shows good agreement between the elastic critical load obtained from the model and the load-bearing capacity determined from the experiments for smaller cross-sections for which the model is slightly conservative. However, for larger cross-sections, the model results are significantly higher than the test results. This discrepancy can be attributed to the excessive rigidity of the modelled bracing which adds to the stiffness of the braced flange. Therefore, the braced flange is able to take more load off the unbraced flange. For the bigger cross-sections, the flanges are stiffer in the weak direction (flanges are wider) and yield high capacities in the idealised FE model.

By simplifying the unbraced flange as a compressed member, the dependency of its Euler critical load on slenderness can be analysed. Smaller cross-sections have greater slenderness, and the Euler critical force for more slender members is closer to the actual load-bearing capacity because buckling occurs within the elastic deformation range. The Euler critical load is derived based on the validity of Hooke's law. For larger cross-sections, the loss of load-bearing capacity occurs partially within the plastic deformation range, and the Euler critical load yields a higher result than the actual load-bearing capacity.

The elastic critical loads obtained from the model and the calculated effective buckling lengths are presented in Table 36.

Table 36. Load-bearing capacities and effective buckling lengths obtained from the model for all configurations, tested configurations shown in italics.

Flange on the fire side $b_f \times h_f$ [mm]	Unexposed flange $h_f \times b_f$ [mm]	Cross-Section height [mm]	Column height [mm]	Web material	Elastic critical load [kN]	l_{eff} from the model [mm]
<i>47x27</i>	<i>47x47</i>	<i>380</i>	<i>3050</i>	<i>OSB</i>	<i>38.9</i>	<i>1397</i>
<i>47x47</i>	<i>47x47</i>	<i>400</i>	<i>3050</i>	<i>OSB</i>	<i>49.9</i>	<i>1385</i>
<i>57x27</i>	<i>97x47</i>	<i>380</i>	<i>3050</i>	<i>OSB</i>	<i>110.9</i>	<i>1286</i>
<i>97x47</i>	<i>97x47</i>	<i>400</i>	<i>3050</i>	<i>OSB</i>	<i>291.3</i>	<i>1696</i>
97x47	97x47	200	3000	OSB	416.6	1420
97x47	97x47	300	3000	OSB	302.9	1665
67x47	97x47	200	3000	OSB	273.7	940
67x47	97x47	300	3000	OSB	177.0	1233
67x47	97x47	400	3000	OSB	150.1	1374
47x47	97x47	200	3000	OSB	196.9	1151
47x47	97x47	300	3000	OSB	106.1	1409
47x47	97x47	400	3000	OSB	80.0	1509
97x97	97x47	200	2500	OSB	488.6	1311
97x97	97x47	300	2500	OSB	404.9	1439
97x97	97x47	400	2500	OSB	385.5	1475
67x47	97x47	200	2500	OSB	306.6	1081
67x47	97x47	300	2500	OSB	215.1	1268
67x47	97x47	400	2500	OSB	190.6	1327
47x47	97x47	200	2500	OSB	209.8	898
47x47	97x47	300	2500	OSB	121.3	1133
47x47	97x47	400	2500	OSB	96.9	1224
97x47	97x47	200	3500	OSB	367.6	1512
97x47	97x47	300	3500	OSB	267.0	1772
97x47	97x47	400	3500	OSB	240.1	1868
67x47	97x47	200	3500	OSB	257.8	930
67x47	97x47	300	3500	OSB	152.3	1525
67x47	97x47	400	3500	OSB	123.6	1671
47x47	97x47	200	3500	OSB	189.0	966
47x47	97x47	300	3500	OSB	97.0	1302
47x47	97x47	400	3500	OSB	69.7	1491

4.5.5 Analysis of numerical and experimental results

The ratios of the effective buckling length and the column height are plotted against the relative stiffnesses in Figure 76. The regression equation represents the factor accounting for the influence of boundary conditions, for lateral buckling about the z-axis depending on the relative stiffness of the web.

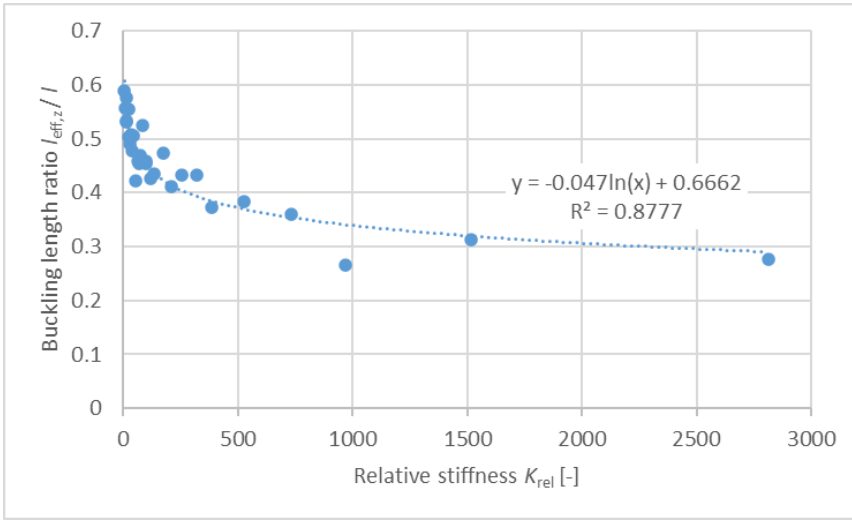


Figure 76. Effective buckling length vs relative stiffness.

Using the symbols from FprEN 1995-1-1:2025 (CEN, 2025a), the expression for the buckling length factor is:

$$k_{fb,z} = 0.67 - 0.05 \cdot \ln K_{rel} \quad (34)$$

where

$k_{fb,z}$ is the factor for lateral buckling about the z-axis [-];

K_{rel} is the relative stiffness of the web [-].

The calculated and tested load-bearing capacities are compared in Figure 77.

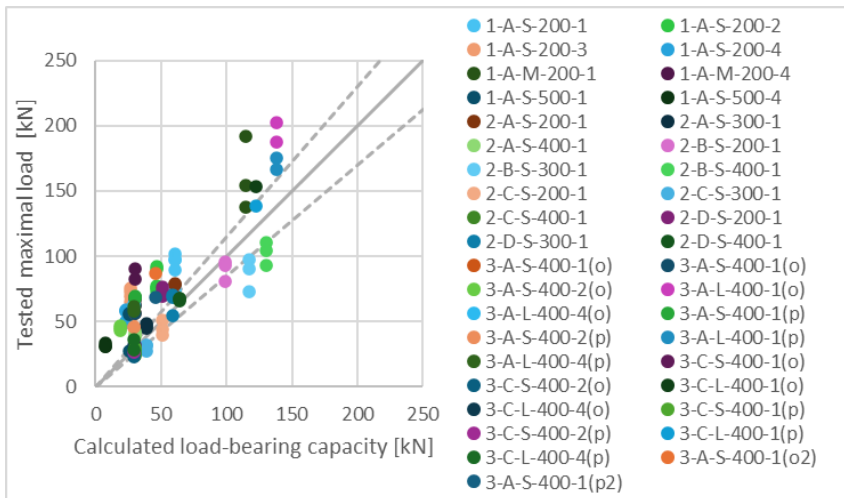


Figure 77. Calculated and tested compression capacities from ambient tests. Dashed lines represent $\pm 15\%$ difference.

The results of the ambient compression tests and the calculated load-bearing capacities considering buckling are comparable. The calculations are mainly on the conservative side, especially in the cases where the bracing was only on one side.

5 Design of wooden I-joists in fire

This chapter presents the design model for wooden I-joists exposed to the standard fire in accordance with the principles of the Effective Cross-Section Method. First, the charring model is presented with equations for the parameters. The load-bearing calculations are provided in the following three sections. The final subchapter gives validation for the model parameters that were developed.

5.1 Charring

Char depth should be calculated separately for the Exposed side and the Lateral sides of the fire exposed flange according to Figure 78. The following has been published in Publication II of the thesis.

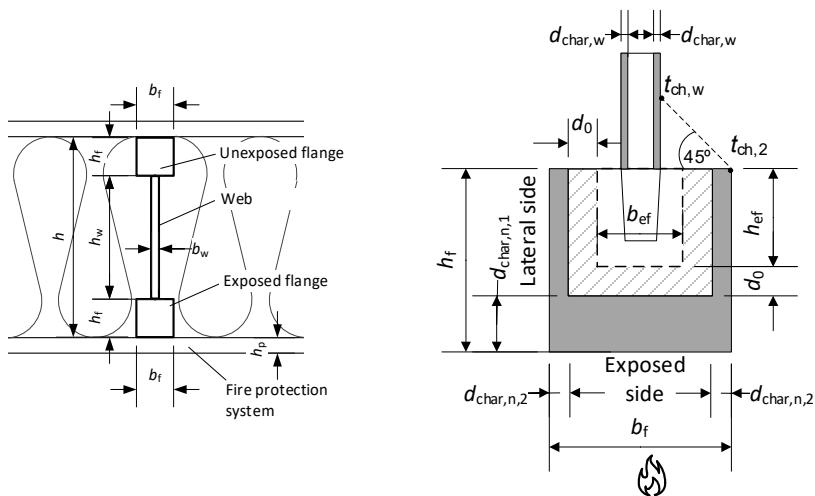
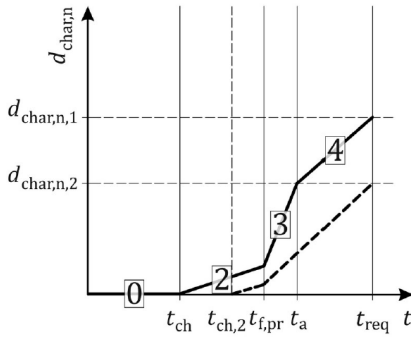
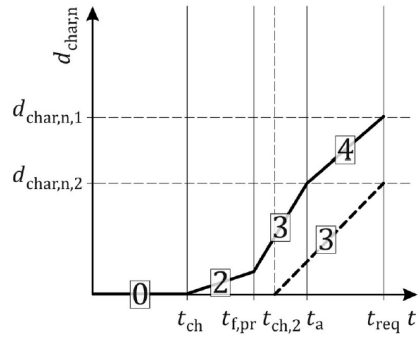


Figure 78. I-joist. (a) Naming of the parts of an I-joist; (b) Principles of the new design model.

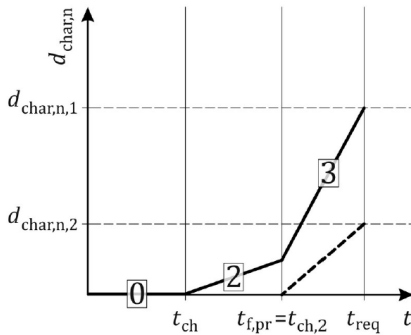
Charring on the fire exposed side of the exposed flange may exhibit 4 charring phases depending on the combination of materials used in the assembly. The combined section and conversion factor $k_{s,n}$ takes into account the effect of the cross-section size to the notional charring rate and is the same for all charring phases. The width of the flange influences the factor $k_{s,n,1}$ for charring from the Exposed side (Figure 78b) and the height (depth) of the flange influences the factor $k_{s,n,2}$ for charring from the Lateral side (Figure 78b). The properties of the fire protection system have the greatest influence on charring behaviour. Necessary parameters describing the protection system are the start time of charring, the failure time and the protection coefficient k_2 (to consider the slowed charring rate behind protection). After the failure of fire protection system, the increased charring on the Exposed side (see Figure 78b) will be considered by the charring coefficient $k_{3,1}$ until the consolidation time t_a and by charring coefficient k_4 after that. See Figure 79 for the depiction of the charring phases.



a) Charring phases with cavity insulations PL1 and PL2 when charring on the lateral side occurs before the failure of fire protection system; $t_{ch,2} \leq t_{f,pr}$



b) Charring phases with cavity insulations PL1 and PL2 when charring on the lateral side occurs after the failure of fire protection system; $t_{ch,2} > t_{f,pr}$



c) Charring phases for void cavities

Figure 79. Design model for I-shaped timber members of timber frame assemblies according to FprEN 1995-1-2:2025 (CEN, 2025b).

The charring rate of the lateral sides of the flange is mostly dependent on the cavity insulation material. The start time of charring on the lateral side $t_{ch,2}$ can occur during Phase 2, Phase 3 or Phase 4 depending on the cladding and the cavity insulation. After time $t_{ch,2}$ the flange width will be reduced, taking into account the factor k_2 for charring occurring before the fall-off of the fire protection system and factor $k_{3,2}$ for charring after the fall-off. The consolidated charring phase has not been observed for lateral charring, therefore, after the fall-off of protection, charring is considered to occur at a constant rate until the end of the fire.

The general expressions to calculate the notional char depth of the flanges of an I-joist are shown in equations (35) to (37).

The notional char depth on the fire exposed side of the exposed flange $d_{char,n,1}$ is calculated as:

$$d_{char,n,1} = \beta_0 \cdot k_{s,n,1} \cdot k_2 \cdot (t_f - t_{ch}) + \beta_0 \cdot k_{s,n,1} \cdot k_{3,1} \cdot (t_a - t_f) + \beta_0 \cdot k_{s,n,1} \cdot k_4 \cdot (t - t_a) \quad (35)$$

where

β_0 is the basic design charring rate of the flange material [mm/min];

k_2 is the protection factor of the fire protection system [-];

$k_{s,n,1}$	is the combined section and conversion factor for the fire exposed side [-];
t_{ch}	is the start time of charring behind the fire protection system [min];
t_f	is the fall-off time of the fire protection system [min];
t_a	is the consolidation time [min];
$k_{3,1}$	is the post-protection factor for the fire-exposed side [-];
k_4	is the consolidation factor [-];
t	is the fire resistance time [min].

The start time of lateral charring is considered as the time when 300 °C is reached at the corner of the fire exposed flange (see $t_{ch,2}$ in Figure 78b). It is recommended to be calculated using the Separating Function Method (CEN, 2025b), formerly known as the Improved Component Additive Method (Mäger et al., 2017, 2018, 2019; Östman et al., 2010).

If the start time of charring on the lateral sides of the flange ($t_{ch,2}$) is before the fall-off of the fire protection system, then the notional charring depth on the lateral sides $d_{char,n,2}$ occurs in two phases, see equation (36).

$$d_{char,n,2} = \beta_0 \cdot k_{s,n,2} \cdot k_2 \cdot (t_f - t_{ch,2}) + \beta_0 \cdot k_{s,n,2} \cdot k_{3,2} \cdot (t - t_f) \quad (36)$$

where

$k_{s,n,2}$	is the combined section and conversion factor for the lateral side [-];
$k_{3,2}$	is the post-protection factor for the lateral side [-];
$t_{ch,2}$	is the start time of lateral charring [min].

If charring on the lateral sides occurs only in post-protection phase (after the fall-off of the fire protection system), then notional char depth on the lateral sides of the flange may be calculated as:

$$d_{char,n,2} = \beta_0 \cdot k_{s,n,2} \cdot k_{3,2} \cdot (t - t_{ch,2}) \quad (37)$$

The char depth of the web is considered from time $t_{ch,w}$ and calculated according to equation (38). The start time of charring of the web is considered as the time when 300 °C is reached on the web (see $t_{ch,w}$ in Figure 78b). It is recommended to be calculated using the Separating Function Method (CEN, 2025b), (Mäger et al., 2017, 2018, 2019; Östman et al., 2010).

$$d_{char,w} = \beta_{n,w} \cdot k_3 \cdot (t - t_{ch,w}) \quad (38)$$

where

$\beta_{n,w}$	is the notional design charring rate of the web material [mm/min];
k_3	is the post-protection factor for the web (equal to 2) [-];
$t_{ch,w}$	is the start time of charring of the web [min].

The values for the coefficients shown in bold type in the above expressions are given in Table 37.

Table 37. Charring calculation model parameters derived from thermal simulations.

Coefficient	PL1 (Stone wool)	PL2 (Glass wool)
Combined section and conversion coefficient for the exposed side $k_{s,n,1}$	$7.6 \cdot b_f^{-0.35}$	
Combined section and conversion coefficient for the lateral side $k_{s,n,2}$	$220 \cdot h_f^{-1.2}$	
Consolidation time t_a	$1.05 \cdot t_f$	
Post-protection coefficient for the exposed side $k_{3,1}$	$9 - 0,093 \cdot t_f$	$5.5 - 0,015 \cdot t_f$
Post-protection coefficient for the lateral side $k_{3,2}$	$0.024 \cdot \max \left\{ \frac{t_{ch,2}}{t_f} - 0.41 \right\}$	$0,043 \cdot \max \left\{ \frac{t_{ch,2}}{t_f} - 0.068 \right\}$
Consolidation coefficient for the exposed side k_4	$1.3 - 0.0018 \cdot t_a$	$0.0088 \cdot t_a + 2.3$

5.2 Zero-strength layer

The depth of the zero-strength layer should be calculated based on the load scenario and the type of cavity insulation. The zero-strength layer depth develops throughout the full fire exposure. To calculate the load-bearing capacity of an I-shaped member, the effective flange dimensions are calculated as:

$$h_{f,ef} = h_f - d_{char,n,1} - d_0 \quad (39)$$

and

$$b_{f,ef} = b_f - 2 \cdot (d_{char,n,2} + d_0) \quad (40)$$

where

- $h_{f,ef}$ is the effective flange depth [mm];
- h_f is the initial flange depth [mm];
- $d_{char,n,1}$ is the char depth on the exposed side [mm];
- d_0 is the depth of the zero-strength layer [mm];
- $b_{f,ef}$ is the effective flange width [mm];
- b_f is the initial flange width [mm];
- $d_{char,n,2}$ is the char depth on the lateral side [mm].

The depth of the zero-strength layer at any moment of the fire exposure can be calculated using the expressions given in Table 38.

Table 38. Best fit zero-strength layer parameters derived from simulations.

$t \leq t_{ch}$	
Tension	$d_0 = \frac{k_2}{\ln b_f} \cdot t$
Compression	$d_0 = \frac{2k_2}{\ln b_f} \cdot t$
$t > t_{ch}$	
PL1 tension	$d_0 = -\frac{1.9 \cdot t_f^{0.42} \cdot (t - t_{ch})^2}{b_f^{0.22} \cdot h_f^{1.5}} + \frac{t_f^{0.76} \cdot (t - t_{ch})}{34.5 \cdot b_f^{0.1}} + \frac{k_2 \cdot t_{ch}}{\ln b_f}$
PL1 compression	$d_0 = -\frac{28 \cdot (t - t_{ch})^2}{t_f^{0.14} \cdot b_f^{0.5} \cdot h_f^{1.1}} + \frac{t_f^{0.4} \cdot (t - t_{ch})}{2.111 \cdot b_f^{0.25}} + \frac{2k_2 \cdot t_{ch}}{\ln b_f}$
PL2 tension	$d_0 = -\frac{3.13 \cdot b_f^{0.035} \cdot (t - t_{ch})^2}{t_f^{0.9} \cdot h_f^{0.5}} + \frac{t_f^{0.8} \cdot b_f^{0.11} \cdot (t - t_{ch})}{83} + \frac{k_2 \cdot t_{ch}}{\ln b_f}$
PL2 compression	$d_0 = -\frac{200 \cdot (t - t_{ch})^2}{t_f^{0.9} \cdot b_f^{0.3} \cdot h_f^{0.9}} + \frac{t_f^{0.5} \cdot (t - t_{ch})}{3.5 \cdot b_f^{0.13}} + \frac{2k_2 \cdot t_{ch}}{\ln b_f}$

In case the failure time of the fire protection system is longer than the required fire resistance time, the fall-off time t_f may be substituted with the resistance time t .

5.3 Buckling

The verification of the buckling capacity of I-shaped members in walls depends on the bracing scenario. If both or neither flanges are braced, the verification against buckling about the z-axis should be performed according to the rules described in FprEN 1995-1-1:2025 (CEN, 2025a).

In case the member is unbraced on the fire exposed side, the compressive load acting on the I-shaped member should be divided to the flanges proportionally to their effective areas.

The effective length for lateral buckling about the z-axis for the unbraced flange of an I-shaped member with bracing on one side only should be calculated as:

$$l_{c,z,ef} = k_{fb,z} \cdot l \quad (41)$$

where

$l_{c,z,ef}$ is the effective length for lateral buckling about the z-axis [mm];

$k_{fb,z}$ is the factor for lateral buckling about the z-axis [-];

l is the length of the member [mm].

The factor for lateral buckling about the z-axis depends on the stiffness of the web and the critical load of the unbraced flange as:

$$k_{fb,z} = 0.67 - 0.05 \cdot \ln K_{rel} \quad (42)$$

with

$$K_{rel} = \frac{3 \cdot E_w \cdot b_{w,ef}^3 \cdot l^4}{\pi^2 \cdot h_w^3 \cdot E_f \cdot h_{f,ef} \cdot b_{f,ef}^3}$$

where

- E_w is the modulus of elasticity of the web material [MPa];
 $b_{w,ef}$ is the effective thickness of the web [mm];
 h_w is the height of the web (distance between the flanges) [mm];
 E_f is the modulus of elasticity of the flange material [MPa];
 $h_{f,ef}$ is the effective height of the unbraced flange [mm];
 $b_{f,ef}$ is the effective width of the unbraced flange [mm].

The calculation should continue with the normal buckling verification using the moment of inertia about the z-axis, the radius of gyration and relative slenderness.

5.4 Adhesives

Adhesive performance has been investigated in a previous project FIREWOOD. Based on the results of the project, a test method for the assessment of the adhesive performance in finger joints in the tension flange has been recommended and included in FprEN 1995-1-2:2025 Annex B (CEN, 2025b).

For the verification of the load-bearing capacity of I-joists in bending with the tension side exposed to fire, the depth of the zero-strength layer depends on the performance of the adhesive used in the finger joints of the flange. The depths of the zero-strength layer in tension given in Table 38 should be increased according to the finger joint class according to values given in Publication III or Table 39.

Table 39. Additional zero-strength layer depths for the tension flange.

Finger joint class	Additional zero-strength layer in tension [mm]
FJ1	0
FJ2	2
FJ3	4

5.5 Validation

5.5.1 Charring

The charring coefficients presented previously were validated against residual charred areas obtained from six unloaded and 13 loaded MST results as shown in Table 40.

The start time of charring, fall-off time, and start time of charring on the lateral side were taken from test results. Char depths and residual areas were calculated according to the equations in Table 37. Calculated duration was found only for the cases where exposed flanges were not completely charred in the tests. The right half of Table 40 shows tested and calculated times to reach the residual charred areas of tests.

Table 40. Validation of charring calculations.

Beam number	Residual flange area [mm ²]		Duration [min]	
	Test	Calculation	Test	Calculation
T1_B1	2806	0	46	30.0
T1_B2	572	0		32.6
T2_B1	1586	0	70	53.2
T2_B2	0	0		-
T3_B1	99	0	51.8	40.3
T3_B2	934	0		42.3
T4_B1	0	0	55.4	-
T4_B2	472	46		48.9
T5_B1	103	0	63.4	46.9
T5_B2	0	0		-
T6_B1	0	0	69.3	-
T6_B2	0	0		-
1.2	1706	1427	24.3	22.1
2.2	2034	2209	26.4	26.8
2.4	1130	818	29.7	26.5
3.3	1064	858	29.3	27.2
5.1	2209	2209	23.1	23.1
6.3	1505	1179	38.8	36.3
8.3	1979	2209	26.1	26.6
8.4	2183	2209	23.9	24.0
9.2	2022	2209	24.1	24.5
11.1	1663	1468	36.7	35.0
12.2	2130	2209	26.6	26.8
12.3	1705	1512	36.3	34.7
12.4	1912	2004	32.4	32.6

Figure 80 presents the calculated and tested times to reach the same charred cross-section areas. Results where the residual charred area was 0 in the tests have been omitted as the tested residual areas are measured only at the end time of the test, therefore, the time when the flange area charred completely is not known.

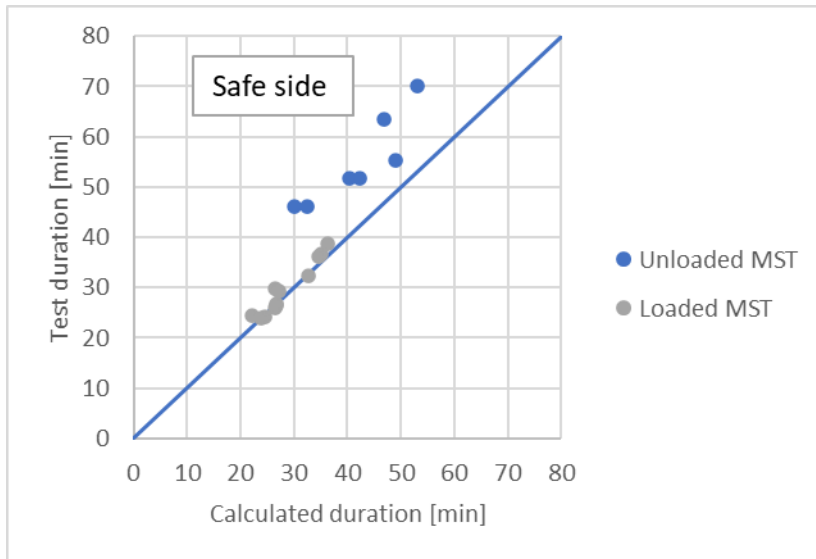


Figure 80. Comparison of calculated and tested durations to reach the same charred areas.

Calculated fire durations are mostly smaller than those measured in tests. Any points above the diagonal line are considered as safe, meaning that calculated times to reach the same residual flange area are shorter. Start time of charring in calculations was calculated according to Eurocode 5. Noticeably the calculated fire durations are more conservative for unloaded tests. This may be due to the deflections caused by loading or less secure fixation of the protection in the loaded tests.

No data was available on the residual cross-sections of full-scale furnace tests (FST) due to the purpose of FST usually being to verify the load-bearing capacity and the relatively long time between the turning off of the burners to extinguishment. The latter means that the residual cross-section continues to char and the data is not directly comparable to the charring measured in a standard fire exposure.

Generally, based on the available test data, the charring behaviour of I-joists is captured well by the proposed new coefficients.

5.5.2 Load-bearing capacity

The load-bearing capacities based on calculations and available test data have been compared to validate the charring and zero-strength layer expressions and the design model proposed within this thesis. Test measurements of the start time of charring (t_{ch}), the start time of lateral charring ($t_{ch,2}$) and the failure time of the fire protection system (t_f) have been used in calculations where possible.

An overview of loaded MST is presented in Table 41. The finger joint classes used in determining the depth of the zero-strength layer and the calculated TTF are shown on the right-hand side.

Table 41. Validation of zero-strength layer calculations based on loaded model-scale tests.

Test beam	Start time of charring [min]	Fall-off time [min]	Start of lateral charring [min]	Test duration [min]	FJ class	Calculated duration [min]
	t_{ch}	t_f	$t_{ch,2}$	t_{test}		t_{calc}
1.2	17.8	20.3	-	24.3	1	21.0
2.2	20.3	-	-	26.4	1	26.7
2.4	17.5	19.8	27.8	29.7	1	20.5
3.3	19.0	19.9	23.5	29.3	1	20.7
4.3	19.0	-	-	22.5	2	22.5
5.1	-	-	-	23.1	2	23.8
5.2	-	-	-	11.7	3	18.0
6.3	20.9	-	-	38.8	1	26.9
7.4	-	-	-	15.2	3	16.7
8.3	19.7	-	-	26.1	1	26.4
8.4	26.5	-	-	36.7	1	31.9
8.4	-	-	-	23.9	3	21.1
9.2	21.1	-	-	24.1	2	23.5
11.1	25.4	-	-	36.7	1	28.8
11.2	11.7	11.7	-	12.1	3	12.0
11.4	20.5	-	-	29.4	1	27.1
12.2	25.8	-	-	26.6	2	26.5
12.3	25.4	-	-	36.3	1	31.4
12.4	21.2	-	-	32.4	1	27.3

Additionally, tests conducted in a previous project have been added to the validation. See Table 42 for an overview of the test results and calculated time to failure (TTF).

Table 42. Validation of calculations based on loaded model-scale tests from Schmid (Schmid et al., 2011).

No	Loading	Bending moment [kNm]	Test duration [min]	Calculated duration [min]
1	CSW	3.83	17.7	16.3
2	CSW	3.35	25.7	20.3
3	CSW	1.86	41.1	26.4
4	CSW	1.34	47.5	28.3
5	CSW	1.02	52	29.1
6	CSW	0.49	34	37.6
7	CSW	1.79	26.2	21.9
8	CSW	1.88	71.4	46.3
9	TSW	3.56	29.8	22.9
10	TSW	3.13	40.1	28.9
11	TSW	3.7	36.5	28.1
12	TSW	3.4	38.4	28.6
13	TSW	3.6	45.3	28.3
14	TSW	3.5	32.3	28.5

The calculated and tested TTF are compared visually in Figure 81. The top left side of the grey line is the safe side, where the test results are longer than the calculated TTF of the same configuration.

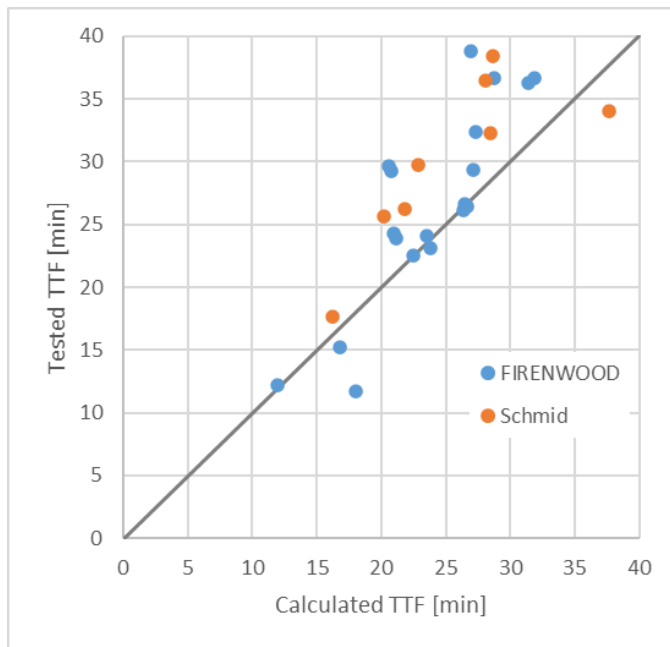


Figure 81. Comparison of tested and calculated time to failure (TTF).

The calculated times to failure according to the database of full-scale floor tests are shown in Table 43. The same configurations and fall-off times from the test results were used for the calculations. As no data on the finger joint classes was unavailable, the assumption of FJ2 was used in the calculations of the zero-strength layer depths for I-joists with sawn wood flanges.

Table 43. Validation of calculations based on loaded full-scale floor tests.

No	Cavity insulation	Fall-off time, min	Time to failure, min	Load, kN/m ²	Calculated time to failure, min	$\frac{TTF_{calc}}{TTF_{test}}, \%$
F1	Void	28	34	1.03	32.67	96.09
F2	PL2	63	70	1.5	57.03	81.47
F3	PL2	44	61	1.35	48.96	80.26
F4	PL2	59	65	1.35	61.11	94.02
F5	PL2	22.5	33	1.35	28.13	85.24
F6	PL1	15	29	2.7	26.00	89.66
F7	Void	27	31	1.5	31.69	102.23
F8	Void	25	30	0.7	31.20	104
F9	Void	27	30	1.0	32.73	109.1
F10	PL2	58	73	1.5	57.86	79.26
F11	Void	29	34	1.02	32.68	96.12
F12	Void	31	35	1.06	34.98	99.94
F13	Void	37	37	1.09	34.79	94.03
F14	Void	29	34	1.02	32.68	96.12
F15	Void	24	30	1.0	28.98	96.60
F16	PL2	65	65	1.5	65.76	101.17
F17	PL2	41	75	1.7	43.53	58.04
F18	Void	37	39	1.02	35.81	91.82
F19	PL2	78	82	1.36	71.11	86.72
F20	Void	52	72	1.7	53.19	73.88
F21	Void	28	33	1.12	31.92	96.73
F22	Void	22	30	1.02	27.67	92.23
F23	Void	39	39	1.02	35.81	91.82

The calculated and tested TTF in full-scale floor tests are compared visually in Figure 82. The top left side of the grey line is the safe side, where the test results are longer than the calculated TTF of the same configuration. The floor test (F) results are grouped according to the type of cavity insulation (PL).

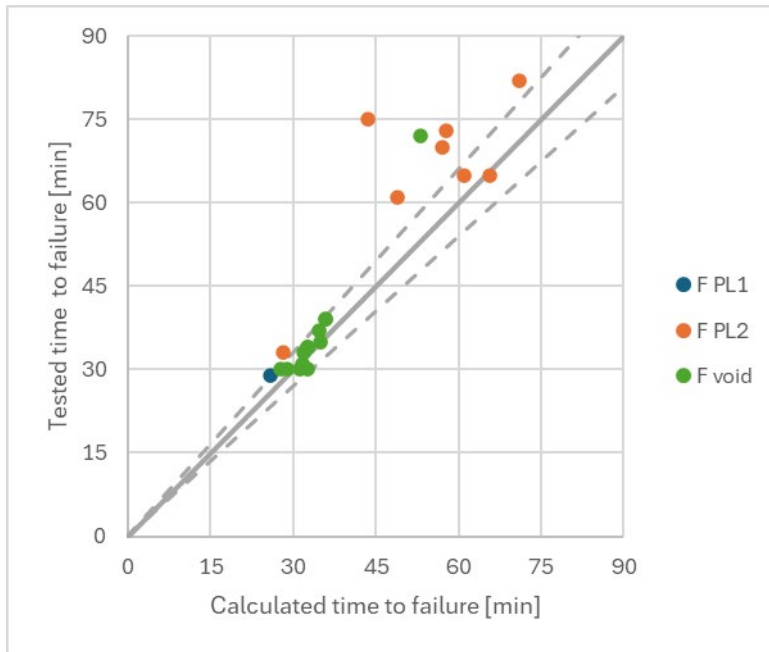


Figure 82. Comparison of tested and calculated time to failure (TTF) in full-scale floor tests. Dashed lines represent $\pm 10\%$ difference.

The calculated times to failure were on average 91% of the tested values. Test F9 is overestimated by 9.1%. The other unsafe calculation results are within a 4% margin.

The fall-off time of the fire protection system has the greatest influence on the calculated time to failure. F18 and F21 are an example of this phenomenon, where in the test, the specimen was able to last for a long time, either by redistribution of loads or if the fall-off occurred partially. In the calculations, the reported fall-off time is taken to occur simultaneously over the whole exposed surface.

The possible reasons for the overestimation of the time to failure in the calculations is the uncertainty of the real strength of the tested I-joists and the real occurrence of the fall-off time. In the tests, the whole specimen is rarely observed throughout the test and so, a part of the fire protection system may have failed earlier than what was reported.

The calculated times to failure according to the database of full-scale wall tests are shown in Table 44. The same configurations and fall-off times from the test results were used for the calculations.

Table 44. Validation of calculations based on loaded full-scale wall tests.

No	Cavity insulation	Fall-off time, min	Time to failure, min	Load per stud, kN	Calculated time to failure, min	$\frac{TTF_{calc}}{TTF_{test}}$, %
W1	PL2	84	99	10.1	52.2	52.73
W2	PL2	30	45	10.1	30.83	68.51
W3	PL2	28	35	10.2	31.46	89.89
W4	PL2	33	35	10.2	33	94.29
W5	PL2	62	83	9.6	53.75	64.76
W6	PL2	82	120	13.5	56.8	47.33
W7	PL2	66	82.9	54	66	79.61
W8	PL2	61	61	17	55.7	91.31
W9	PL1	21	57	22	21.36	37.47
W10	PL2	77	85	22	64.9	76.35
W11	PL2	47	69	24	47.14	68.32
W12	PL2	27	40	17	27.96	69.9
W13	PL2	102	113	50	78.72	69.66
W14	PL2	48	82	54	48	58.54
W15	PL2	NA	69	24	62.33	90.33
W16	PL1	19	57	22	19.77	34.68
W17	PL2	74	121	48	68.73	56.8

The calculated and tested TTF in full-scale wall tests are compared visually in Figure 83. The top left side of the grey line is the safe side, where the test results are longer than the calculated TTF of the same configuration. The wall test (W) results are grouped according to the type of cavity insulation (PL).

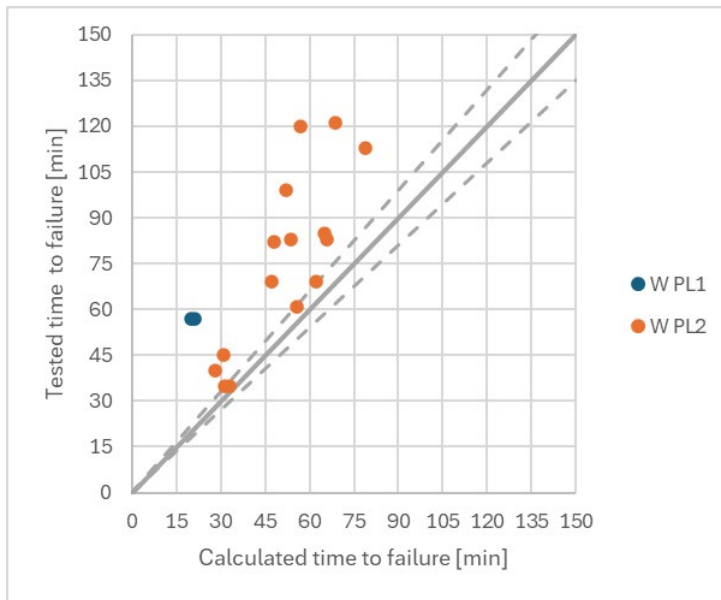


Figure 83. Comparison of tested and calculated time to failure (TTF) in full-scale wall tests. Dashed lines represent $\pm 10\%$ difference.

The calculated times to failure were on average 68% of the tested values. All calculations are on the safe side. Most calculations are more than 10% shorter than test results.

The fall-off time of the fire protection system has the greatest influence on the calculated time to failure. After the fall-off time, the wall studs become braced on one side only and lateral buckling of the fire exposed unbraced flange is governing. Most calculations show the time to failure at or just after the fall-off of the claddings.

Charring on the lateral sides of flanges with less than 40-mm depth are probably overestimated due to the calculation principles where less than 40-mm thick cavity insulation is not considered to offer protection.

6 Discussion

This chapter discusses the main findings of the research, evaluates the results from both numerical simulations and experimental investigations, and highlights the implications for fire design methods for wooden I-joists. Contributions, limitations, and suggestions for future work are also outlined.

The main outcome of the work conducted throughout the thesis is the design model for wooden I-shaped members exposed to the standard fire. The proposed design model is harmonised with the ECSM and all principles of the Eurocodes. The new model is valid for members in bending and compression and is flexible to use with a variety of fire protection systems and cavity insulations. The model is based on extensive thermal FE simulations, fire testing and ambient compression tests.

6.1 Finite element methods

Finite element modelling was used to investigate the thermal, thermo-mechanical and buckling behaviour of I-joists.

The thermal FE simulations were conducted to investigate the charring behaviour depending on different flange sizes, fire protection systems and cavity insulation. Thermal properties of widely accepted literature were used and gave appropriate results compared to model-scale furnace fire test results. In the longer fire exposures, the simulations became more conservative.

The FE simulations were further analysed to develop the charring coefficients. The charred areas of the fire exposed flange were calculated using MATLAB scripts. The reduction in the charred areas showed distinct phases which supported the adoption of the ECSM. Interestingly, rapid charring in the few minutes after the fall-off time was observed from the simulation results. This phenomenon is considered through the post-protection coefficient for the fire exposed side as the exposed side has had the most pre-heating effects when the protection was still in place. For the lateral sides, the preheating is only occurring in the zone closest to the fire exposed side, whereas the further away from the exposed side, the heating lessens and is more uniform due to the protection offered by the cavity insulation.

Due to the sheer amount of data points, a variety of scripts were used to conduct the analysis of the FE data. The proprietary scripts are a large part of the novelty of the thesis. Specifically, a complex regression analysis was undertaken, resulting in the most optimal parameter functions for the various charring coefficients which most effectively captured the charring behaviour recorded in all FE simulation cases.

An important outcome is that the section and conversion factors for charring at the exposed and lateral sides are the same regardless of the type of cavity insulation. The charring behaviour of I-joists behind the fire protection system is very similar in the simulated cases with stone and glass wool cavity insulation. This is in line with the Eurocode 5 principles, where the charring behind protection is affected only by the parameters of the protection and not the cavity insulation.

The type of insulation used in the cavities affects the charring of I-joists after the fall-off of the fire protection system. The charring is more rapid with glass wool compared to stone wool cavity insulation, as can be expected based on previous studies. The protection level of the cavity insulation also affects the start time of lateral charring and the start time of charring on the web.

Based on the FE simulations, the most appropriate criteria for the start time of lateral charring and the start time of charring on the web were chosen. The start time of lateral charring is the time to reach 300 °C on the far corner of the exposed flange. The start time of charring on the web was taken as the time to reach 300 °C at a height of the 45° angle line from the edge of the flange. In the calculations, these times can be found using the SFM with a good agreement to the FE simulations and furnace fire tests.

The start time of charring of the web is conservative in the calculations; however, that is appropriate for I-joists as the protection of the web against charring is important for the load-bearing capacity. The loss of the web reduces the capacity significantly, as the I-joist is then unable to retain its shape and redistribute loads effectively.

The mechanical behaviour of I-joists was investigated using thermo-mechanical simulations of beams, thermal FE simulations in combination with strength reduction factors and FE modelling of columns in compression at ambient temperature. The thermo-mechanical simulations were compared to model-scale loaded fire test results. The compression test results were used to validate the ambient temperature FE models.

The thermo-mechanical simulations could not replicate the deflections obtained from fire tests. The simulated deflections were always smaller than the test measurements. Even after reducing the moduli of elasticity of the components, the simulation did not capture the deflection as it occurred in the tests. Nonetheless, the simulations mostly did not reach the test times. This points to the difference in the approach of tests and simulations where in the tests the I-joists are able to redistribute loads and possibly the cross-section does not remain planar, as is the assumption in the simulations.

The design model was developed based on effective areas obtained from thermal FE simulation results with the temperatures substituted by the reduction factors for tensile and compressive strength at elevated temperatures. The resulting effective areas and the charring calculation model were used to compute the zero-strength layer depths for each simulation case and every timestep. A regression script was utilised to develop the zero-strength depth equations. These were derived as a stepwise regression with the most significant terms being the flange dimensions and the failure time of the fire protection system.

The design model is highly accurate in comparison to the thermo-mechanical simulations. The calculated and simulated times to failure show very good agreement apart from a few cases where the simulation stopped before the start time of charring. These cases where the simulation stops early seem to be unrealistic and not representative of expected behaviour that has been observed in fire tests.

The use of thermo-mechanical simulations in SAFIR added limited value to the work of this thesis due to modelling assumptions which in some cases led to early convergence errors. The models could be improved with the inclusion of some limited non-linear rotation of the cross-section, which may be able to better capture the real effects of stress redistribution and greater deflections.

The ambient FE simulations conducted by Kerge (Kerge, 2024) were crucial for developing the understanding of the buckling behaviour of I-joists when bracing is on one side only. The results of compression tests were used to validate the FE model and further models were created to extend the test results.

6.2 Experimental investigations

Loaded and unloaded model-scale fire tests, full-scale fire tests and ambient temperature compression tests were conducted and analysed to gain insight into the thermal and mechanical behaviour of I-joists.

Six unloaded model scale furnace fire tests were conducted within this study to investigate the charring behaviour of I-joists in assemblies with stone and glass wool cavity insulation materials. The temperatures in various places were recorded throughout the test duration.

Each test featured two I-joists with different flange geometries. The flanges were of solid wood or LVL. Both showed similar charring behaviour in the tests. Therefore, the same charring coefficients are valid. For other materials, a different charring rate may be used in practice. The temperature measurements showed good agreement with previous studies. The char layer developed as expected.

Test data from nineteen loaded model-scale fire tests was available from the FIREWOOD project. These tests were conducted to investigate the behaviour of various adhesives used in the finger joints in the tension flanges. The I-joists were loaded in bending with the tension flange on the fire exposed side. Deflections and failure times of the beams were recorded. The test data was used for validating the thermo-mechanical simulations and the developed fire design model.

Differences were observed in the performance of the finger joints in the tension flanges. Based on further tests within the project, three finger joint classes have been proposed. The design model for I-joists considers the adhesive performance based on the finger joint classes through the calculation of the zero-strength layer depth. Adhesive failure in the bond lines between the flange and the web have not been observed in any of the performed fire tests.

The extensive test series of ambient compression tests gave invaluable insight into the behaviour of I-joists in axial loading. The tests investigated the effect of a variety of bracing and loading conditions on the buckling capacity of different I-joist geometries. The modelling extended the test data. The complex phenomena were simplified according to assumptions given in FprEN 1995-1-1:2025 Annex B (CEN, 2025a) for the unbraced flange to be considered as a compression element with a smeared restraint.

Full-scale fire test results of wall and floor assemblies were used for validation of the developed design model. A database of full-scale furnace fire tests consisting of 23 floor and 17 wall test results was gathered from different producers.

6.3 Design model

The design model developed within this thesis is an improvement of previous works and follows the ECSM. It is harmonised with the principles of the new generation of Eurocodes. The model is based on extensive experimental and computational investigations. The charring equations were compared to model-scale fire tests. The design model was validated against the database of full-scale fire test results. The validation showed that the calculation results are most affected by the fall-off time of the fire protection system.

The development of the design model was a multi-step process. The basis of the model for I-joists is the design model for timber frame assemblies with rectangular members developed by Tiso (Tiso, 2018). The charring coefficients for rectangular members were not appropriate for I-shaped members due to the smaller overall dimensions of the flanges

and the different mechanical response of I-joists. For those reasons, the new model for I-joists was developed based on simulations and experimental data.

Charring on the exposed side can occur in up to four linear phases depending on the properties and behaviour of the fire protection system. The development of the char layer depth behind fire protection is similar to the prediction according to the Eurocode 5 calculation model. After the fall-off of fire protection, an interesting phenomenon was observed. For a short period of time, the charring rate is significantly increased until the preheated wood has charred. Then, the charring rate consolidates to a stable rate until the end of the fire exposure.

Charring on the lateral sides of the fire exposed flange is simplified to a maximum of two phases – before and after the fall-off of fire protection. The temperature gradient on the lateral sides is steep and therefore, the phase of rapid charring after fall-off occurs only in a limited area close to the fire exposed side and is averaged over the entire flange depth.

The design model was developed as charring and zero-strength layer equations. Firstly, the charring equations were proposed using a variety of coefficients which could consider the phenomena occurring in different charring phases. Secondly, the expressions for calculating the zero-strength layer depth were developed based on further simulation data.

With the use of various scripts, all simulation data was analysed. The charring coefficients and the expressions for calculating the depth of the zero-strength layer were derived using various optimisation scripts to fit the simulation results.

The combined section and conversion coefficient $k_{s,n,1}$ for the fire exposed side and $k_{s,n,2}$ for the lateral sides considers the dimensions of the exposed flange. The coefficient values from the optimisation script were relatively similar values for assemblies insulated with stone or glass wool. This confirmed that the equations appropriately decouple different effects.

The protection coefficient k_2 is a property of the fire protection system and shows how much charring is slowed behind such a system compared to unprotected charring. The values given in FprEN 1995-1-2:2025 were appropriate for I-joists.

The post-protection coefficient for the fire exposed side $k_{3,1}$ depends on the fall-off time and represents the rapid charring rate that occurs on the fire exposed side immediately after fall-off. For longer fall-off times the increase of the charring rate is lesser, therefore the coefficient is linearly dependent on the fall-off time with a negative slope. The values of the coefficient are different depending on the type of cavity insulation, for assemblies with PL1 cavity insulation the coefficient is more dependent on the fall-off time.

The consolidated charring phase is represented by the consolidation coefficient k_4 . The values are dependent on the protection level of the cavity insulation. For I-joists in assemblies with PL1 cavity insulation the coefficient is linearly dependent on the consolidation time with a negative slope. In the case of PL2 cavity insulation the slope is positive. These effects are consistent with the literature about the fire performance of PL1 and PL2 insulations where the latter provide much less protection to the timber member against fire and charring.

The post-protection coefficient for the lateral side $k_{3,2}$ is used to consider the protection offered by the cavity insulation to the lateral sides of the fire exposed flange. The values are calculated using a linear equation depending on the greater of the start of lateral charring or the fall-off time with a positive slope. The slope is steeper for assemblies with PL2 cavity insulation.

The expressions for calculating the depth of the zero-strength layer are dependent on the load scenario (compression or tension), the protection level of the cavity insulation, the geometry of the I-joist, the start time of charring and the fall-off time of the fire protection system. The d_0 equations were developed based on simulations and the charring calculations. The zero-strength layer is compensating for the difference between the simulated effective areas and the calculated charred areas. The depth increases linearly for the time before the start of charring. After the start of charring, the zero-strength layer is calculated as a quadratic function. The depth is greater for members in compression.

The expressions for the d_0 are complex in order to consider the different effects accurately. However, in practical use, the engineer will have all the necessary inputs available to them.

Buckling capacity is verified according to the principles given in the Eurocodes if the I-joist is unbraced or has bracing on both sides of the section. If the fire protection system has fallen off, then the I-joist becomes braced against lateral buckling only on one side. For these cases a new factor was developed that considers the stiffness of the web and can be used to calculate the effective buckling length of the I-joist with bracing on one side. The verification with full-scale test results showed that this approach is conservative. In fire tests, the I-shaped members showed longer fire resistance after the fall-off of the fire protection system than the calculations.

The load-bearing calculation results are conservative compared to the full-scale tests. This is possibly due to the high specificity of the tested assemblies. Fire tests are typically conducted with the goal of rating particular combinations and construction types for fire resistance. Additionally, the test data gives only the strength classes of the I-joist components. The real strength is possibly much greater than the declared properties of the strength class.

In most of the test data, the fall-off times were assessed visually. That means that the first time when a fall-off of a part of the last layer of the fire protection system was noticed has been recorded. The real fall-off time could have happened at any point between the previous and current observations were made. That possibly introduces a lag in the recorded time.

The charring equations were compared to the residual charred areas obtained from the model-scale fire tests. The comparison of the times to reach the same flange area show that the calculations are conservative, giving shorter times than the test durations.

The design model can be implemented in engineering practice and is harmonised with the Eurocodes. The greatest influence on the char depth and load-bearing capacity of I-joists is had by the failure time of the fire protection system. Every minute of fire resistance is important for I-joists. The failure time of the fire protection system is a crucial parameter for the fire resistance of timber frame assemblies with I-shaped members. For I-joists, the protection against charring is extremely important as they are highly optimised in their shape and material use and there is no sacrificial timber.

Based on the validation of the design model with model- and full-scale furnace fire tests, thermo-mechanical simulations and compression tests, the model is conservative. Only part of the risks considered in the design model, happened in the validation tests. This may lead to oversized assemblies; however, the model is valuable as a cost-effective substitute for testing and for the prediction of test configurations.

The proposed design model is reliable for such sensitive structural members as the I-joists. As until now there has not been an open and flexible calculation model, the contribution of this thesis has added to the state of the art of fire design of timber structures.

6.4 Limitations and further research

While the results of this study are promising and contribute significantly to the development of fire design methods for timber I-joists, several limitations should be acknowledged:

- **Material modelling assumptions:** The FE simulations were based on isotropic and homogeneous material properties. Real timber exhibits anisotropy and variability, which may affect the accuracy of the predictions, particularly under elevated temperatures.
- **Moisture content and migration:** The effects of varying initial moisture content and moisture migration were not modelled, although both are known to influence thermal and mechanical responses.
- **Adhesive degradation:** The adhesive lines were not explicitly modelled in the FE simulations. This simplification limits the ability to predict delamination and adhesive failure modes, which were seen in some experimental results.
- **Boundary conditions and restraint modelling:** The boundary conditions used in the models were idealised and may not fully reflect real structural systems where restraint and bracing vary.
- **Scope of fire exposure:** The scope of the work was limited to standard fire curves (ISO 834), and did not consider natural fire scenarios or varying heating rates as found in parametric fire design.

Future research directions are proposed to address these limitations and extend the applicability of the proposed design model:

- **Simplification of design equations:** A simpler approach with fewer variables may be possible, however with a reduction of accuracy.
- **Integration of natural and parametric fires:** To generalise the applicability of the model, future studies should incorporate parametric fire exposures and natural fire conditions. This would allow investigation of delayed ignition, ventilation effects, and cooling phases.
- **Advanced material and bond-line modelling:** Incorporating orthotropic material properties, transient moisture flow, and bond-line degradation models could significantly improve predictive capabilities.
- **Advanced modelling of buckling:** numerical investigation of the effect of the loss of bracing on one side of the assembly at elevated temperatures.
- **Full-scale testing of alternative geometries:** Larger-scale testing campaigns with additional flange geometries, new insulation materials, different timber species, and hybrid composite solutions would help validate and refine the model further.
- **Software development:** An implementation of the model into open-source design tools or plug-ins for engineering software would encourage broader adoption by practitioners.

6.5 Closing remarks

This chapter has drawn together the critical insights obtained through an integrated programme of numerical simulation and experimental investigation. The fire design model developed through this work represents a step forward in understanding and predicting the fire resistance of timber I-joists.

By incorporating a range of influencing parameters – including flange geometry, insulation type, adhesive performance, and failure modes – the proposed method offers a more complete and reliable tool for engineering applications. It reflects the physical behaviour observed in model-scale testing and captures trends that were previously underrepresented in simplified calculation approaches.

The harmonisation of the model with the Effective Cross-Section Method ensures compatibility with the evolving Eurocode 5 framework and positions the work for adoption in both regulatory and professional contexts. The model's ability to address practical design variables, such as protection fall-off, slenderness, and restraint conditions, makes it particularly suitable for real-world design scenarios.

The development of a new coefficient for evaluating the buckling behaviour of the unbraced flange introduces a novel way of incorporating web stiffness and restraint into compression capacity checks. This approach allows a nuanced treatment of structural instability, providing an improvement over earlier models that treated such members in a simplified manner.

Overall, the research offers a robust framework that not only advances scientific understanding but also delivers a user-oriented calculation method. It establishes a solid basis for future investigations and design practices aimed at improving the fire resilience of timber structures.

7 Summary

The aim of this thesis was to investigate the behaviour of wooden I-shaped members when exposed to standard fire conditions. The work focused on understanding the charring mechanisms, insulation effects, and load-bearing capacity of fire-exposed I-joists with various flange geometries and cavity insulation materials. The outcome of this research is an improved fire design model, capable of considering different charring and loading scenarios with respect to different fire protection systems and cavity insulation materials.

Previous studies in this area date back several years and focused on earlier design methodologies, which have not been significantly updated. These older approaches were limited both in terms of applicability and experimental validation. This thesis addresses these gaps by combining modern finite element simulations with physical testing to develop and validate a more versatile and reliable design approach.

The research methodology included both numerical and experimental components. Finite element simulations were used to model thermal and thermo-mechanical behaviour, with the thermal models predicting temperature profiles and charring progression, and the mechanical models simulating deformation and failure under fire exposure. These models were calibrated using results from model-scale furnace fire tests and ambient compression tests.

Extensive testing was conducted to evaluate performance under both loaded and unloaded fire scenarios. Six unloaded model-scale furnace fire tests were conducted on different I-joists with stone and glass wool cavity insulation. The temperature development was measured in various positions within the specimen. Data from 19 loaded model-scale tests was analysed to determine the effect of different adhesives on the load-bearing capacity in bending. These tests provided insight into the role of gypsum board fall-off, adhesive performance, cavity insulation, and applied load. Temperatures, charred areas, deflections and failure times depths were recorded and compared with simulation results to assess the accuracy of simulations.

An improved analytical model was developed to predict the char depth and the depth of the zero-strength layer. The model was developed in harmony with the Effective Cross-Section Method (ECSM) framework, ensuring consistency with evolving European design standards. The fire design model for I-shaped members is able to consider the flange dimensions and the geometry of the I-joists, the adhesives used in finger joints, different cavity insulation types and fire protection systems. Model parameters were developed using a combination of regression-based optimisation techniques and rule-based scripting to ensure generality across the parameter space. The model was validated using a database of full-scale fire tests, providing strong experimental confirmation of its predictive accuracy and engineering applicability.

One of the major findings is that the start of charring on the exposed side is largely unaffected by the type of cavity insulation, confirming the assumptions used in simplified calculation models. However, lateral charring shows a clear dependency on insulation type, with stone wool providing significantly longer protection times than glass wool, particularly at greater flange depths. Another important observation is that the calculation methods provided in Eurocode 5 Part 1-2 for determining the start of charring on the exposed and lateral sides and on the web are slightly conservative when compared to the results of detailed thermal simulations. This conservativeness was observed consistently across multiple configurations and insulation types. The simplified

calculation rules, while less precise, offer a reliable and safe estimate for engineering applications, particularly in design situations where a detailed simulation is not feasible.

The thermo-mechanical simulations, while mostly conservative, occasionally failed to converge before physical failure in certain test scenarios, particularly for large cross-sections or for short failure times, highlighting the importance of modelling assumptions and convergence criteria. An important finding of this work is that the unbraced flange can be effectively treated as a compression member with smeared lateral restraint provided by the web and opposite flange. A novel coefficient was developed to reduce the effective buckling length of I-joists in compression with one unbraced flange, accounting for the relative stiffness of the web. This coefficient allows more accurate representation of lateral-torsional restraint, especially for tall, slender cross-sections where the flange is prone to instability. Compression load capacity with one unbraced flange was shown to be highly sensitive to flange width, web slenderness and stiffness.

Several limitations were identified in the course of the work. These include the simplification of material properties and boundary conditions in the simulations, and the exclusion of adhesive bond-line modelling. Additionally, the scope of this thesis is limited to only standard fire exposure.

Despite these limitations, the developed design model provides a conservative and robust framework for evaluating the fire resistance of timber I-joists. It offers improvements over previous models, particularly in its ability to account for variation in insulation type and flange dimensions. The model can serve as a basis for engineering calculations and may support the development of future performance-based design codes.

This work contributes to the broader field of timber engineering by providing updated data, validated modelling approaches, and practical guidance for fire design. It also establishes a framework that can be extended to include other materials, larger structural assemblies, or different fire exposure scenarios. The model has been included in the new generation of Eurocode 5 part 1-2.

In summary, this thesis demonstrates that a balanced approach combining simulations and experimental data can produce a design model that improves safety, practicality, and understanding in the fire resistance design of timber structures. The findings form a strong foundation for continued development in this field and underscore the importance of integrating real behaviour into simplified engineering tools.

List of figures

Figure 1. Timber frame assembly (Tiso, 2018).....	14
Figure 2. I-joist components (left) and different shapes (right): (a) glued thin webbed beam, (b) rectangular groove, (c) trapezoidal groove (I-Joists, n.d.).	15
Figure 3. Thin-webbed beams EN 1995-1-1:2004 (CEN, 2004b).....	16
Figure 4. Compressive member on smeared elastic restraint (Figure B.10 of FprEN 1995-1-1:2025 (CEN, 2025a)).	17
Figure 5. Charring phases of the European Charring Model, according to FprEN 1995-1-2:2025 (CEN, 2025b)	19
Figure 6. Numbering and function of the layers in a timber frame structure.	22
Figure 7. Flowchart of the procedure to develop charring and zero-strength layer equations.	30
Figure 8. Flowchart of the procedure for the development of the design model.	31
Figure 9. Plan (left) and section (right) views of the model-scale test specimen.	34
Figure 10. Thermocouple placements on tested I-joists.....	34
Figure 11. Thermocouples on the fire exposed flange (left) and the finished specimen (right).	35
Figure 12. All temperatures measured in MST T5.....	36
Figure 13. All temperatures measured in MST T1.....	37
Figure 14. Thermal conductivities (left) and density ratios (right) used in FE simulations.40	
Figure 15. Specific heat of timber, wood-based boards and gypsum plasterboard (left) and stone and glass wool (right) used in FE simulations.	41
Figure 16. Element distribution in thermal simulations.....	42
Figure 17. Fire exposed flange.	43
Figure 18. Charred areas of 13-mm thick gypsum with 30-min fall-off time with stone wool.	46
Figure 19. Charred areas of 13-mm thick gypsum with 45-min fall-off time with stone wool.	46
Figure 20. Charred areas of 13-mm thick gypsum with 30-min fall-off time with glass wool.	47
Figure 21. Charred areas of 13-mm thick gypsum with 45-min fall-off time with glass wool.	47
Figure 22. Start time of charring.	48
Figure 23. Thicknesses of insulation to calculate the start time of lateral charring and the start time of charring on the web	49
Figure 24. Start time of lateral charring with stone wool: a) unprotected, b) 13-mm gypsum, c) 15-mm gypsum, d) 20-mm gypsum. Legend key: flange depth (mm)/fall-off time (min).....	49
Figure 25. Start time of lateral charring with glass wool: a) unprotected, b) 13-mm gypsum, c) 15-mm gypsum, d) 20-mm gypsum. Legend key: flange depth (mm)/fall-off time (min).....	50
Figure 26. Height of the first node to exceed 300 °C on the side of the web.	51
Figure 27. Start time of charring on the web with stone wool: a) unprotected, b) 13-mm gypsum, c) 15-mm gypsum, d) 20-mm gypsum. Legend key: flange width (mm) x flange depth (mm).	52

Figure 28. Start time of charring on the web with glass wool: a) unprotected, b) 13-mm gypsum, c) 15-mm gypsum, d) 20-mm gypsum. Legend key: flange width (mm) x flange depth (mm).	53
Figure 29. Comparison of tested and simulated char depths in tests T5 (left) and T1 (right.)	54
Figure 30. Comparison of simulated and calculated charred areas for assemblies insulated with stone wool and protected by 13-mm gypsum plasterboard with 30-minute fall-off time.	57
Figure 31. Comparison of simulated and calculated charred areas for assemblies insulated with stone wool and protected by 13-mm gypsum plasterboard with 45-minute fall-off time.	58
Figure 32. Comparison of simulated and calculated charred areas for assemblies insulated with glass wool and protected by 13-mm gypsum plasterboard with 30-minute fall-off time.	58
Figure 33. Comparison of simulated and calculated charred areas for assemblies insulated with glass wool and protected by 13-mm gypsum plasterboard with 45-minute fall-off time.	59
Figure 34. Location of thermocouples and finger-joints.....	61
Figure 35. Section of the specimen and location of thermocouples.	62
Figure 36. Loaded model-scale test setup from the FIREWOOD report (Olofsson et al., 2022).	62
Figure 37. Deflections from loaded MST.....	64
Figure 38. Thermo-mechanical simulation setup.....	65
Figure 39. Schematic of mechanical simulation beam.....	66
Figure 40. Comparison of deflections from loaded model-scale tests, part 1.	67
Figure 41. Comparison of deflections from loaded model-scale tests, part 2.	68
Figure 42. Comparison of simulated and calculated times to failure.	70
Figure 43. Effective areas in tension of simulations with 15-mm thick gypsum with 30-min fall-off time with stone wool.....	72
Figure 44. Effective areas in compression of simulations with 15-mm thick gypsum with 30-min fall-off time with stone wool.	72
Figure 45. Zero-strength layer depths for tension in assemblies insulated with stone wool and protected by 15-mm gypsum plasterboard with 30-minute fall-off time.....	75
Figure 46. Zero-strength layer depths for compression in assemblies insulated with stone wool and protected by 15-mm gypsum plasterboard with 30-minute fall-off time.	75
Figure 47. Zero-strength layer depths for tension in assemblies insulated with stone wool and protected by 15-mm gypsum plasterboard with 60-minute fall-off time.....	76
Figure 48. Zero-strength layer depths for compression in assemblies insulated with stone wool and protected by 15-mm gypsum plasterboard with 60-minute fall-off time.	76
Figure 49. Zero-strength layer depths for tension in assemblies insulated with glass wool and protected by 15-mm gypsum plasterboard with 30-minute fall-off time.....	77
Figure 50. Zero-strength layer depths for compression in assemblies insulated with glass wool and protected by 15-mm gypsum plasterboard with 30-minute fall-off time.	77
Figure 51. Zero-strength layer depths for tension in assemblies insulated with glass wool and protected by 15-mm gypsum plasterboard with 60-minute fall-off time.....	78
Figure 52. Zero-strength layer depths for compression in assemblies insulated with glass wool and protected by 15-mm gypsum plasterboard with 60-minute fall-off time.	78

Figure 53. Comparison of simulated and calculated effective areas in tension for assemblies insulated with stone wool and protected by 15-mm gypsum plasterboard with 30-minute fall-off time.....	80
Figure 54. Comparison of simulated and calculated effective areas in compression for assemblies insulated with stone wool and protected by 15-mm gypsum plasterboard with 30-minute fall-off time.....	81
Figure 55. Comparison of simulated and calculated effective areas in tension for assemblies insulated with stone wool and protected by 15-mm gypsum plasterboard with 60-minute fall-off time.....	81
Figure 56. Comparison of simulated and calculated effective areas in compression for assemblies insulated with stone wool and protected by 15-mm gypsum plasterboard with 60-minute fall-off time.....	82
Figure 57. Comparison of simulated and calculated effective areas in tension for assemblies insulated with glass wool and protected by 15-mm gypsum plasterboard with 30-minute fall-off time.....	82
Figure 58. Comparison of simulated and calculated effective areas in compression for assemblies insulated with glass wool and protected by 15-mm gypsum plasterboard with 30-minute fall-off time.....	83
Figure 59. Comparison of simulated and calculated effective areas in tension for assemblies insulated with glass wool and protected by 15-mm gypsum plasterboard with 60-minute fall-off time.....	83
Figure 60. Comparison of simulated and calculated effective areas in compression for assemblies insulated with glass wool and protected by 15-mm gypsum plasterboard with 60-minute fall-off time.....	84
Figure 61. Bracing and load placement in ambient compression tests.	85
Figure 62. Types of reduced cross-sections of I-joists.....	85
Figure 63. Compression test specimen for test series 3.	88
Figure 64. Web acting as a cantilever beam (left), unbraced flange on a continuous spring support (middle), web substituted by the effective length for lateral buckling (right). .	89
Figure 65. Different views of the FE structural model for compression members.	90
Figure 66. 3D body created in the model (left); rigid links present in the support are depicted (right).	91
Figure 67. Results of compression test series 1.	94
Figure 68. Results of compression test series 2.	95
Figure 69. Results of compression test series 3.	96
Figure 70. Average compression capacities in centrally loaded tests.....	97
Figure 71. Comparison of full and reduced flanges under centric loading.	97
Figure 72. Comparison of different load placements.	98
Figure 73. Comparison of reduced flanges in eccentric loading.	98
Figure 74. Validation of FE compression models.	99
Figure 75. Graphical comparison of load-bearing capacity from tests and elastic critical load from the model.	100
Figure 76. Effective buckling length vs relative stiffness.	102
Figure 77. Calculated and tested compression capacities from ambient tests. Dashed lines represent $\pm 15\%$ difference.....	102
Figure 78. I-joist. (a) Naming of the parts of an I-joist; (b) Principles of the new design model.	103

Figure 79. Design model for I-shaped timber members of timber frame assemblies according to FprEN 1995-1-2:2025 (CEN, 2025b).	104
Figure 80. Comparison of calculated and tested durations to reach the same charred areas.....	110
Figure 81. Comparison of tested and calculated time to failure (TTF).....	112
Figure 82. Comparison of tested and calculated time to failure (TTF) in full-scale floor tests. Dashed lines represent $\pm 10\%$ difference.....	114
Figure 83. Comparison of tested and calculated time to failure (TTF) in full-scale wall tests. Dashed lines represent $\pm 10\%$ difference.....	115

List of tables

Table 1. Model-scale tests.	25
Table 2. I-joist profiles tested in full-scale.	26
Table 3. Full-scale fire test results.....	27
Table 4. Unloaded model-scale furnace tests.....	33
Table 5. Tested start times of charring, fall-off times of gypsum boards and test durations.....	36
Table 6. Thermal properties of timber used in FE simulations according to FprEN 1995-1-2:2025 (CEN, 2025b).	38
Table 7. Thermal properties of wood fibreboard and OSB used in FE simulations (Östman et al., 2010).	38
Table 8. Thermal properties of stone wool used in FE simulations (Östman et al., 2010)..	39
Table 9. Thermal properties of glass wool used in FE simulations (Östman et al., 2010)..	39
Table 10. Thermal properties of gypsum plasterboard used in FE simulations (Östman et al., 2010).	40
Table 11. Flange sizes.....	42
Table 12. Fire protection systems.....	42
Table 13. The start times of charring in minutes from thermal FE simulations with stone wool cavity insulation.	44
Table 14. The start times of lateral charring in minutes from thermal FE simulations with stone wool cavity insulation.	44
Table 15. The start times of charring in minutes on the web from thermal FE simulations with stone wool cavity insulation.	45
Table 16. The heights of the first node to char on the web in millimetres from thermal FE simulations with stone wool cavity insulation.....	45
Table 17. Comparison of tested and simulated start times of charring on the exposed and lateral sides, the web, and the residual charred areas.....	54
Table 18. Loaded model-scale furnace tests.....	60
Table 19. Tested start times of charring, fall-off times of gypsum boards and test durations from loaded MST.	63
Table 20. Overview of thermo-mechanical simulations.	66
Table 21. Simulated and calculated load-bearing capacities and times to failure.....	69
Table 22. Mechanical properties of timber at elevated temperatures used in FE simulations.....	71
Table 23. Expressions for zero-strength layer depth from the start of exposure until the start of charring.	79
Table 24. Expressions for zero-strength layer depth after the start of charring.....	79
Table 25. Goodness of fit parameters for zero-strength layer expressions.....	80
Table 26. Naming key for ambient compression test specimens.	86
Table 27. Compression tests at ambient temperature. Series 1.....	86
Table 28. Compression tests at ambient temperature. Series 2.....	87
Table 29. Compression tests at ambient temperature. Series 3.....	87
Table 30. Tested configurations used in simulations.....	91
Table 31. Extended selection of cross-sections modelled in compression.....	92
Table 32. Results of series 1.....	94
Table 33. Results of series 2.....	95
Table 34. Results of series 3.....	96

Table 35. Load-bearing capacity obtained from tests and Euler critical load values from the model.	99
Table 36. Load-bearing capacities and effective buckling lengths obtained from the model for all configurations, tested configurations shown in italics.	101
Table 37. Charring calculation model parameters derived from thermal simulations.	106
Table 38. Best fit zero-strength layer parameters derived from simulations.	107
Table 39. Additional zero-strength layer depths for the tension flange.	108
Table 40. Validation of charring calculations.	109
Table 41. Validation of zero-strength layer calculations based on loaded model-scale tests.	111
Table 42. Validation of calculations based on loaded model-scale tests from Schmid (Schmid et al., 2011).	112
Table 43. Validation of calculations based on loaded full-scale floor tests.	113
Table 44. Validation of calculations based on loaded full-scale wall tests.	115

References

- CEN. (2002). EN 1991-1-2:2002. Eurocode 1: Actions on structures—Part 1-2: General actions—Actions on structures exposed to fire.
- CEN. (2004a). EN 520:2004+A1:2009. Gypsum plasterboards—Definitions, requirements and test methods.
- CEN. (2004b). EN 1995-1-1:2004. Eurocode 5: Design of timber structures—Part 1-1: General—Common rules and rules for buildings.
- CEN. (2004c). EN 1995-1-2:2004. Eurocode 5: Design of timber structures—Part 1-2: General—Structural fire design.
- CEN. (2005). EN 12369-1:2005. Wood-based panels—Characteristic values for structural design—Part 1: OSB, particleboards and fibreboards.
- CEN. (2006). EN 300:2006. Oriented Strand Boards (OSB)—Definitions, classification and specifications.
- CEN. (2010). EN 408:2010. Timber structures—Structural timber and glued laminated timber—Determination of some physical and mechanical properties.
- CEN. (2016). EN 338:2016. Structural timber—Strength classes.
- CEN. (2019). EN 13381-7:2019. Test methods for determining the contribution to the fire resistance of structural members—Part 7: Applied protection to timber members.
- CEN. (2020). EN 1363-1:2020. Fire resistance tests—Part 1: General Requirements.
- CEN. (2023). EN 13501-2:2023. Fire classification of construction products and building elements—Part 2: Classification using data from fire resistance and/or smoke control tests, excluding ventilation services.
- CEN. (2025a). FprEN 1995-1-1:2025. Eurocode 5—Design of timber structures—Part 1-1: General rules and rules for buildings.
- CEN. (2025b). FprEN 1995-1-2:2025. Eurocode 5—Design of timber structures—Part 1-2: Structural fire design. Final Draft for Formal Vote.
- Franssen, J.-M., & Gernay, T. (2017). Modeling structures in fire with SAFIR®: Theoretical background and capabilities. *Journal of Structural Fire Engineering*, 8(3), 300–323. <https://doi.org/10.1108/JSFE-07-2016-0010>
- IEC. (2013). IEC 60584-1:2013. Thermocouples—Part 1: EMF specifications and tolerances. I-Joist—APA – The Engineered Wood Association. (n.d.). Retrieved 15 September 2025, from <https://www.apawood.org/i-joist>
- I-Joists. (n.d.). The Canadian Wood Council - CWC. Retrieved 31 August 2024, from <https://cwc.ca/en/how-to-build-with-wood/wood-products/i-joists/>
- ISO. (1999). ISO 834 series: Fire-resistance tests—Elements of building construction.
- Kerge, G. (2024). Puidust I-ristlõikega surutud elemendi analüüs [Master of Science]. Tallinn University of Technology.
- König, J. (2006). Fire exposed simply supported wooden I-joists in floor assemblies (No. SP Report 2006:44). SP Trätek/ Wood Technology.

- Mäger, K. N., Just, A., & Frangi, A. (2018). Improvements to the component additive method. Proceedings of the 10th International Conference on Structures in Fire; Nadjai, A., Ali, F., Franssen, J.-M., Vassart, O., Eds, 283–290.
- Mäger, K. N., Just, A., Frangi, A., & Brandon, D. (2017). Protection by fire rated claddings in the Component Additive Method. Proceedings of 50th Meeting of International Network on Timber Engineering Research. 50th meeting of International Network on Timber Engineering Research, Kyoto, Japan.
- Mäger, K. N., Just, A., Schmid, J., Werther, N., Klippel, M., Brandon, D., & Frangi, A. (2019). Procedure for implementing new materials to the component additive method. Fire Safety Journal, 107, 149–160. <https://doi.org/10.1016/j.firesaf.2017.09.006>
- Olofsson, R., Just, A., Mäger, K. N., & Sterley, M. (2022). Loaded fire tests with I-joists. <https://urn.kb.se/resolve?urn=urn:nbn:se:ri:diva-61178>
- Orav, T. (2024). Puidust I-ristlõikega erinevate seinamaterjalidega elementide katseline uuring [Master of Science]. Tallinn University of Technology.
- Östman, B., Mikkola, E., Stein, R., Frangi, A., König, J., Dhima, D., Hakkarainen, T., & Bregulla, J. (2010). Fire safety in timber buildings: Technical guideline for Europe (B. Östman, Ed.). SP Technical Research Institute of Sweden.
- Schmid, J., Just, A., & König, J. (2011). Fire exposed wooden I-joists for wall assemblies (No. SP Report 2011:27). SP Wood Technology.
- Technical Guide STEICOconstruction. (2024).
- The I-joist Handbook by Masonite Beams. (2022).
- Tiso, M. (2018). The Contribution of Cavity Insulations to the Load-Bearing Capacity of Timber Frame Assemblies Exposed to Fire [Doctor of Philosophy, Tallinn University of Technology]. <https://digikogu.taltech.ee/et/Item/83bd42fb-06d1-4bab-90ae-63943dbd05c2>

Acknowledgements

This doctoral journey has been long, challenging, and transformative, and I would not have been able to complete it without the generous support, guidance, and encouragement of many people along the way.

First and foremost, I would like to sincerely thank my supervisor, Prof. Alar Just, for his unwavering support, insightful guidance, and consistent belief in the value of this work. Their ability to challenge me intellectually while still providing encouragement has been critical to my development as a researcher. I am deeply grateful for the time, patience and effort they have invested in helping me grow both academically and professionally.

I also wish to thank my co-supervisor, Dr. Magdalena Sterley, for her constructive feedback and for pushing me to refine my thinking and broaden the scope of this research. This input has helped ensure this work meets a high academic standard.

This work would not have been possible without the funding provided by the Estonian Research Council (projects PRG820, PUT794) and ERA-NET Cofund ForestValue. I sincerely appreciate their financial support, which enabled me to conduct experimental tests, travel for conferences, and focus on this work without compromise.

I would also like to extend my gratitude to Masonite Beams AB, whose collaboration and technical input brought a valuable practical dimension to this research. Their openness in sharing their vast experience and data added an applied relevance that would not have been possible otherwise. I am forever thankful for their trust in me and cherish our work together.

My sincere thanks to the laboratory staff and technicians at RISE Research Institutes of Sweden in Borås and RISE Fire Research in Trondheim for their support with the experimental work. Their expertise, patience, and practical knowledge were crucial, particularly during the furnace tests, and I'm grateful for their professionalism and good humour even during long days in the lab.

To my fellow PhD students and colleagues at TalTech, thank you for being such a supportive group. The informal chats, coffee breaks, coding help, and collective problem-solving meant more than you probably realise. In particular, I want to thank Dr. Miriam Kleinhenz, whose friendship has been a true constant throughout this process. Despite being in different cities and institutions, our shared struggles, peer reviews, and laughter over our coffee talks helped make this experience less isolating and more meaningful.

I would also like to thank the broader academic and research community I've met through conferences, workshops, and collaborations. Your feedback and discussions helped shape this work in ways I couldn't have anticipated when I began.

Finally, and most importantly, I am profoundly grateful to my family and close friends. Your patience, understanding, and unwavering belief in me have been my foundation during both the high and low points of this journey.

I would also like to honour the memory of my grandmother who passed away during the course of this PhD. Though she did not see its completion, her unwavering love and quiet strength have left a lasting imprint on my life. I carry her spirit with me in all that I do, and this work is, in many ways, a reflection of the values she instilled in me.

Abstract

Fire resistance design model for walls and floors with wooden I-joists

This doctoral thesis investigates the behaviour of wooden I-shaped structural members exposed to standard fire conditions. The aim of the research was to develop an improved and validated fire design model that accurately accounts for different flange geometries, fire protection systems, and cavity insulation materials. The study responds to the limitations of earlier models which have not been significantly revised in recent decades and are based on outdated assumptions with limited experimental verification.

The work integrates both numerical modelling and physical testing to provide a comprehensive understanding of the thermal and structural response of I-joists in fire. Thermal and thermo-mechanical finite element simulations were developed and calibrated using results from model-scale furnace fire tests. These simulations modelled temperature development, charring progression, deformation, and failure of I-joists in different assemblies and with a variety of flange geometries. A total of six unloaded and nineteen loaded model-scale fire tests were conducted. The tested specimens included configurations with both stone wool and glass wool insulation, as well as different flange geometries and adhesives.

The experiments measured temperatures at various points, monitored gypsum board fall-off, and recorded deflections and failure times. These tests provided critical validation data for the simulations and highlighted key behavioural trends. One key finding is that the start time of charring on the exposed side does not significantly vary with insulation type, confirming the simplified assumptions used in design codes. However, lateral charring initiation was found to be clearly dependent on cavity insulation, with stone wool offering longer protection times than glass wool, especially in members with deeper flanges.

The fire design model developed in this thesis was formulated within the framework of the Effective Cross-Section Method (ECSM), supporting harmonisation with the next generation of Eurocode 5 Part 1-2. Model parameters were derived using optimisation scripts and regression analyses based on simulation output and validated using a database of full-scale fire tests. The model allows the user to consider flange dimensions, insulation type, fall-off times of protection, and adhesive effects, offering a flexible and realistic calculation approach.

A novel contribution of the work is the treatment of the unbraced flange as a compression member subjected to smeared lateral restraint, with a new coefficient developed to account for the relative stiffness of the web. This coefficient provides a means to reduce the effective buckling length and improve the prediction of fire-induced buckling for tall, slender cross-sections with limited bracing.

The thermal simulations generally predicted slightly longer protection times than the simplified Eurocode methods, indicating a slightly conservative but safe approximation. Thermo-mechanical simulations were also mostly conservative, although some simulations failed to converge before physical failure in specimens with short failure times or large cross-sections. This underlines the need for careful modelling assumptions and highlights the limits of simulation convergence in highly non-linear post-protection phases.

Compression tests conducted at ambient temperature confirmed that load-bearing capacity was significantly reduced in taller specimens with high slenderness, especially in configurations where only one flange was braced. The combination of simulation and test data allowed the development of improved equations for compression capacity that consider flange geometry, web slenderness, and bracing conditions.

Limitations of this study include the simplification of material properties and adhesive performance in fire, as well as the exclusive focus on standard fire exposure. Future research could be conducted to extend this model to parametric and natural fire scenarios and explore the behaviour of other wood-based composite members and more varied boundary conditions.

Overall, the research delivers a validated, user-friendly fire design model that improves on existing design guidance by considering a wider range of influencing factors. The model has already been adopted into the draft of the upcoming Eurocode 5 revision, demonstrating its practical significance and acceptance by the wider engineering community. This work provides both a scientific contribution and a practical tool for engineers, supporting more resilient timber structures in fire design.

Lühikokkuvõte

Puidust I-taladega karkass-seinte ja vahelagede tulepüsivuse arvutusmudel

Käesolev doktoritöö uurib puidupõhiste I-kujuliste kandeelementide (I-talade) käitumist standardtulekahju korral. Uurimistöö eesmärgiks oli välja töötada täiustatud ja valideeritud arvutusmudel, mis arvestaks I-talade geomeetria, tulekaitse- ja soojusisolatsioonimaterjalide panust I-taladega sein- ja vahelaekonstruktsioonide tulepüsivusse. Uuring käsitleb varasemate mudelite puudujääke, mida ei ole viimastel aastakümnetel oluliselt ajakohastatud ja mis põhinevad aegunud eeldustel ning piiratud eksperimentaalsel tõestusmaterjalil.

Töö ühendab nii numbrilise modelleerimise kui ka katsed, et anda põhjalik ülevaade I-talade söestumisest ja kandetarindina toimimisest tulekahjuolukorras. Soojus- ja termomehaanilised lõplike elementide simulatsioonid töötati välja ja kalibreeriti mudel-skaalal tehtud ahjukatsete tulemuste põhjal. Need simulatsioonid kirjeldasid temperatuuri arengut, söestumist, deformatsioone ja purunemist erinevates konstruktsioonides ning erinevate vööde mõõtmega. Kokku viidi läbi kuus koormamata ja üheksateist koormatud mudel-skaala tulekatset. Katsekehad sisaldasid konfiguratsioone nii kivi- kui ka klaasvillast isolatsiooniga, samuti erinevate vööde ja liimidega.

Katsetes mõõdeti temperatuure erinevates punktides, jälgiti kipsplaatide ärakukkumist ning registreeriti läbipaindeid ja varisemisaegu. Need katsed pakkusid olulisi valideerimisandmeid simulatsioonidele ning tõid esile olulisi käitumismustreid. Üks põhitulemus oli, et tulele avatud külje söestumise algusaeg ei varieerunud märkimisväärselt sõltuvalt isolatsioonitüübist, kinnitades projekteerimisnormides kasutatud lihtsustatud eeldusi. Samas leiti, et I-tala tulepoolse vöö külgsuunaline söestumine sõltub selgelt isolatsioonimaterjalist — kivivill tagas pikema kaitseaja kui klaasvill, eriti suurema ristlõikekõrgusega vööde puhul.

Töö käigus arendatud I-talade tulekahjuolukorra arvutusmudel töötati välja kooskõlas Efektiivristlõike Meetodiga (ingl k ECSM), toetades Eurokoodeks 5 järgmise põlvkonna arvutusmeetodite ühtlustamist. Mudeli parameetrid määrati simulatsioonitulemuste põhjal optimeerimisalgoritmide ja regressioonanalüüside abil ning valideeriti täismõõtmeliste tulekatsete andmebaasi põhjal. Mudel võimaldab arvesse võtta ristlõikemõõtmelisi, isolatsioonitüüpi, kaitsematerjali äralangemise aega ja liimi mõju, pakkudes paindlikku ning realistlikku arvutusmeetodit.

Töö üheks uuenduslikuks panuseks on tulekahjuolukorras külgsuunalised sidemed kaotanud vaba vöö käsitlemine surveelemendina, millele mõjuvad arvutuslikud I-tala seinajäikusest mõjutatud külgoed. Selleks töötati välja uus koefitsient, mis arvestab tala sein suhtelist jäikust ning võimaldab vähendada nõtkepikkust ja parandada tulekahjust põhjustatud nõtkumise ennustamist kõrgetel ja saledatel ristlõigetel, kus toetus on piiratud.

Termilised simulatsioonid prognoosisid üldjuhul veidi pikema kaitseage kui lihtsustatud Eurokoodeksi meetodid, viidates standardi konservatiivsele, kuid ohutule lähenemisele. Ka termomehaanilised simulatsioonid olid enamasti konservatiivsed võrreldes katsetulemustega, eriti võrreldes lühikeste varisemisaegadega katsetega või suurte ristlõigetega katsete korral. See rõhutab modelleerimise eelduste hoolika valiku

olulisust ja näitab simulatsioonide piiratust väga mittelineaarses faasis pärast kaitsematerjali äralangemist.

Toatemperatuuril tehtud survekatsed kinnitasid, et kõrgetel ja saledatel elementidel väheneb kandevõime märkimisväärselt, eriti juhul, kui ainult üks vöö oli toetatud. Simulatsioonide ja katseandmete kombineerimisel töötati välja täiendatud valemid survekandevõime hindamiseks, mis arvestavad vöö geomeetriat, seina saledust ja toetuse tingimusi.

Töö piirangute hulka kuuluvad materjali omaduste ja liimide käitumise lihtsustamine tuleolukorras, samuti keskendumine üksnes standardtulekahjule. Tulevased uuringud võiksid laiendada mudelit parameetrilistele ja tegelikele tulestsenaariumidele ning uurida teiste puitkomposiitmaterjalide ja mitmekesisemate ääritingimustega konstruktsioonide käitumist.

Kokkuvõttes pakub käesolev uurimistöö valideeritud ja kasutajasõbraliku projekteerimise mudeli, mis täiendab olemasolevaid juhiseid, arvestades laiemat hulka mõjutegureid. Mudel on juba vastu võetud Eurokoodeks 5 uue versiooni eelnõus, mis tõendab selle praktilist väärtust ja laialdast tunnustust insenerikogukonnas. Töö annab teadusliku panuse ja praktilise tööriista inseneridele, toetades tulekindlamate puitkonstruktsioonide projekteerimist.

Appendix

Data request sent to producers

Request for information

Please complete the following table with information from full-scale fire tests (tests conducted according to test standards from the EN 136X series or similar).

The information included in this table will be only used to identify the knowledge gaps for planning of further tests and to verify the calculation model.

Parts of the information will be published in a confidential manner without including the report numbers and, if necessary, without the exact dimensions of the joists. Publication will serve the purpose of showing the reliability and improvement of the developed calculation model without preference for any specific producer of any product included in the tested structures.

When completing the table, please include as much information as possible, however it is understandable if some cells must be left empty due to confidentiality or incompleteness of the information included in the test report.

Add comments or rows/columns as needed. If using other abbreviations than those listed below, please include them in the list. The first row has been filled in as an example.

List of abbreviations

W	Wall/vertical structure
F	Floor/horizontal structure
B	Width of the flange
H	Height of the flange
C00	Strength class of coniferous sawn wood
GL00	Strength class of glulam
WFB	Wooden fibreboard according to EN 622
Ply	Plywood according to EN 636
PB	Particleboard according to EN 312
OSB	Oriented strand board according to EN 300
GtF	Gypsum plasterboard type F according to EN 520
GtA	Gypsum plasterboard type A (or any other than type F) according to EN 520
GF	Gypsum fibreboard according to EN 15283
RC	Resilient channels or other acoustic profiles with void cavities
Btn	Wooden battens with void cavities
(b)	Loose fill or blown in cavity insulation
SW	Stone wool insulation, mineral wool according to EN 13162
GW	Glass wool insulation, mineral wool according to EN 13162
WF	Wood fibre batt insulation
CF	Cellulose fibre batt insulation
Void	Void cavity between I-joists
V	Visually observed fall-off
T	Fall-off measured with thermocouples according to EN 13381-7 (if temperature at any thermocouple differs from the furnace temperature by less than 50°C)
R, EI, ...	Fire resistance criteria according to EN 13501-2
L	Compressive load per stud in a wall test
A	Evenly distributed load in a floor test
...	

Legend for each column

- 1 Add the orientation of the test specimen, W-vertical, F-horizontal
- 2 Add the test report number for identification purposes
- 3 Add the total height of the I-joist

- 4 Add the width (B) and height (H) of the flange
- 5 Flange material: strength class of sawn wood, LVL, glulam, etc
- 6 Web thickness and material: wood fibreboard (WFB), plywood (Ply), etc
- 7 Add type and thickness (in mm) of the fire protection system (all layers before the I-joist)
- 8 Add type and thickness (in mm) of the cavity insulation
- 9 Add the fall-off time of the fire protection system along with the distinction of visual (V) or measured (T) type
- 10 Add the time to failure of the structure and the type of failure (R, E, I, EI, REI)
- 11 Add the load per stud (L) or evenly distributed (A)

1	2	3	4	5	6	7	8	9	10	11	12
Wall/ Floor	Test	I-joist height, mm	Joist distance c/c, mm	Flange, Bmm x Hmm	Flange material	Web	Fire protection system	Cavity insulation	Fail-off time, min	Time to failure, min	Load, kN or kN/m ²
W	Report12345	250	600	45x45	C24	WFB10	GtF15+Btn34	SW250	V66	R82,9	L54

Curriculum vitae

Personal data

Name: Katrin Nele Mäger
Date of birth: 06.08.1991
Place of birth: Tallinn, Estonia
Citizenship: Estonian

Contact data

E-mail: Katrin.Mager@taltech.ee

Education

2018–2025 Tallinn University of Technology, PhD
2010–2016 Tallinn University of Technology, MSc
2007–2010 Tallinn English College, Upper Secondary Education

Language competence

English Fluent
Estonian Native speaker
German Basic user
Russian Basic user
French Basic user

Professional employment

2024– Tallinn Pelgulinna State Upper Secondary School
2017– Tallinn University of Technology
2016– Tignum OÜ
2014–2016 AS Amhold
2012–2014 NCC Ehitus OÜ

Co-supervised Master theses

Hugo Manguse (2020). “Charring analysis of wooden I-joists in standard fire”
Mattias Mihkelson (2023). “Compartment test with wooden I-joists – analysis and comparison to standard fire”
Carmen Karma (2023). “Analysis and modelling of fire tests with I-joists”

Elulookirjeldus

Isikuandmed

Nimi: Katrin Nele Mäger
Sünniaeg: 06.08.1991
Sünnikoht: Tallinn, Eesti
Kodakondsus: Eesti

Kontaktandmed

E-post: Katrin.Mager@taltech.ee

Hariduskäik

2018– Tallinna Tehnikaülikool, PhD
2010–2016 Tallinna Tehnikaülikool, MSc
2007–2010 Tallinna Inglise Kolledž, Keskkharidus

Keelteoskus

Inglise keel Kõrgtase
Eesti keel Emakeel
Saksa keel Algtase
Vene keel Algtase
Prantsuse keel Algtase

Teenistuskäik

2024– Tallinna Pelgulinna Riigigümnaasium
2017– Tallinna Tehnikaülikool
2016– Tignum OÜ
2014–2016 AS Amhold
2012–2014 NCC Ehitus OÜ

Juhendatud magistritööd

Hugo Manguse (2020). "Puidust I-talade söestumise ulatuse analüüs standardtulekahjuolukorras"

Mattias Mihkelson (2023). "Puidust I-taladega ruumtulekahjukatse analüüs ja kahjustuste võrdlus standardtulekahjuga"

Carmen Karma (2023). "Puidust I-taladega tulekatsete analüüs ja modelleerimine"

ISSN 2585-6901 (PDF)
ISBN 978-9916-80-404-9 (PDF)